

GL-TR-89-0142

SEISMIC WAVE ATTENUATION AND YIELD DETERMINATION AT REGIONAL DISTANCES

B.J. Mitchell
O.W. Nuttli
J.K. Xie
H. Al-Shukri
A. Correig

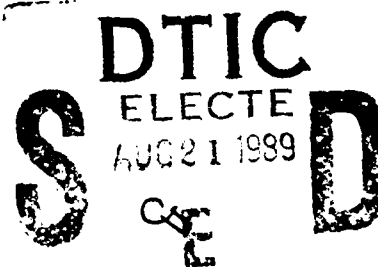
Saint Louis University
221 North Grand Boulevard
St. Louis, MO 63103

25 May 1989

Final Report
1 May 1987 - 30 April 1989

Approved for public release; distribution unlimited

GEOPHYSICS LABORATORY
AIR FORCE SYSTEMS COMMAND
UNITED STATES AIR FORCE
HANSCom AIR FORCE BASE, MASSACHUSETTS 01731-5000



89 8 21 040

AD-A211 548

4

The views and conclusions contained in this document are those of the authors and should not be interpreted as representing the official policies, either expressed or implied, of the Defense Advanced Research Projects Agency of the U.S. Government.


Sponsored by

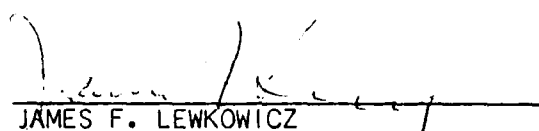
Defense Advanced Research Projects Agency (DoD)
Defense Sciences Office, Geophysical Sciences Division
DARPA/DSO Physical Characterization of Seismic Sources

DARPA/ARPA Order No. 5299


Issued by the Air Force Geophysics Laboratory
Under Contract F19628-87-K-0036

This technical report has been reviewed and is approved for publication.


JAMES F. LEWKOWICZ
Contract Manager
Solid Earth Geophysics Branch
Earth Sciences Division


JAMES F. LEWKOWICZ
Branch Chief
Solid Earth Geophysics Branch
Earth Sciences Division

FOR THE COMMANDER


DONALD H. ECKHARDT, Director
Earth Sciences Division

This report has been reviewed by the ESD Public Affairs Office (PA) and is releasable to the National Technical Information Service (NTIS).

Qualified requestors may obtain additional copies from the Defense Technical Information Center. All others should apply to the National Technical Information Service.

If your address has changed, or if you wish to be removed from the mailing list, or if the addressee is no longer employed by your organization, please notify AFGL/DAA, Hanscom AFB, MA 01731-5000. This will assist us in maintaining a current mailing list.

Do not return copies of this report unless contractual obligations or notices on a specific document requires that it be returned.

Unclassified

SECURITY CLASSIFICATION OF THIS PAGE

REPORT DOCUMENTATION PAGE

1a. REPORT SECURITY CLASSIFICATION Unclassified		1b. RESTRICTIVE MARKINGS	
2a. SECURITY CLASSIFICATION AUTHORITY		3. DISTRIBUTION/AVAILABILITY OF REPORT Approved for public release; distribution unlimited	
2b. DECLASSIFICATION/DOWNGRADING SCHEDULE			
4. PERFORMING ORGANIZATION REPORT NUMBER(S)		5. MONITORING ORGANIZATION REPORT NUMBER(S) GL-TR-89-0142	
6a. NAME OF PERFORMING ORGANIZATION Saint Louis University	6b. OFFICE SYMBOL (If applicable)	7a. NAME OF MONITORING ORGANIZATION Geophysics Laboratory	
6c. ADDRESS (City, State and ZIP Code) 221 North Grand Boulevard St. Louis, MO 63103		7b. ADDRESS (City, State and ZIP Code) Hanscom Air Force Base Massachusetts 01731-5000	
8a. NAME OF FUNDING/SPONSORING ORGANIZATION Defense Advanced Research Projects Agency	8b. OFFICE SYMBOL (If applicable) NMRO	9. PROCUREMENT INSTRUMENT IDENTIFICATION NUMBER F19628-87-K-0036	
8c. ADDRESS (City, State and ZIP Code) 1400 Wilson Boulevard Arlington, VA 22209		10. SOURCE OF FUNDING NOS.	
		PROGRAM ELEMENT NO. 61101E	TASK NO. DA
		PROJECT NO. 7A10	WORK UNIT NO. CK
11. TITLE (Include Security Classification) Seismic Wave Attenuation & Yield Determination at Regional Distances			
12. PERSONAL AUTHOR(S) B.J. Mitchell, O.W. Nuttli, J. Xie, H. Al-Shukri, A. Correig			
13a. TYPE OF REPORT Final	13b. TIME COVERED FROM 5/1/87 TO 4/30/89	14. DATE OF REPORT (Yr., Mo., Day) 1989 May 25	15. PAGE COUNT 130
16. SUPPLEMENTARY NOTATION			
17. COSATI CODES		18. SUBJECT TERMS (Continue on reverse if necessary and identify by block number)	
FIELD	GROUP	SUB. GR.	
19. ABSTRACT (Continue on reverse if necessary and identify by block number)			
<p>Work was completed by O.W. Nuttli on yield determination at the Soviet test site on Novaya Zemlya. Magnitudes and yields were determined for 30 explosions using Lg amplitudes recorded in northwestern Europe. They ranged between 2.5 and 4900 kt, the largest since April 1976 being about 145 kt. The $m_b(P)$ bias was estimated to be 0.20 magnitude units.</p> <p>Studies were completed on seismic wave attenuation of surface waves at intermediate periods and of Lg waves at 1 Hz in several regions of the world. Limits were determined for the degree of frequency dependence of Q_b, which can occur in the crust in stable and tectonically active regions. If Q_b varies as ω^ζ, where ζ is a constant, then models in which $\zeta = 0.5, 0.5$, and 0.75 satisfy fundamental-mode Rayleigh and 1-Hz Lg data for eastern North America, eastern South America, and the Indian Shield, respectively. If Q_b is assumed to be independent of frequency ($\zeta = 0.0$) for periods of 3 s and greater, and ζ</p> <p style="text-align: right;">(continued)</p>			
20. DISTRIBUTION/AVAILABILITY OF ABSTRACT UNCLASSIFIED/UNLIMITED <input checked="" type="checkbox"/> SAME AS RPT. <input type="checkbox"/> DTIC USERS <input type="checkbox"/>		21. ABSTRACT SECURITY CLASSIFICATION Unclassified	
22a. NAME OF RESPONSIBLE INDIVIDUAL James F. Lewkowicz		22b. TELEPHONE NUMBER (Include Area Code) (617) 377-3028	22c. OFFICE SYMBOL GL/LWH

DD FORM 1473, 83 APR

EDITION OF 1 JAN 73 IS OBSOLETE.

Unclassified
SECURITY CLASSIFICATION OF THIS PAGE

19. Abstract (continued)

is allowed to increase from 0.0 at 3 s to a maximum at 1 s, then the maximum value for ζ is about 0.7, 0.6, and 0.9, respectively, for the same three regions. Tectonically active regions require a much lower degree of frequency dependence to explain both observed fundamental-mode and observed Lg data. Optimum values for ζ for western North America and western South America are 0.0, but uncertainty in the attenuation data allows ζ to be as high as 0.3 for western North America and 0.2 for western South America. In the Himalaya, the optimum value is about 0.3, but it could range between 0.0 and 0.5. The regional variation of Lg attenuation can cause large errors in magnitude determination if attenuation is not taken into account.

A stochastic convolution model was proposed for Lg coda at distances greater than 200 km which considers the effects of dispersion scattering and mode conversions at those distances. A spectral ratio method was developed for inverting Lg coda Q which produces smaller variances than those associated with earlier methods. It can be extended to inversions for source parameters if both Lg and its coda are used.

A back projection tomographic method was developed to regionalize large-scale lateral variations of coda Q for Lg waves which traverse long continental paths. It was applied to continental Africa where low Q values were found to be associated with the East African rift system, the Atlas Mountains, and the Cape Fold Belt, regions which have undergone Mesozoic or younger deformation.

A seismically active region in an otherwise stable portion of North America (the New Madrid seismic zone) was found to be characterized by lower than normal Q values. The presence of fluid-filled cracks in the crust can explain the low Q values as well as previously discovered reduced velocities there.

Work has continued in the western United States where we find that Q values in the upper mantle vary laterally, becoming smaller from east to west. The crust of the Basin and Range province has a low-Q upper crust overlying a lower crust with higher Q values. This layered Q structure causes Q_{Lg} to vary with frequency even though Q_β in the crust is independent of frequency.

Attenuative dispersion was observed in a low-Q region of the Pyrenees. Low intrinsic Q values dominate over attenuation by scattering in that region and allow an interpretation in terms of a continuous relaxation model in which the minimum Q value is 5 and the high-frequency and low-frequency cutoffs are 2.7 Hz and 0.02 Hz, respectively.

TABLE OF CONTENTS

Contributing Scientists	iv
Publications	v
Technical Summary	vi
Research Results	
I. Introduction	1
II. Summaries of research published during the period 1 May 1987 - 30 April 1989	1
III. Summaries of research not as yet submitted for publication	2
IV. A back projection method for imaging large-scale lateral variations of Lg coda Q with application to continental Africa	4
V. Three-dimensional attenuation structure in and around the New Madrid seismic zone	56
VI. Attenuative body wave dispersion at La Cerdanya (Eastern Pyrenees)	88

Accession For	
NTIS GRA&I	<input checked="" type="checkbox"/>
DTIC TAB	<input type="checkbox"/>
Unannounced	<input type="checkbox"/>
Justification	
By	
Distribution/	
Availability Codes	
Dist	Avail and/or Special
A-1	



Contributing Scientists

The following faculty and students contributed to research performed during the period covered by this report:

O.W. Nuttli	Professor of Geophysics
B.J. Mitchell	Professor of Geophysics
A.M. Correig	Professor of Geophysics
J. Xie	Graduate Student
H. Al-Shukri	Graduate Student
W.J. Lin	Graduate Student
H. Al-Khatib	Graduate Student

Publications

- Al-Shukri, H., and B.J. Mitchell, Three-dimensional seismic attenuation structure in and around the New Madrid seismic zone, *Bull. Seism. Soc. Am.*, Submitted, 1989.
- Cong, L., and B.J. Mitchell, Frequency dependence of crustal Q_β in stable and tectonically active regions, *PAGEOPH* **127**, 581-605, 1988.
- Correig, A.M., and B.J. Mitchell, Attenuative body wave dispersion at La Cerdanya (Eastern Pyrenees), *Phys. Earth Planet. Int.*, in press, 1989.
- Nuttli, O.W., Lg magnitudes and yield estimates for Novaya Zemlya nuclear explosions, *Bull. Seism. Soc. Am.* **78**, 873-884, 1988.
- Xie, J., and O.W. Nuttli, Interpretation of high-frequency coda at large distances: Stochastic modeling and method of inversion, *Geophys. J.* **95**, 579-595, 1988.
- Xie, J., and B.J. Mitchell, A back projection method for imaging large-scale lateral variations of Lg coda Q with application to continental Africa, *Geophys. J.*, in press, 1989.

TECHNICAL SUMMARY

Work was completed by O.W. Nuttli on yield determination at the Soviet test site on Novaya Zemlya. Magnitudes and yields were determined for 30 explosions using Lg amplitudes recorded in northwestern Europe. They ranged between 2.5 and 4900 kt, the largest since April 1976 being about 145 kt. The $m_b(P)$ bias was estimated to be 0.20 magnitude units.

Studies were completed on seismic wave attenuation of surface waves at intermediate periods and of Lg waves at 1 Hz in several regions of the world. Limits were determined for the degree of frequency dependence of Q_β which can occur in the crust in stable and tectonically active regions. If Q_β varies as ω^τ , where τ is a constant, then models in which $\tau = 0.5, 0.5$, and 0.75 satisfy fundamental-mode Rayleigh and 1-Hz Lg data for eastern North America, eastern South America, and the Indian Shield, respectively. If Q_β is assumed to be independent of frequency ($\tau = 0.0$) for periods of 3 s and greater, and τ is allowed to increase from 0.0 at 3 s to a maximum at 1 s, then the maximum value of τ is about 0.7, 0.6, and 0.9, respectively, for the same three regions. Tectonically active regions require a much lower degree of frequency dependence to explain both observed fundamental-mode and observed Lg data. Optimum values for τ for western North America and western South America are 0.0, but uncertainty in the attenuation data allows τ to be as high as 0.3 for western North America and 0.2 for western South America. In the Himalaya, the optimum value is about 0.3, but it could range between 0.0 and 0.5. The regional variation of Lg attenuation can cause large errors in magnitude determination if attenuation is not taken into account.

A stochastic convolution model was proposed for Lg coda at distances greater than 200 km which considers the effects of dispersion scattering and mode conversions at those distances. A spectral ratio method was developed for inverting Lg coda Q which produces smaller variations than those associated with earlier methods. It can be extended to inversions for source parameters if both Lg and its coda are used.

A back projection tomographic method was developed to regionalize large-scale lateral variations of coda Q for Lg waves which traverse long continental paths. It was applied to continental Africa where low Q values were found to be associated with the East African rift system, the Atlas Mountains, and the Cape Fold Belt, regions which have undergone Mesozoic or younger deformation.

A seismically active region in an otherwise stable portion of North America (the New Madrid seismic zone) was found to be characterized by lower than normal Q values. The presence of fluid-filled cracks in the crust can explain the low Q values as well as previously discovered reduced velocities there.

Work has continued in the western United States where we find that Q values in the upper mantle vary laterally, becoming smaller from east to west. The crust of the Basin and Range province has a low- Q upper crust overlying a lower crust with higher Q values. This layered Q structure causes Q_{Lg} to decrease with frequency even though Q_β in the crust is independent of frequency.

Attenuative dispersion was observed in a low- Q region of the Pyrenees. Low intrinsic Q values dominate over attenuation by scattering in the region and allow an interpretation in terms of a continuous relaxation model in which the minimum Q value is 5 and the high-frequency and low-frequency cutoffs are 2.7 hz and 0.02 Hz, respectively.

Research Results

I. Introduction

The research results during this period fall into three categories: (1) those which have been published in scientific journals, (2) those which have not as yet been published in journals, but may have appeared in technical reports, and (3) those which have been submitted for publication or are in press. Summaries of the first two categories appear in sections II and II below, and preprints of papers submitted for publication, or are in press (category III) appear in the following sections. All of the work is related to the determination of yield and attenuation of seismic waves at regional distances.

II. Summaries of research published during the period 1 May 1987 - 30 April 1989

1. *Interpretation of high-frequency coda at large distances: stochastic modeling and method of inversion*, by J. Xie and O.W. Nuttli proposed a stochastic convolution model for Lg coda observed at large epicentral distances ($\Delta > 200$ km). Coda at these distances differ from local coda in several respects. Effects of various physical processes, such as dispersion, scattering, and mode conversion on coda at large distances are discussed in detail. A spectral ratio method was developed for inversion of Lg coda Q , in which the large variance associated with inversion is greatly reduced. The method was also extended to the inversion of seismic source parameters by jointly using Lg and its coda. They tested the model and method using data from two GDSN stations and found the results to be superior to other models when those methods used only a small number of stations.
2. *Lg magnitudes and yield estimates for underground Novaya Zemlya explosions*. O.W. Nuttli used Lg-wave amplitudes of 30 Novaya Zemlya underground nuclear explosions, as recorded by short-period seismographs in Denmark, Finland, Germany, Norway, Spitsbergen, and Sweden to determine $m_b(\text{Lg})$ values. Assuming that the $m_b(\text{Lg})$ versus explosion yield relation derived from Nevada Test Site data applies to all continental areas, he estimated yields of the explosions. They cover a large range of values, from 2.5 to 4900 kt. The largest explosion since April 1976 had an estimated yield of 145 kt.
The $m_b(\text{Lg})$ values, when subtracted from the $m_b(\text{P})$ values, can be used to estimate the $m_b(\text{P})$ bias between two test sites. In this way, the $m_b(\text{P})$ bias between Novaya Zemlya and the Nevada Test Site is estimated to be 0.20 magnitude units.
3. *Frequency dependence of crustal Q_β in stable and tectonically active regions*. L. Cong and B.J. Mitchell inverted fundamental-mode Rayleigh wave attenuation data for stable and tectonically active regions of North America, South America, and India to obtain several frequency-independent and frequency-dependent Q_β models. Because of trade-offs between the effect of depth distribution and frequency-dependence of Q_β

on surface wave attenuation there are many diverse models which will satisfy the fundamental-mode data. Higher-mode data, such as 1-Hz Lg can, however, constrain the range of possible models, at least in the upper crust. By using synthetic Lg seismograms to compute expected Lg attenuation coefficients for various models we obtained frequency-dependent Q_β models for three stable and three tectonically active regions, after making assumptions concerning the nature of the variation of Q_β with frequency.

In stable regions, if Q_β varies as ω^ζ , where ζ is a constant, models in which $\zeta = 0.5, 0.5$, and 0.75 satisfy fundamental-mode Rayleigh and 1-Hz Lg data for eastern North America, eastern South America, and the Indian Shield, respectively. If Q_β is assumed to be independent of frequency ($\zeta = 0.0$) for periods of 3 s and greater, and τ is allowed to increase from 0.0 at 3 s to a maximum value at 1 s, then that maximum value for τ is about 0.7, 0.6, and 0.9, respectively, for eastern North America, eastern South America, and the Indian Shield. The Q models obtained under each of the above-mentioned two assumptions differ substantially from one another for each region, a result which indicates the importance of obtaining high-quality higher-mode attenuation data over a broad range of periods.

Tectonically active regions require a much lower degree of frequency dependence to explain both observed fundamental-mode and observed Lg data. Optimum values of ζ for western North America and western South America are 0.0, if ζ is constant (Q_β is independent of frequency), but uncertainty in the Lg attenuation data allows ζ to be as high as about 0.3 for western North America and 0.2 for western South America. In the Himalaya, the optimum value of ζ is about 0.2, but it could range between 0.0 and 0.5. Frequency-independent models ($\tau = 0.0$) for these regions yield minimum Q_β values in the upper mantle of about 40, 70, and 40 for western North America, western South America, and the Himalaya, respectively.

In order to be compatible with the frequency dependence of Q observed in body-wave studies, Q_β in stable regions must be frequency-dependent to much greater depths than those which can be studied using the surface wave data available for this study, and Q_β in tectonically active regions must become frequency-dependent at upper mantle or lower crustal depths.

III. Summaries of research not as yet submitted for publication

1. *Lateral variations of anelasticity in the upper mantle beneath the western United States from Rayleigh wave attenuation.* H. Al-Khatib and B.J. Mitchell have determined Rayleigh wave phase and group velocities and attenuation coefficients in the period range 18-100 sec for three regionalized paths across the western United States using a two-station method. The attenuation coefficients were found to increase systematically from east to west between the Rocky Mountains and Pacific coast. This

contrasts with results for the eastern and central United States where no systematic variation of long-period Rayleigh wave attenuation could be discerned in earlier studies. The Rayleigh wave velocities and attenuation measurements were inverted to obtain shear wave velocity and internal friction (Q_β^{-1}) as a function of depth. The shear wave velocities and Q_β values decrease from east to west at all depths. The inversion results show that Q_β^{-1} values in the western United States are highest for the Coastal regions, lowest for the Rocky Mountains and western Great Plains, and intermediate for the Basin and Range. Low values of Q_β (30-70) occur in the upper crust, higher values occur in the lower crust (90-230), and the highest values occur in the uppermost 20 km of the mantle (300-770). These overlie a very low-Q zone which is shallower than the low-velocity zone in all regions.

2. *Q studies in the Basin and Range province.* W.J. Lin and B.J. Mitchell, using intermediate-period data from the Lawrence Livermore network, have obtained models of Q_β for the Basin and Range province with low Q values (< 100) in the upper crust and higher values (> 300) in the lower crust. The model explains observed attenuation of 1-Hz Lg without the need for Q_β being frequency-dependent. This result, apparently, contradicts results from studies of Lg frequency dependence in which a high frequency dependence for that wave is required. In order to study these apparently contradictory results, we obtained more than 40 recordings of Lg and its coda as recorded by the broad-band instruments of the Lawrence Livermore network in the Basin and Range province. A carefully designed procedure was developed to retrieve high-fidelity spectral estimates in the frequency domain. Two-station determinations of Q_{Lg} , stacked over repeated paths for different station pairs lead to $Q_{Lg}(f) = (267 \pm 56) f^{0.4 \pm 0.0}$ for the frequency band 0.2 - 2.5 Hz. We then calculated synthetic Lg Q over the frequency range 0.3 - 4.0 Hz, using a layered, frequency-independent crustal Q_β model previously obtained using long-period, fundamental- and first-higher-mode Rayleigh waves. These synthetic Lg Q values agree well with the observed Lg Q, indicating that the significant frequency dependence of observed Lg Q, indicating that the significant frequency dependence of observed Lg Q and coda Q can be explained by a layered, frequency-independent, crustal Q_β model. We conclude that Lg Q and coda Q sample crustal Q_β in a complicated, non-linear manner: therefore the frequency dependence of Lg Q and coda Q does not necessarily represent that of crustal Q_β .

IV. A Back Projection Method for Imaging Large-Scale Lateral Variations of Lg coda Q with Application to Continental Africa

J. Xie and B.J. Mitchell Department of Earth and Atmospheric Sciences, St. Louis University, 3507 Laclede, St Louis, MO 63103, USA

Summary. A new method is developed which uses back-projection tomography to regionalize large-scale lateral variations of coda Q for Lg waves which have traversed long continental paths. Successful use of this method requires precise and stable single-trace measurements of Lg coda Q (Xie & Nuttli 1988). The method converges rapidly and requires minimal computer storage. It also allows quantitative estimation of resolution and error in imaging lateral variations of coda Q. The spatial resolution of this method is limited by the uneven spatial coverage of the data base, by our limited knowledge of Lg coda generation, and by the trade-off between the stability and the spatial resolution of the coda Q inversion. The method is applied to a large set of digital Lg coda data from Africa, where large-scale lateral variations of Lg coda Q are found to correlate well with major tectonic features. Most of Africa is stable, and like other stable regions, has relatively high coda Q values. The lowest values of coda Q are associated with the African rift system. Other regions of low-Q values include the Atlas mountains and Cape Fold Belt, regions of mesozoic and younger deformation. The lateral variation of frequency dependence of Lg coda Q correlates, in most regions, with that of Q at 1 Hz. Our analysis of the spatial resolution of this method indicates that the resolving power of Lg coda Q imaging is comparable to that of velocity tomography using long-period surface waves. Using empirical approaches, we estimate that uncertainties in Lg coda Q and its power-law frequency dependence

parameter are less than about 60 and about 0.2, respectively, for most of Africa.

Abbreviated title: Back projection of Q in Africa

Keywords: Lg coda Q, back projection tomography, Africa

1 INTRODUCTION

Developments in seismic tomography in recent years have greatly advanced the study of lateral variations of velocity structure in continental areas. By contrast, little progress has been made in imaging lateral variations of Q of the Earth using tomographic algorithms (Nolet 1987). This is largely due to the lack of precision and stability in Q measurements, as well as the lack of a sufficiently large and well-distributed data base.

Vertical-component, high-frequency (~ 1 Hz) Lg waves can be treated as a superposition of higher-mode Rayleigh waves propagating within the continental crust (Knopoff *et al.* 1973, Der *et al.* 1984, Kennett 1984). It is reasonable to assume that in the absence of large-scale disruption of the crustal wave guide, Q derived from Lg or its coda is representative of Q of the continental crust (*eg.* Singh and Herrmann 1983, Der *et al.* 1984, Campillo *et al.* 1987). In this paper we define Lg Q as Q derived from the direct Lg phase and Lg coda Q as Q derived from Lg coda. Measuring Lg Q requires either records from two stations on the same great circle path or a record from one station produced by an event for which we have knowledge of the source spectrum (Cheng and Mitchell 1981, Campillo 1987). With data currently available, these requirements will likely result in very poor ray path coverage for studying lateral variations of Q. Lg coda Q can, however, be measured at a single station without knowledge of the source spectrum (Aki and Chouet, 1975; Herrmann, 1980; Xie and Nuttli, 1988); it is therefore more useful than Lg itself for the study of large-scale lateral variations of Q. The interpretation of Lg coda, however, is more difficult than that of Lg. Because high-frequency coda is highly random, it is difficult to model Lg coda properly and regionalized coda Q values resulting from inversion may be characterized by large uncertainties. Nevertheless, several studies have determined lateral variations of Lg coda Q

(or local coda Q derived from local S wave coda) in major continental areas such as North and South America and China, using a master curve technique (Herrmann, 1980; Singh and Herrmann, 1983; Raoof and Nuttli, 1985; Jin and Aki, 1988). The results of these studies generally show good correlation between lateral variations of Q and the main tectonic features of the continents studied.

In order to improve the precision and stability of Lg coda Q measurements, Nie and Nuttli (1988) proposed a stochastic model for Lg coda. They discussed the effects of various physical processes (*eg.*, dispersion, mode conversions, scattering) which affect the generation of Lg coda. They approximated the randomness of Lg coda by band-limited white, Gaussian noise. This approach allows a quantitative estimate of the variance of Q determined by the inversion process. A stacked spectral ratio (henceforth denoted as SSR) method was proposed for Lg coda Q inversion which allows cancellation of station site effects (provided that those effects are stationary) and results in a large reduction of the variance. Improved Q values obtained by the SSR method, plus the rapid evolution of techniques used in seismic tomography, make it possible to develop more quantitative, or computerized, methods to image lateral variations of Lg coda Q , with more rigorous analysis of error and resolution.

Africa is a continent where no systematic investigation of crustal Q has been conducted. Almost all of Africa has been free of orogenic activity for about the past 500 million years (Clifford 1970, Cahen *et al.* 1984). Africa has some unique and interesting tectonic features, the most striking being the well-developed rift systems and volcanic lines (Moreau *et al.* 1987) in east and west Africa, with lengths of thousands of kilometers (Figure 1). Other noteworthy features of this continent are the younger mountain ranges at both the southern and northern margins. The Cape Fold Belt in the south and the Atlas mountains in the north were affected by Hercynian or younger orogenies.

2 INVERSE METHODS

As in velocity tomography, the imaging of lateral variations of Lg coda Q proceeds in two steps. First, individual seismograms containing coda are collected and processed to obtain Q values, each being a functional of the distribution of regional Lg Q (or more strictly, of regional

Lg coda Q) inside an area sampled by the single-trace coda record. Second, many single-trace measurements are combined to image the lateral variations of Q . A major difference between Lg coda Q tomography and velocity tomography is that the forward modeling involved in the former method must take into account the elliptical region over which scattering occurs whereas the latter considers seismic waves that are restricted to single paths.

§ 2.1 Single-trace measurement of coda Q

High-frequency coda is highly random and the generation of Lg coda involves various complicated physical processes such as scattering, dispersion, mode summation, and mode conversion (Der *et al* 1984, Snieder 1987, Xie and Nuttli 1988). Consequently, two problems arise in the interpretation of the single-trace coda records. First, because of the randomness of coda it is difficult to obtain a Q estimator which is stable enough to provide an acceptable variance (Der *et al* 1984). Second, a coda Q estimator may be subject to systematic deviations from an Lg Q estimator due to imprecise forward modeling. In order to solve these two problems Xie and Nuttli (1988) derived a stochastic model and an inverse method for the interpretation of single-trace Lg coda signals. They used a convolutional relationship to model the processes of Lg coda generation. That relationship allows the effect of those processes to be expressed and examined separately in the frequency domain. In particular, they found that the single isotropic scattering (SIS) model can satisfactorily explain previous observations on several major continents, and that the randomness of the Lg coda signal can be approximated by simple band-limited white, Gaussian noise. The latter approximation allows a quantitative estimation of the theoretical variance of coda Q inversion. Xie and Nuttli found that unacceptably low confidence levels in the Lg coda Q inversion results could occur if a carefully designed variance reduction procedure was not used. At large epicentral distances this problem of low confidence levels can be very serious due to the narrow pass-band of the Q filter. They therefore proposed a stacked spectral ratio (SSR) method to reduce the variance resulting from the inversion. For convenience of discussion we briefly summarize the SSR method in the following paragraphs.

First, the Lg coda time series is divided into by a number, N_w , of non-overlapping time

windows with a constant window length, T , where the m th window has a centered lapse time τ_m , and $m = 1, 2, \dots, N_W$. For each window of the time series the discrete Fourier transform is performed to obtain the geometrical mean of the amplitude spectrum, $\langle A_{k,m} \rangle$, at the k th discrete frequency $f_k = k/T$, defined as

$$\langle A_{k,m} \rangle = \prod_{i=k-l}^{k+l} |A_{i,m}|^{\frac{1}{2l+1}}, \quad (1)$$

where the subscripts i, k represent discrete frequencies, and m denotes the window number. $|A_{i,m}|$ is the i th discrete amplitude spectral estimate obtained by applying the discrete Fourier transform to the m th windowed time series and $2l + 1$ is an integer, which gives the number of amplitude spectral estimates used in each geometrical mean.

The SSR is defined as

$$F_k = \frac{1}{M} \sum_{m=1}^M \frac{1}{\pi(\tau_{M+m} - \tau_m)} \log \left[\frac{G_{M+m} \sqrt{U_m} \langle A_{k,m} \rangle}{G_m \sqrt{U_{M+m}} \langle A_{k,m+M} \rangle} \right], \quad (2)$$

where M is given by

$$M = \begin{cases} N_W/2 & \text{if } N_W \text{ is even} \\ (N_W+1)/2 & \text{if } N_W \text{ is odd} \end{cases}. \quad (3)$$

U_m is the length of each group velocity window for Lg given by

$$U_m = v \tau_m (1/v_{\min} - 1/v_{\max}) \quad (4)$$

where v , v_{\max} and v_{\min} are the average, maximum, and minimum group velocities of the Lg wave train, respectively. G_m is the geometrical spreading term which can be expressed as

$$G_m = \left[\frac{1}{4\pi^2 R \sqrt{v^2 t^2 / R^2 - 1}} \Big|_{t=\tau_m} \Delta\phi \right]^{-1/2} \quad (5)$$

where $\Delta\phi$ is given by

$$\Delta\phi = \int_{\phi=\phi_1}^{\phi_2} d\phi = \phi_2 - \phi_1. \quad (6)$$

We have replaced the symbol η in Xie and Nuttli (1988) by ϕ in order to avoid confusion with the frequency dependence of Q in equation (7) of this paper. Equation (6) is obtained using equations (A1) through (A5) of Xie and Nuttli (1988) but is more general than equation (A5) because here we have generalized the limits of integration for ϕ . When part of the integration path, which is an

ellipse, is missing, the numbers ϕ_1 and ϕ_2 can be found using equation (A4) of Xie and Nuttli (1988). An example of this situation is the case when the ellipse intercepts a continental boundary which is non-transmissive to Lg waves. Otherwise $\Delta\phi$ is 2π and the resulting G_m from equation (5) becomes

$$G_m = (2\pi R)^{-1/2} (v^2 \tau_m^2 / R^2 - 1)^{-1/4} . \quad (5')$$

The right-hand side of equation (2) is calculable from a coda time series.

Assuming a power law for the frequency dependence of Q

$$Q(f) = Q_0 f^\eta , \quad (7)$$

where Q_0 and η are Q at 1 Hz and the frequency dependence of Q , respectively, Xie and Nuttli (1988) used linear regression to find η and Q_0 from

$$\log F_k = (1-\eta) \log f_k - \log Q_0 + \epsilon , \quad (8)$$

where ϵ represents a random error. Both theoretical and observational calculations show that the SSR provides a statistically stable Q estimator, with the resulting standard error in Q_0 being an order of magnitude smaller than Q_0 itself.

A possible source of major systematic deviations of the Lg coda Q estimator from the Lg Q estimator is the use of an incorrect geometrical spreading term, G_m in equation (2). Using available observations conducted in various areas, including central Asia, North America, and southern Africa, Xie and Nuttli (1988) made a comparison between the Lg Q_0 and Lg coda Q_0 calculated from applying the single isotropic scattering (SIS) model to digital coda data, and concluded that the geometrical spreading term G_m calculated using the SIS model can be used to calculate the value of Lg coda Q_0 and that that value is close to Lg Q_0 averaged over the same area. These areas have widths of about 10^3 km. This conclusion is semi-empirical and many aspects on the the generation of Lg coda still remain unclear. For instance, we do not yet understand the details of mode conversion, nor why the SIS model appears to be valid. A further complication is that the stochastic modeling of Lg coda may be non-unique (Xie and Nuttli 1988).

§2.2 Spatial interpretation of single trace coda Q measurements

In order to obtain an image of lateral variation of Lg coda Q which closely resembles the

lateral variation of Lg Q, one has to interpret single-trace measurements of Lg coda Q in terms of laterally varying Lg Q, *ie.* one has to make an *a priori* assumption about how the single-trace measurements of Lg coda Q depend on the laterally varying Lg Q inside the area sampled by Lg coda. From considerations of the afore-mentioned non-uniqueness in modeling Lg coda and the unclear aspects of Lg coda generation, we think it is premature to assume a detailed, perhaps non-linear, functional relationship of such a dependence to image lateral variation of Lg Q. Additional problems in any attempt at using such a detailed functional relationship comes from the tremendous computation time and computer storage involved, and the probability of numerical instabilities (Xie and Mitchell, 1988). On the other hand, the Lg coda time series is typically longer than 300 seconds, thus the moving window stacking defined by equation (2) utilizes many windows and results in a stable measurement of Q. Assuming an Lg group velocity of 3.5 km/s and single scattering, the area sampled by the single trace Lg coda will always have a width greater than 10^3 km. This distance is about the same as the widths of the areas over which the consistency between averaged Lg Q_0 and Lg coda Q_0 were observed (§2.1). Therefore we assume that the inverse of Lg coda Q obtained by applying the SSR method (with G_m calculated from the SIS model) to a single-trace record of Lg coda gives the areal average of Lg Q^{-1} inside the elliptical area corresponding to the maximum τ_m , which will be denoted as τ_{max} , of this record. The major and minor axes of this ellipse are given respectively by

$$a = vt/2 \Big|_{t=\tau_{max}} \quad (9)$$

where v is the same as in equation (4), and

$$b = \sqrt{v^2 t^2 - R^2} \Big|_{t=\tau_{max}} \quad (10)$$

where R is the epicentral distance (Xie and Nuttli 1988, equations (A3) and (A4). Note that $r_1 + r_2 = vt$ and that the delta function in equation (A3) results in α being equal to vt/R).

Since the τ_{max} of a coda record, under the single-scattering assumption, gives the largest possible area sampled by the Lg coda, the above assumption attributes each coda Q value measured from a single-trace record to the average Lg Q over the largest possible area. We will use this assumption exclusively in imaging lateral variations of Q. We note that strictly speaking the

image of lateral variations of Q obtained using such an assumption is the image of lateral variations of Lg coda Q , which, as indicated in the above discussion, should closely resemble the lateral variations of Lg Q .

It appears that the above assumption will lead to limited resolving power in the imaging of lateral variation of coda Q . Previous practice in determining lateral variations of coda Q (Singh and Herrmann, 1983; Raoof and Nuttli, 1985; Jin and Aki, 1988) have assigned single-trace Q measurements to spatial points, instead of areas. We think that our assumption is more reasonable since high-frequency seismic coda samples an area rather than a spatial point. Moreover, spatial resolution in imaging lateral variations of coda Q is also limited by the random nature of the high-frequency coda signal. This causes more basic and more severe restrictions in resolution compared to any restrictions artificially caused by the assumptions used in our inversion. This basic restriction is very important and profound but has not been addressed previously. We shall give a detailed discussion on this limitation in the following paragraphs.

There is a trade-off between the stability of single-trace coda Q measurements and spatial resolution. As mentioned by Kopnichev (1980), Der *et al.* (1984) and Xie and Nuttli (1988), the high-frequency Lg coda is highly random. Thus in order to estimate coda Q using spectral ratios, stacking techniques should be used to overcome large variances or uncertainties. Stacking can be applied either to coda data from repeated paths if they are available, or to coda obtained from many time-shifted windows applied to the same single trace. Moving-window stacking (Xie and Nuttli, 1988) can provide better data coverage since only one record is required for multiple measurements. In this method, as one moves toward later parts of the coda, the area sampled by the signal successively increases and the spatial resolution becomes poorer. This is a special case of the usual trade-off between variance and resolution in inverse problems (Bakus and Gilbert 1970). In measuring coda Q using the master curve method (Herrmann, 1980), better constrained coda Q estimates require use of predominant frequencies measured from the later part of coda, unless Q is very low (Singh and Herrmann 1983, Xie and Nuttli 1988). The method of Aki and Chouet (1975) applies linear regression to amplitudes over lapse time for each of several frequency pass-

bands. More data points are needed in these regressions to reduce the uncertainty in the estimation of slope (which gives Q); thus the later part of coda is also needed in the method of Aki and Chouet. Therefore to stabilize the Q -inversion using the random coda signal, the later part of coda is needed, regardless of the method used. The increased stability and the reduced uncertainty due to using the later coda, however, is achieved at the cost of poorer spatial resolving power of later coda since it samples a larger area. Eventually one achieves an acceptable uncertainty in coda Q inversion with limited spatial resolution. Compared to this primary limitation in the spatial resolution inherent in narrow-band random coda signal, the limitations associated with our assumptions are secondary and probably trivial. At short distances the low-pass effect of attenuation is not as serious as it is at large distances where Lg coda is observed; therefore for local S-wave coda recorded by broad-band instruments, the variance could be reduced by increasing $2l+1$ (equation (1)) at the cost of frequency resolution if the SSR method is used, and the trade-off could be set toward a higher spatial resolution.

§ 2.3 Method of imaging lateral variations of Lg coda Q

In this section we propose a back-projection algorithm to image lateral variations of Lg coda Q . Suppose we have a number (N_d) of Lg coda time series collected from a continental region. We shall denote the Q value calculated by applying the SSR method to the n th time series by $\overline{Q_n}$. We divide the whole area under study into a number of N_g grids with widths of W_{NS} degrees in a north-south direction and W_{EW} degrees in a east-west direction. We parameterize the unknown lateral variation of Lg coda Q by assuming it to be a constant (Q_m) inside the m th grid. Following the assumption in §2.2, $\overline{Q_n}$ gives the areal average of Lg Q (strictly speaking, Lg coda Q) in the elliptical area sampled by coda waves received at the maximum lapse time, τ_{max} , of the whole time trace. Denoting the area that the n th ellipse overlaps with the m th grid by s_{mn} , we have

$$\frac{1}{\overline{Q_n}} = \frac{1}{S_n} \sum_{m=1}^{N_g} \frac{s_{mn}}{Q_m} + \epsilon_n, \quad n=1,2,\dots,N_d, \quad (11)$$

where

$$S_n = \sum_{j=1}^{N_g} s_{jn}$$

and ϵ_n is the residual due to the errors in modeling Lg coda and in the Q measurement. Equation (11) is a sparse linear system because many of the s_{mn} 's are zero. We shall use a back-projection, or ART technique (eg., Gordon 1974, Dines and Lytle 1979, McMechan 1984, Suetsugu and Nakanishi 1985, Humphrey and Clayton 1988) to solve equation (11). This technique is an iterative "raw-action" procedure. Our adopted version of this technique to image lateral variation of Lg coda Q is briefly summarized as follows:

(1) calculate s_{mn} for all the (m,n)'s and store all the non-zero s_{mn} values.

(2) construct a starting model for Q_m 's, denoted by Q_m^i , for $m=1,2,3,\dots,N_g$, and $i=0$ (the superscript i will be used to indicate the last iteration completed over all the coda records).

(3) for each of the n records ($n=1,2,3,\dots,N_d$), calculate the updated residual Δ_n^i , defined through

$$\Delta_n^i = \frac{S_n}{Q_n} - \sum_{m=1}^{N_g} \frac{1}{Q_m^i} s_{mn} \quad (12)$$

(4) for each of the m grids ($m=1,2,\dots,N_g$), a new estimate of Q_m , denoted by Q_m^{i+1} , is made by back projecting Δ_n^i into the inverse of the Q_m^i 's:

$$\frac{1}{Q_m^{i+1}} = \frac{1}{Q_m^i} + \frac{1}{N_i} \sum_{n=1}^{N_d} \frac{\Delta_n^i s_{mn}}{\sum_{j=1}^{N_g} s_{jn}^2} \quad (13)$$

where N_i is number of ellipses overlapping with the ith grid.

(5) a nine-point spatial smoothing proposed by Suetsugu and Nakanishi (1985) is applied to smooth and stabilize the inversion. If we denote the mth grid by $m(l,j)$, where l and j are grid numbers in the east and north directions, respectively, then the smoothed model $(Q_m^{i+1}(l,j))'$ is given by

$$\begin{aligned} \frac{1}{(Q_m^{i+1}(l,j))'} = \frac{1}{29} & \left[\frac{1}{Q_m^{i+1}(l-1,j-1)} + \frac{1}{Q_m^{i+1}(l-1,j+1)} + \frac{1}{Q_m^{i+1}(l+1,j-1)} + \frac{1}{Q_m^{i+1}(l+1,j+1)} + \right. \\ & \left. + 4 \left(\frac{1}{Q_m^{i+1}(l,j-1)} + \frac{1}{Q_m^{i+1}(l,j+1)} + \frac{1}{Q_m^{i+1}(l-1,j)} + \frac{1}{Q_m^{i+1}(l+1,j)} \right) + \frac{9}{Q_m^{i+1}(l,j)} \right] \quad (14) \end{aligned}$$

This smoothing procedure is much like a spatial Gaussian filter, and we have found that unreasonably low (or even negative) Q^{-1} values could result if this smoothing is not applied.

(6) repeat the iterative procedures in (3) through (5) until one of the following criteria is satisfied:

$$i+1 \geq i_{\max} , \quad (15)$$

or

$$\frac{\sum_{j=1}^{N_d} (\Delta_j^{i+1})^2 - \sum_{j=1}^{N_d} (\Delta_j^i)^2}{\sum_{j=1}^{N_d} (\Delta_j^i)^2} \leq \delta^2 \quad (16)$$

where i_{\max} is an integer which gives the maximum iteration acceptable and δ is the relative change in the overall residual, or the relative improvement of the degree to which the model fits data. Both numbers were chosen by experience after several tests of the method. Both i_{\max} and δ are set before the iteration procedure begins.

The advantages of using back-projection techniques include the minimal computer storage involved, and the rapid convergence achieved. These advantages are very important when an entire continent is being studied. The disadvantage of using this technique is that back-projection does not provide formal estimates of resolution, bias, and error (Suetsugu and Nakanishi 1985). Humphreys and Clayton (1988) suggested using the "point spreading function", which we shall denote as p.s.f., as an approximation of the resolution kernel. To obtain the p.s.f. one simply constructs a model composed of one grid with unit-valued Q^{-1} at the geographic point of interest. The Q^{-1} values in all the other grids are set at zero. Synthetic data using this model are then computed and inverted. The resulting image gives the p.s.f. at this geographic point, which in turn gives a measure of spreading of the resolution kernel.

The effect of random noise preserved in single-trace Q estimates on the final image can be empirically tested utilizing the sample standard error in $\overline{Q_n}$ due to the randomness of the SSR's (Xie and Nuttli 1988). To do so we denote the standard error associated with $\overline{Q_n}$ by δQ_n , $n=1,2,3,\dots,N_d$ (note that δQ_n is always positive due to the way standard error is estimated), and assume that δQ_n gives a good measure of the absolute value of real error preserved in the corresponding $\overline{Q_n}$ measurements. We then empirically construct a number, N_d , of noise series,

whose n th member have an absolute value equal to δQ_n and a sign that is chosen randomly. The n th term of this noise series is then added to $\overline{Q_n}$ to construct a new set of $\overline{Q_n}$, which we shall denote as

$$\overline{Q_n}^T = \overline{Q_n} + \delta Q_n .$$

$\overline{Q_n}^T$ values were then inverted to obtain a new Q_m model. The difference between the new image of Q_m values using $\overline{Q_n}^T$ and the original image of Q_m values will give us an error estimation for the Q_m values. This process empirically measures the effect of random noise on the Q_m image. The sign of the δQ_n series can be simulated by pseudorandom binary generators in a computer and the process must be repeated several times to obtain an averaged, and more stable error measurement of Q_m values.

3. DATA PROCESSING

In this study we have used Lg coda records collected from vertical-component, short-period seismographs installed at 12 stations in continental Africa. Table 1 lists the instrument types of these seismographs, and the codes and locations of the stations. The station locations are also plotted in Figure 1, where the Ivory Coast Array stations are clustered together and abbreviated as ICA. The data set is composed of the following:

(1) 59 digital records from stations BCAA and SLR, both belonging to the DGSN network. Events recorded by these stations occurred in the years 1979 through 1985.

(2) 155 analog records from WWSSN stations AAE, BUL, GRM, HLW, NAI, PRE, SDB and WIN. Events recorded by these stations occurred primarily in the years 1973 and 1974, but two nuclear explosions occurred on October 20, 1963 and February 27, 1965.

(3) 39 analog records from the Ivory Coast Array stations. 12 events recorded at these stations occurred during the years 1978 through 1984. The Ivory Coast Array has five short-period (~ 1 Hz), vertical seismographs with an instrument response similar to that of WWSSN instruments. These seismographs are located within tens of kilometers of each other. Four of them are high-gain instruments (magnification $\geq 125k$), and one is low-gain (magnification = 62.5k). We have chosen to use three or four (depending on how many were available to us with acceptable

record length and signal/noise ratios) of the records from the high-gain instruments in this study. The response of these instruments varied quite frequently during the years of recording events, but these variations have no effect when the SSR method is used (Xie and Nuttli 1988).

All of the analog seismograms were digitized at St. Louis University. Figures 2 and 4 display some typical digitized seismograms from WWSSN and Ivory Coast Array stations, respectively. Together with the digital seismograms, we have a total number of 253 Lg coda time series. This makes the digital Lg coda data set used in this study the largest ever collected for a major continent. Each of the coda time series were segmented by many windows with the centered lapse time, τ_m , starting at roughly the arrival of group velocity of 3.15 km/s and increasing to successively cover the entire portion of the signal which can be distinguished from the ambient noise. We used a 10 percent Hanning window with a length of 30 seconds for the digitized analog data and a length of 25.6 seconds for the digital GDSN data. The reference noise spectra for each record were obtained in the way described by Xie and Nuttli (1988), i.e., from the portion of the trace prior to the P arrival. The Fast Fourier Transform (FFT) was performed on both signal and noise and the effect of noise was empirically reduced by subtracting the reference power spectra of noise from power spectra of the signal. The SSR, defined by equation (2), was then obtained for single-trace Q measurements. Table 2 lists the event dates, recording stations, epicentral distances, back-azimuths and the resulting single-trace measurements of Lg coda Q, together with the estimated standard errors. Figure 3 gives some examples of the SSR analysis using the digitized WWSSN records displayed in Figure 2. The frequency band used is from 0.5 Hz to 2.0 Hz. It is noteworthy that the SSR estimated from the event dated 05-14-74 recorded by station BUL (middle of Figure 1) fluctuated more than others, perhaps because of fundamental-mode interference. Some examples of SSR analysis using GDSN data can be found in Xie and Nuttli (1988). All of the events recorded by the Ivory Coast Array were a few thousand kilometers from the stations, giving virtually the same travel-times to all the stations (Table 1). In this case we have treated the records of the same event collected from all the available stations belonging to this array as records of a repeated path and obtained a more stable Q measurement by averaging the SSR over

the whole array. This permitted us to use a shorter coda time series (roughly 200 to 300 seconds), but to still have rather small sample standard errors. Figures 4 and 5 give examples of this averaging process. Figure 4 shows the time traces and Figure 5 shows the SSR's calculated from each station (curves), their average (dots), and the linear regression over the average (line), together with the resulting Q_0 and η (denoted by z in the plot), and their standard errors.

The lengths of the coda time series we used are between 200 seconds and 800 seconds. We have determined the sampling areas of these coda records under the assumptions that each coda time series samples an elliptical area with axes given by equations (9) and (10) and that the boundary separating oceanic crust from continental crust forms a non-transmissive barrier to the Lg wave. When such a boundary is encountered by the Lg wave coming from the continental side, some part of the energy carried by this wave is scattered back into the continental side and the remaining energy is converted into other types of seismic waves which propagate into the oceanic crust or mantle. We further assume that the scattering at this boundary is isotropic and is not abnormally strong, compared to the scattering caused by scatterers inland. When part of the ellipse corresponding to τ_m , the centered lapse time of the m th window (Xie and Nuttli, 1988), is oceanic, equation (A4) of Xie and Nuttli has been used to determine the limits of integration (ϕ_1 and ϕ_2 in equation (6) of this paper), to exclude the oceanic crust and to determine the new geometric spreading term, G_m . Our assumption of the absence of abnormally strong scattering (or reflection) of Lg waves toward the receiver by the continental boundary is not necessarily valid in all cases. Although there have been some qualitative demonstrations of the possibility of this type of scattering or reflection, quantitative estimates of its effects are not possible at the present time (Kennett 1986). If abnormally strong scattering or reflection does occur at the continental margin our image of lateral variation of Lg coda Q obtained may be biased near those margins.

The assumption of non-transmissibility at continental margins allows us to exclude any oceanic crust in the scattering ellipse in the Lg coda Q analysis. Figure 6 shows the pattern of coda sampling area corresponding to our data set. These areas are bounded roughly by complete ellipses corresponding to τ_{\max} (equations (9) and (10)) but some are truncated by the continental margin.

The

density of coverage of these coda sampling areas decreases from south to north. Southern Africa has the densest coda sampling area coverage whereas northern Africa has the sparsest. For each of the records, the SSR method was applied to obtain a single-trace measurement of Q_0 and η . Examples of the SSR analysis may be found in Xie and Nuttli (1988) and in Figures 3 and 5 of this paper. Most data provide information in the frequency band between 0.5 Hz and 2.0 Hz but digital GDSN data sometimes has high-frequency cut-offs that are higher than 2.0 Hz. Occasionally, when large-amplitude fundamental-mode waves distort coda signal at lower frequencies, we use slightly higher low cut-off values. The results of single-trace determinations of Q_0 and η , together with the sample standard error(s.s.e.), are listed in Table 2. The s.s.e. values of Q_0 are almost all within 15% of Q_0 and the s.s.e. values of η are mostly within 0.2. This is consistent with the stochastic model mentioned in §2.1 of this paper.

4 LATERAL VARIATIONS OF LG CODA Q

The back projection method in §2.3 is applied to image lateral variations of Lg coda Q in continental Africa. We have divided the whole area into 282 grids with widths W_{EW} and W_{NS} equal to 3° in latitude and longitude, respectively. The latitudes and longitudes of the centers of the grids span the area between 31.5°S , 34.5°N and 14.5°W , 48.5°E . To find the area sampled by each coda trace we first found the corresponding ellipse in a two-dimensional Cartesian coordinate system, and projected this ellipse onto the surface of the Earth. Strictly speaking, on a surface with non-zero curvature, an isocron of scatterers corresponding to coda waves received at a constant lapse time is not an ellipse but a more complicated curve. However we have found that when the axes of ellipses are shorter than approximately 2200 km the difference between the isocron obtained considering the Earth's curvature and the ellipse defined in a Cartesian system without considering the Earth's curvature differs by less than two percent. Since G_m corresponding to an isocron when the Earth's curvature is considered does not have a closed-form solution and since all but a few ellipses in this study have major axes longer than 2200 km, we have ignored the effect of the Earth's curvature on Q imaging.

4.1 Lateral variation of Q_0

To use the iterative back projection method in §2.3 to image lateral variations of Lg coda Q_0 , we have used a starting model of $Q_m^0 \equiv 600$, $m=1,2,\dots,N_g$ for all of continental Africa. This starting model is roughly the average of all of the single-trace measurements of Q_0 (Table 2). Single-trace measurements of Q_0 were then used as $\overline{Q_n}$ in §2.3 to calculate the residuals in the iteration. The stopping criteria, i_{\max} and δ , defined by equations (15) and (16), were chosen to be 20 and 10^{-5} , respectively. The latter criterion was satisfied after 14 iterations. The whole computational process, including calculation of s_{mn} values, took less than 90 minutes and less than 25 minutes of CPU time on a Masscomp MC745 and a Ridge-34 minicomputer, respectively. The variance reduction achieved was 95%. After 15 iterations the left hand of (16) started to increase slightly, probably due to the accumulation of computer round-off errors. The resulting Q model did not vary significantly after the 14th iteration. Figure 7 shows the resulting distribution of Q_0 in continental Africa. Circles represent Q_0 values lower than 570 and crosses represent Q_0 values higher than 570. Each symbol represents a Q_0 interval of 60, *eg.* the smallest circle represents a Q_0 value between 510 and 570. The lateral variation of Q_0 is rather smooth, indicating that only large-scale variations of Q_0 are preserved. Low Q_0 values are most apparent in the East African Rift zone and the Cameroon rift (or the Cameroon volcanic line, *cf.* Moreau *et al.*, 1987). Previous single-path observations of the direct Lg phase travelling through segments of the East African Rift also indicate low Q values in that region (Gumper and Pomeroy 1970). Low Q_0 values also occur near the southern and northern margins of Africa, where the Cape Fold Mountains and Atlas Mountains are located (Figure 1). High Q_0 values occur in central southern Africa where the Congo craton and Kalahari Craton are located, in northwestern Africa where the west Africa craton is located (Clifford 1970, Cahen *et al.* 1984), and in northeastern Africa. The latter area contains the highest mapped Q_0 values. Although this region has undergone a complicated tectonic history (Cahen *et al.* 1984), it has not been affected by either large-scale orogeny or volcanic activity for about the last 550 million years and some basement outcrops in this area are dated at ages greater than two billion years (Klerkx 1980).

§4.2 Lateral variation of η

Imaging the lateral variation of frequency dependence, η , requires another procedure. First, we obtained Q_0 and η for each coda record using the SSR method. This allowed us to calculate single-trace measurements of Q at a frequency other than 1 Hz, say at 3 Hz. These single-trace measurements were then used as $\overline{Q_n}$ in equations (11) and (12) to calculate Q_m values at 3 Hz for each of the m grids, $m=1,2,\dots,N_g$. Finally, using Q_m for each grid calculated at 1 Hz (§4.1) and 3 Hz and assuming exponential frequency dependence of Q , we calculate η for the same grid using the relationship

$$\eta = \frac{1}{\ln 3} \ln \left[\frac{Q(f)|_{f=3\text{Hz}}}{Q_0} \right]. \quad (17)$$

Figure 8 shows the resulting lateral variation of η in continental Africa. In southern Africa, the frequency dependence is relatively uniform (between 0.3 to 0.5), but is slightly lower (around 0.2 to 0.3) in central southern Africa, than near the southern margin. η is about 0.5 in the region of the East African Rift system. The areas where η values are slightly higher in southern Africa are also areas where Q_0 is lower (Figure 7). Near the equator in central Africa (between 10°S and 10°N), η is very uniformly distributed, being about 0.5 inland and about 0.6 in coastal areas. In northern Africa η exhibits significant lateral variations. Even if the extreme values near the western and northeastern margins are ignored (because sampling coverage is poor), there is still a large change in η from about 0.8 in the West African shield to about 0.1 in the northeastern Africa even though Q_0 is high in both regions. Our images of lateral variation of η and Q_0 do not therefore suggest a systematic correlation between Q_0 and η throughout the whole continent. If northwestern Africa (where the west African shield is located) is ignored, however, then η appears to decrease as Q_0 increases. This tendency is most easily seen in northeastern Africa and southern Africa. Nuttli (1988) suggested that this relation is generally true throughout the world.

5. RESOLUTION AND ERROR

The imaging of Lg coda Q variations is inherently limited because of the trade-off between the stability and the spatial resolving power (§2.2). For this reason it is important that any study of Lg coda Q variations include an analysis of resolution and error.

We have calculated the p.s.f. defined in §2.3 for 12 grids (Figures 9(a) through 9(g)) to estimate the resolving power at the locations where these grids are centered. These locations include: 31.5°S, 24.5°E (Figure 9(b)); 28.5°S, 18.5°E (9(c)); 19.5°S, 30.5°E (9(d)); 13.5°S, 24.5°E (9(a)); 13.5°S, 24.5°E (9(d)); 1.5°N, 30.5°E (9(b)); 4.5°N, 21.5°E (9(f)); 7.5°N, 39.5°E (9(g)); 13.5°N, 39.5°E (9(e)); 19.5°N, 3.5°E (9(d)); 19.5°N, 18.5°E (9(c)); 19.5°N, 33.5°E (9(a)). All of the p.s.f. determinations were normalized such that the maximum values are unity. In general, the degree of spreading of p.s.f.'s increases from south to north. This is to be expected since the coda sampling areas are relatively dense in southern Africa and are less dense toward the north (Figure 6). The p.s.f. plots in Figures 9(a) through 9(d) show that in southern Africa the lateral variation of Lg coda Q is resolvable to spatial wavelengths of between 6 and 20 degrees. Slightly lower resolving power is obtained in the central part of Africa where the degree of spreading of p.s.f. plots is as low as 12 degrees at 7.5°N and 39.5°E (Figure 9(g)) and increases to between 15 and 24 degrees further to the west (Figures 9(b) and 9(f)). In the north the resolving power decreases drastically, except for some points close to continental margin where resolution spreading is still very low (around 12 to 15 degrees, see Figures 9(a) and 9(e)). For example, at 19.5°N, 18.5°E (Figure 9(c)) and 19.5°N, 3.5°E (Figure 9(d)) we cannot determine the lateral variation of Lg coda Q with confidence for spatial wave lengths of less than between 24 and 33 degrees. In summary, the spatial wavelengths of lateral variation in Lg coda Q that are resolvable range from about 10 degrees in southern Africa to 30 degrees in northern Africa.

It is interesting to compare our resolution in imaging lateral variation in Lg coda Q to the resolution of two-dimensional surface wave velocity tomography. Several authors have conducted studies of lateral variations of long-period surface wave phase and/or group velocities in recent years. Suetsugu and Nakanishi (1985), Montagner (1986), and Hadiouche and Jobert (1988) mapped lateral variations of surface wave dispersion in the Pacific Ocean, the Indian Ocean, and Africa, respectively, using data at periods between a few seconds and a few hundred seconds. In all these studies the spatial resolving power was generally limited to wavelengths of 15 to 20 degrees or more. Resolving power in some cases was locally limited to 40 degrees for situations where the

ray coverage was poor (Suetsugu and Nakanishi 1985). Therefore the resolving power in this study using Lg coda waves at frequencies between roughly 0.5 and 2.0 Hz is comparable to that achievable in surface wave tomography at longer periods. This is somewhat surprising since surface wave tomography uses direct paths whereas imaging of lateral variations in the Lg coda Q uses scattered waves, thus requiring smoothing over broader areas. A closer look at this comparison suggested that the resolving power of surface-wave tomography is limited by gaps between ray paths which are typically about 20 degrees. The smoothing techniques used in surface-wave tomography remove these gaps in the inverted velocity image at the cost of resolution. The limitations in resolution in the present study are, however, largely due to the random nature of coda data itself (§2.2). Moreover the Q image may be subjected to greater systematic errors in the single-trace measurements of Q and in their spatial interpretation than are velocity images from surface waves.

The effect of the random error in single trace measurements of Lg coda Q on the image of lateral variations in Q was estimated empirically using the method described in §2.3. Five tests were run to estimate the error in the image of Q_0 and η . In each of the five tests we first constructed two noise, or error series. The absolute values of the n th terms of the first and the second series equal the sample standard errors in Q_0 and η calculated from the n th coda seismogram, respectively. The signs of the n th term of both noise series were randomly generated by a random binary generator. The n th terms of the two noise series were then added to the n th Q_0 and η measurements to construct a new synthetic set of Q_0 and η values. The new sets of synthetic Q_0 and η values were then inverted using the back projection method to obtain Q_0 and η for all of the grids. The differences between the Q_0 and η values for the new image and the original image were then calculated and stored at the end of each test. After all five tests, the absolute values of the five differences in Q_0 and η for each grid were averaged. The averaged values thus obtained gave empirical estimates of absolute error in the imaged Q_0 and η values. Figures 10 and 11 give the estimated errors in Q_0 and η , respectively. The errors in Q_0 are small (less than 60) throughout most of Africa. Errors are higher, however, in western Africa and northeastern Africa, where the

Q_0 values are high (Figure 7). Since the relative error in Q_0 tends to have a stochastic distribution (Xie and Nuttli, 1988), the increased error in western and northeastern Africa must be partly due to the high Q_0 values. The second reason for these increased errors is the poor spatial coverage, especially along the western margin of the continent where the estimated error is as high 300. The estimated error in η is small (0.0 to 0.1) throughout most of interior Africa and is generally higher at the margins. The error in η at the northern margin is typically between 0.3 and 0.4 and is 0.5 in the region of the western margin where sampling is very poor. These calculations indicate that the errors in both Q_0 and η are inversely related to the density of the coda sampling area.

6. RELATION OF Q VALUES TO GEOLOGICAL FEATURES

The map of Q_0 values in Figure 7 exhibits broad regional variations of Q_0 values ranging between about 960 and about 360. The higher values are similar to those found in other stable regions of the world. Since almost all of Africa has been stable for the past 500 million years (Clifford, 1970; Cahen *et al.*, 1984), we might expect that high Q values would be typical of most of the continent. It is therefore interesting to speculate on the mechanism for the regions of low Q which are observed.

The most obvious region of high attenuation (low Q) occurs in eastern Africa and correlates well with the east African Rift system (Figure 1). This is a region which has been subjected to extensive Cenozoic volcanism and is characterized by Lg coda Q_0 values as low as 360. Although these values are lower than those for most of Africa, they are not as low as those found throughout much of the western United States where Cenozoic volcanism has occurred (Singh and Herrmann 1983). The values in Figure 7 are, however, averages over broad regions including rift areas as well as areas where volcanism has not occurred. It is possible that our results are averages of lower values occurring in the immediate vicinity of the rifts and higher values occurring between and outside the arms of the rifts.

The low Q values in the region of the East African Rift system can be explained as resulting ultimately from higher than normal temperatures in the crust. Morgan (1982) reported a pattern of heat flow values in which high values (up to 98 mW/m²) occur on the rift floor and lower values

(57 mW/m²) occur on the flanks. Mitchell (1975, 1980) proposed that such higher temperatures caused enhanced levels of hydrothermal fluids in the crust; thus low values of crustal Q can be explained by fluid flow through cracks and connected pore space in the crust by mechanisms such as those proposed by Winkler and Nur (1979) and O'Connell and Budianski (1977).

The Cameroon line running northeastward from the coast in west-central Africa appears to be characterized by relatively low values of Q_0 (about 540). This region is also the site of Cenozoic volcanism, so can be expected to have higher than normal heat flow. Its extent, however, is smaller and reductions in Q are less severe than in the East African Rift system.

The lowest values of Q outside the East African Rift system lie in the region of the Cape Fold Belt in southernmost Africa. Orogenic activity occurred there over the time span from middle Paleozoic to early Mesozoic (Clifford 1970). Although the low Lg coda Q values in southern Africa appear to be associated with the Cape Fold Belt, the mechanism for the low values is uncertain. They can be explained either by reductions of intrinsic Q produced by interstitial fluids (Mitchell, 1975, 1980) or by disruption of the crustal wave guide caused by severe topography and fluctuating thickness of sediments. Higher than normal heat flow values in much of southern Africa (Jones, 1988), however, may be suggestive of the former mechanism.

Low Q_0 values (about 540) in northwestern Africa correlate geographically with the Atlas Mountains. These mountains are the result of the most recent orogenic activity in Africa, thus low Q values might be expected to occur in that region.

A broad band of low Q_0 values (about 600) runs in a southeasterly direction from a portion of the Atlas Mountains near Gibraltar, crosses the Cameroon line, and continues southeastward to about 10° S latitude. Except near the Cameroon line and Atlas mountains, these low values cannot be related to any recent orogenic or volcanic activity in Africa. They do, however, correlate with a broad region of Mesozoic and younger sediments which is mapped in that region (Choubert and Faure-Muret 1971). Mitchell and Hwang (1987) showed that all of the regional variations of Lg coda Q in the stable portions of the central United States can easily be explained by high attenuation caused by accumulations of sediments of Mesozoic age and younger.

In summary, Q values throughout most of the Africa are high or relatively high and are consistent with values obtained in other stable regions of the world. Low values occur in regions of Cenozoic volcanism and in the two small regions (Cape Fold Belt and Atlas Mountains) where orogenic activity has occurred as recently as the Mesozoic Era. Somewhat low values appear to be associated with broad regions of sedimentary cover of Mesozoic age.

7. CONCLUSIONS AND DISCUSSION

Taking advantage of recent developments in both more stable single-trace measurements of Lg coda Q and in the rapid evolution of seismic tomography, a computerized back projection method is proposed to image large-scale lateral variation of Lg coda Q . Several major differences can be recognized between this method and the earlier contouring methods used by various authors. First, this method assumes that each Lg coda time series samples an area rather than a spatial point, thus better approximating the real coda sampling process. Second, this method is fully computerized and quantitative, yet requires very small computer memory and time. Even when a major continental area is studied, a minicomputer is more than adequate. This new method also allows quantitative estimates of resolution and error. The analysis of resolution is especially important in coda Q inversion because of the inherent randomness of signal which limits resolution.

We have collected a large amount of digital and digitized Lg coda data from continental Africa. Applying the back projection method to this data base, we find that the lateral variation of Q_0 (Q at 1 Hz) correlates well with major tectonic features. The Cape Fold Belt, the Atlas Mountains, the East African rift and Cameroon rift (or the Cameroon volcanic line) are characterized by relatively low Q values whereas the shields in southern and western Africa are characterized by high Q values. Northeastern Africa, another stable region, also has high Q values. In most regions the frequency dependence, η , increases with decreasing values of Q_0 . However, higher η values were also found in the West Africa Shield where Q_0 is high. It is possible that larger errors or poorer resolution in western Africa has caused this inconsistency.

A quantitative resolution analysis indicates that the resolving power of the Lg coda Q

image in continental Africa is limited to spatial variations with wavelengths ranging between 10 and 30 degrees. This is comparable to the resolving power of long-period surface-wave tomography applied in earlier studies. The resolution is best in southern Africa where the coda sampling area is densest. The error analysis shows that the errors in the images of both Q_0 and η inversely correlate with the density of coda sampling area. For most of interior Africa the error in the imaged Q_0 is lower than 60 and the error in the imaged η is less than 0.2. The largest errors occur near the northern and western margins of Africa.

Our knowledge of both the distribution and characteristics of scatterers is limited, and the quantity of available data is still very small. These limitations currently prevent us from obtaining detailed knowledge of the physical process which governs the generation and propagation of the Lg coda wave. Our assumption that a single-trace measurement of Lg coda uniformly samples an elliptical area limits the resolving power of this imaging process. A non-linear approach may overcome this limitation (Xie and Mitchell, 1988), but errors in the forward modeling procedure and in the final image are likely to be larger. A non-linear approach will also greatly increase computer time and will require a very large amount of computer storage. For the present, therefore, it is preferable and more convenient to have lower resolving power than to attempt to achieve greater detail with a non-linear approach. Future work should include systematic studies of more detailed interpretations of the dynamic properties and stochastic characteristics of Lg and Lg coda, which, if combined with an increased data base, should enable us to improve the resolution and quality of the Q image.

ACKNOWLEDGEMENTS

We express our gratitude to the late Otto W. Nuttli, who initiated our interest in lateral variations of Lg coda Q in Africa, helped us to obtain the necessary data and shared his experience in the interpretation of Lg and Lg coda. We also thank Dr. R.B. Herrmann for helpful discussions, two anonymous reviewers for providing helpful suggestions, and Dr. B. Massinon of Laboratoire de Detection et de Geophysique (L.D.G.), France for providing us a large package of seismograms from the Ivory Coast Array stations. R.B. Herrmann, E.J. Haug, S. T. Morrissey and

H.A.A. Ghalib assisted in implementing our computational procedures on minicomputers at The Department of Earth and Atmospheric Sciences, St. Louis University. This research was supported by the Advanced Research Projects Agency of the Department of Defense and was monitored by the Air Force Geophysics Laboratory under contract F19628-87-K-0036.

REFERENCES

- Aki, K. & Chouet, B., 1975. Origin of coda waves: source, attenuation and scattering effects, *J. Geophys. Res.*, **80**, 3322-3342.
- Backus, G. & Gilbert, F., 1970. Uniqueness in the inversion of inaccurate gross earth data, *Philos. Trans. R. Soc. London*, **266**, 123-192.
- Bolt, B.A., 1976. *Nuclear Explosions and Earthquakes, the Parted Veil*, W.H. Freeman and Company, San Francisco, pp.309.
- Cahen, L., Snelling, N.J., Delhal, J. & Vail J.R., 1984. *The Geology and Evolution of Africa*, Clarendon Press, Oxford, pp.464.
- Campillo, M., 1987. Lg wave propagation in a laterally varying crust and the distribution of the apparent quality factor in central France, *J. Geophys. Res.*, **92**, 12,604-12,614.
- Cheng, C.C. and Mitchell, B.J., 1981. Crustal Q structure in the United States from multi-mode surface waves, *Bull. Seism. Soc. Am.*, **71**, 161-181.
- Choubert par G. & Faure-Muret A., 1971. Grand bassins sédimentaires de l'Afrique occidentale, in *Tectonics of Africa*, Unesco, Paris, pp. 602.
- Clifford, T.N., 1970. The structural framework of Africa, in *African Magmatism and Tectonics*, Clifford, T.N. & Gass I.G. (editors), Oliver & Boyd, Edinburgh, pp.461.
- Der, Z., Marshall, M.E., O'Donnell, A. & McElfresh T.W., 1984. Spatial coherence structure and attenuation the Lg phase, site effects, and interpretation of the Lg coda, *Bull. Seism. Soc. Am.*, **74**, 1125-1148.
- Dines, K.A. and Lytle, R.J. 1979. Computerized geophysical tomography, *Proc. IEEE*, **67**, 1065-1073.
- Dott, R.H. & Batten R.L., 1971. *Evolution of the Earth*, McGraw-Hill Inc., New York, pp. 649.
- Gordon, R., 1974. A tutorial on ART, *IEEE Trans. on Nuclear Science*, **NS-21**, 78-93.
- Gumper, F. & Pomeroy P.W., 1970. Seismic wave velocities and earth structure on the African continent, *Bull. Seism. Soc. Am.*, **60**, 651-668.
- Hadiouche, O. and Jobert N., 1988. Geographical distribution of surface wave velocities and 3-D upper mantle structure in Africa, *Geophys. J.*, **95**, 87-110.

- Herrmann, R.B., 1980. Q estimates using the coda of local earthquakes, *Bull. Seism. Soc. Am.*, **70**, 447-468.
- Humphreys E. & Clayton R.W., 1988. Adaptation of back projection tomography to seismic travel time problems, *J. Geophys. Res.*, **93**, 1073-1086.
- Jin, A. & Aki, K., 1988. Spatial and temporal correlation between coda Q and seismicity in China, *Bull. Seism. Soc. Am.*, **78**, 741-769.
- Jones, M.Q.W., 1988. Heat flow in the Witwatersand Basin and Environs and its significance for the South African Shield geotherm and lithospheric thickness, *J. Geophys. Res.*, **93**, 3243-3260.
- Kennett, B.L.N., 1984. Guided wave propagation in laterally varying media-I. Theoretical development, *Geophys. J. R. astr. Soc.*, **79**, 235-255.
- Kennett, B.L.N., 1986. Lg waves and structural boundaries, *Bull. Seism. Soc. Am.*, **76**, 1133-1141.
- Klerkx, J., 1980. Age and metamorphic evolution of the basement complex around Jadal al'Awaynat, in *The Geology of Lybia, part III*, Salem M.J. & Busrewil (Editors), Academic Press, London, 901-906.
- Knopoff, L., Schwab, F. & Kausel, E., 1973. Interpretation of Lg, *Geophys. J. R. astr. Soc.*, **33**, 389-404.
- Kopnichev, Y.F., 1980. Statistical models for the generation of coda and short-period Lg -phases and the results of their joint interpretation, *Izv. Akad. Nauk USSR. Earth Phys.*, **16** 99-108.
- McMechan, G.A., 1983. Seismic tomography in boreholes, *Geophys. J. R. astr. Soc.*, **74**, 601-612.
- Mitchell, B.J., 1975. Regional Rayleigh wave attenuation in North America, *J. Geophys. Res.*, **80**, 4904-4916.
- Mitchell, B.J., 1980. Frequency dependence of shear wave internal friction in the continental crust of eastern North America, *J. Geophys. Res.*, **85**, 5212-5218.
- Mitchell, B.J. & Hwang, H.J., 1987. Effect of low Q sediments and crustal Q on Lg attenuation in the United States, *Bull. Seism. Soc. Am.*, **77**, 1197-1210.
- Montagner, J.P., 1986. Regional three-dimensional structures using long-period surface waves, *Annales Geophysicae*, **4**, B, 3, 283-294.
- Moreau, C., Regnault, J-M., Deruelle, B. & Robineau, 1987. A new tectonic model for the Cameroon line, central Africa, *Tectonophysics*, **139**, 317-334.
- Morgan, P., 1982. Heat flow in rift zones, in *Continental and Oceanic Rifts*, Palmason, G., editor; *Geodynamics series*, **8**, American Geophysical Union, Washington D.C., Geological Society of America, Boulder, Colorado, pp 309.
- Nolet, G. 1987. Seismic wave propagation and seismic tomography, in: *Seismic Tomography with Applications in Global Seismology and Exploration Geophysics*, Nolet, G., D. (editor), Reidel Publishing Company, Dordrecht, pp 381.

- Nuttli, O.W., 1986. Yield estimates of Nevada test site explosions obtained from seismic Lg waves, *J. Geophys. Res.*, **91**, 2137-2152.
- Nuttli, O.W., 1988. Lg magnitudes and yield estimates for underground Novaya Zemlya nuclear explosions, *Bull. Seism. Soc. Am.*, **78**, 873-884.
- O'Connell, R.J. & Budianski, B., 1977. Viscoelastic properties of fluid-saturated cracked solids, *J. Geophys. Res.*, **82**, 5719-5735.
- Raoof, M. & Nuttli, O.W., 1985. Attenuation of high-frequency earthquake waves in south America, *Pure and Appl. Geophys.*, **22**, 619-644.
- Singh, S.K. & Herrmann, R.B., 1983. Regionalization of crustal coda Q in the continental United States, *J. Geophys. Res.*, **88**, 527-538.
- Snieder, R., 1987. Surface wave holography, in *Seismic Tomography with Applications in Global Seismology and Exploration Geophysics*, Nolet, G., D. (editor), Reidel Publishing Company, Dordrecht, pp 381.
- Suetsugu, D. & Nakanishi, I., 1985. Tomographic inversion and resolution for Rayleigh wave phase velocities in the Pacific Ocean, *J. Phys. Earth*, **33**, 345-368.
- Winkler, K. & Nur, A., 1979. Pore fluids and seismic attenuation in rocks, *Geophys. Res. Letters*, **6**, 1-4.
- Xie, J. & Mitchell, B.J., 1988. Tomographic imaging of large scale lateral variations in Lg coda Q, *EOS Trans.*, **69**, 1309.
- Xie, J. & Nuttli, O.W., 1988. Interpretation of high-frequency coda at large distances: stochastic modeling and method of inversion, *Geophys. J.*, **95**, 579-595.

Figure Captions

Figure 1. Map showing the locations of seismographic stations used in this study (triangles and circles), and areas that have been affected by orogenies or large-scale rifting in the last 425 million years (shaded areas): 1-the East African Rift system, 2-the Cameroon rift (or the Cameroon volcanic line) system, 3-the Atlas Mountains, 4-the Cape Fold Belt. Adopted from Clifford (1970), Dott & Batton (1971) and Cahen *et al.*(1984). ICA indicates the Ivory Coast Array.

Figure 2. Three typical short-period, vertical-component WWSSN seismograms showing Lg coda. The abscissa indicates the lapse time measured from the earthquake origin time. The seismograms were digitized from analog records. The station code, gain of the instrument, epicentral distance and back-azimuth (in degrees) are shown above each trace. The event date is indicated below each trace and the arrival times of group velocities of 3.15km/s are identified.

Figure 3 Q_0 and frequency dependence (denoted by η in text and by z in this plot) values and their standard errors obtained by linear regression using SSR values calculated from the records plotted in Figure 2. The frequency band used is 0.5 Hz-2.0 Hz. At lower frequencies the spectral ratio estimates in the middle plot (station BUL) shows some fluctuations, probably due to the fundamental-mode interference.

Figure 4. Typical short-period, vertical-component seismograms at three Ivory Coast Array stations showing the long duration of Lg and Lg coda. The abscissa indicates the lapse time. The event is the same for all of the traces. The station code, instrument gain, epicentral distance, and back-azimuth (in degrees) are above each trace. The event date is indicated below and near the beginning of each trace, and the arrival times of waves with group velocities of 3.50km/s and 3.15km/s are identified.

Figure 5. The SSR's calculated from each trace in Figure 4 (curves), their average (dots), and the result of regression fitting (line) over the average. The resulting Q_0 and frequency dependence (denoted by z in this plot) and the frequency band used are given above the figure.

Figure 6. Sampling pattern of Lg coda used in this study. Each record of Lg coda is assumed to sample an elliptical area corresponding to the maximum lapse time used in the analysis. When the continental boundary is encountered we assume it is a barrier to the Lg wave and therefore the sampling area is bounded by this boundary, instead of being bounded by the corresponding segment of the ellipse which extends into the ocean.

Figure 7 Lg coda Q_0 of continental Africa obtained in this study. Circles represent numbers smaller than 570 and crosses represent numbers larger than 570.

Figure 8 Frequency dependence (η) of Lg coda Q (in the vicinity of 1 Hz) in Africa. Circles represent η values smaller than 0.45 and crosses represent η values larger than 0.45.

Figure 9(a) Point spreading function (p.s.f.) plots for grids centered at 13.5°S , 24.5°E and 19.5°N , 33.5°E . The p.s.f. plots have been normalized such that the maximum value is unity. The center of each grid is marked by a large cross.

Figure 9(b) p.s.f. plots for grids centered at 31.5°S , 24.5°E and 1.5°N , 30.5°E .

Figure 9(c) p.s.f. plots for grids centered at 28.5°S , 18.5°E and 19.5°N , 18.5°E .

Figure 9(d) p.s.f. plots for grids centered at 19.5°S , 30.5°E and 19.5°N , 3.5°E .

Figure 9(e) p.s.f. plot for the grid centered at 13.5°N , 39.5°E .

Figure 9(f) p.s.f. plot for the grid centered at 4.5°N , 21.5°E .

Figure 9(g) p.s.f. plot for the grid centered at 7.5°S , 39.5°E .

Figure 10 Error distribution in the image of lateral variation in Q_0 on continental Africa. The error is tested empirically, based on the sample standard error in the Q_0 and η values calculated from real data and the psuedo-random sign generators. See text for details.

Figure 11 Error distribution in the image of lateral variation in η on continental Africa. The

error is tested empirically, in the same manner as that described in Figure 10.

Table 1. Seismographic Stations Used in This Study

Station Code	Latitude	Longitude	Type of Instrument [†]
AAE	9.0300° N	38.8000° E	WWSSN
BCAO	4.4335° N	18.5354° E	SRO
BUL	20.1430° S	28.6130° E	WWSSN
DIC	6.6700° N	4.7700° W	IC *
GRM	33.3133° S	26.5733° E	WWSSN
HLW	29.8580° N	31.2420° E	WWSSN
KIC	6.3606° N	4.7411° W	IC *
LIC	6.2244° N	5.2778° W	IC *
NAI	1.2739° S	36.8037° E	WWSSN
PRE	25.7533° S	28.1900° E	WWSSN
SLR	25.7349° S	28.2816° E	DWWSSN
TIC	6.6447° N	5.0200° W	IC *
WIN	20.1430° S	28.6130° E	WWSSN

[†] all instruments are short period, vertical component

* Ivory Coast Stations. These instruments have response similar to that of 1-Hz short-period WWSSN instruments.

Table 2. Events used and the corresponding results of single-trace analysis of Lg coda Q_0 , with sample standard errors.

Fvent Date	Origin Time †	Recording Station	Epicentral Distance(km)	Back Azimuth °	Q_0	η
102063	13h0m0.0s	AAE	3948.9	299.0	724 ± 67	0.3 ± 0.2
022765	11h30m0.0s	AAE	3949.5	299.0	690 ± 91	0.4 ± 0.2
010773	12h17m12.6s	AAE	468.2	207.5	454 ± 40	0.5 ± 0.1
011373	6h5m42.2s	AAE	3076.5	201.9	510 ± 83	0.5 ± 0.1
011473	13h36m59.8s	AAE	1991.2	208.5	461 ± 53	0.5 ± 0.1
030573	23h59m46.6s	AAE	2133.2	346.0	712 ± 89	0.3 ± 0.2
040173	6m29m27.7s	AAE	534.2	57.4	449 ± 49	0.5 ± 0.1
040573	1h59m12.6s	AAE	906.0	66.2	493 ± 54	0.5 ± 0.1
040773	19h17m38.7s	AAE	530.0	55.0	518 ± 34	0.5 ± 0.1
041373	14h13m56.9s	AAE	633.4	59.0	468 ± 61	0.5 ± 0.1
041573	13h13m33.4s	AAE	2024.7	208.1	452 ± 61	0.5 ± 0.3
042273	22h3m43.5s	AAE	1014.1	236.6	499 ± 52	0.5 ± 0.1
051473	20h16m26.8s	AAE	1951.7	210.7	475 ± 56	0.5 ± 0.1
052473	7h15m8.5s	AAE	2211.0	194.7	478 ± 75	0.5 ± 0.2
070773	16h4m9.9s	AAE	1387.7	195.2	425 ± 62	0.6 ± 0.2
071873	19h39m13.0s	AAE	2285.0	192.2	477 ± 55	0.5 ± 0.2
112473	14h5m46.4s	AAE	4591.5	316.1	810 ± 109	0.3 ± 0.2
120173	16h51m14.0s	AAE	1383.3	228.5	441 ± 59	0.5 ± 0.2
021874	9h59m45.7s	AAE	1704.1	217.7	453 ± 65	0.5 ± 0.1
031774	7h31m25.2s	AAE	995.0	298.9	683 ± 53	0.4 ± 0.1
041774	18h27m33.7s	AAE	924.7	10.4	528 ± 45	0.4 ± 0.2
042574	0h3m49.1s	AAE	1310.3	227.8	511 ± 57	0.5 ± 0.1
042674	18h8m16.9s	AAE	912.6	10.6	533 ± 47	0.4 ± 0.1
042974	20h4m39.7s	AAE	2489.4	343.8	721 ± 65	0.3 ± 0.2
063074	13h26m24.7s	AAE	777.0	6.6	563 ± 49	0.4 ± 0.1
090474	6h29m16.4s	AAE	3717.3	319.5	790 ± 112	0.3 ± 0.2
110880	7h54m18.2s	BCAO	3979.2	334.1	604 ± 61	0.5 ± 0.1
111080	0h1m49.4s	BCAO	3954.2	335.8	537 ± 56	0.7 ± 0.5
111780	8h29m51.6s	BCAO	1661.0	144.4	602 ± 41	0.5 ± 0.1
112080	1h38m29.3s	BCAO	2954.6	142.3	600 ± 37	0.4 ± 0.2
120780	17h37m9.7s	BCAO	3920.0	335.3	557 ± 73	0.6 ± 0.1
020181	13h19m59.2s	BCAO	3940.4	336.2	507 ± 57	0.8 ± 0.3
030481	1h58m55.8s	BCAO	1373.8	103.8	565 ± 26	0.5 ± 0.1
032381	22h23m5.4s	BCAO	3091.2	145.9	664 ± 85	0.4 ± 0.3
071981	8h7m49.8s	BCAO	2664.2	159.5	569 ± 84	0.5 ± 0.4
072381	6h21m52.0s	BCAO	301.7	145.4	796 ± 22	0.3 ± 0.1
031282	4h33m56.8s	BCAO	1478.6	129.2	525 ± 40	0.5 ± 0.1
042282	4h24m54.3s	BCAO	1305.5	129.7	618 ± 120	0.5 ± 0.1
051082	12h47m27.9s	BCAO	2002.0	136.3	652 ± 24	0.5 ± 0.2
060582	19h36m2.3s	BCAO	1381.5	126.7	580 ± 59	0.6 ± 0.1
070382	23h21m1.2s	BCAO	1467.5	127.8	638 ± 55	0.4 ± 0.1
070482	2h22m1.4s	BCAO	1467.3	128.0	644 ± 50	0.4 ± 0.1
072282	9h22m57.9s	BCAO	1349.3	113.5	520 ± 45	0.6 ± 0.1
072482	3h51m41.6s	BCAO	1333.1	105.1	599 ± 51	0.6 ± 0.1
080382	12h19m9.2s	BCAO	1776.8	134.8	611 ± 49	0.6 ± 0.3
080482	1h42m15.3s	BCAO	3093.5	144.5	574 ± 16	0.5 ± 0.3
080682	21h43m23.7s	BCAO	2381.8	159.9	514 ± 48	0.5 ± 0.3
082082	12h57m33.3s	BACO	2599.4	34.1	653 ± 62	0.5 ± 0.2
082182	5h46m1.6s	BCAO	2392.3	160.0	675 ± 97	0.5 ± 0.2

Table 2. (continued)

Event Date	Origin Time *	Recording Station	Epicentral Distance(km)	Back Azimuth *	Q_0	η
092582	21h51m27.6s	BCAO	1776.8	132.2	665 \pm 12	0.6 \pm 0.1
110882	18h29m47.7s	BCAO	1770.9	153.9	513 \pm 23	0.3 \pm 0.2
111882	8h43m19.1s	BCAO	1474.6	125.8	574 \pm 19	0.5 \pm 0.2
120482	18h3m45.4s	BCAO	1991.2	134.0	758 \pm 73	0.6 \pm 0.2
120782	9h36m3.3s	BCAO	1807.3	134.2	654 \pm 20	0.7 \pm 0.3
122282	0h44m50.0s	BCAO	1089.9	117.9	657 \pm 38	0.5 \pm 0.1
122782	2h43m9.1s	BCAO	2162.3	121.6	570 \pm 35	0.6 \pm 0.1
011583	16h34m7.3s	BCAO	1366.0	108.2	527 \pm 59	0.6 \pm 0.2
011783	4h18m16.6s	BCAO	3092.5	145.4	698 \pm 71	0.6 \pm 0.2
020383	13h46m2.3s	BCAO	3299.8	30.40	811 \pm 97	0.2 \pm 0.4
022683	19h49m19.1s	BCAO	2121.1	115.5	651 \pm 44	0.4 \pm 0.1
110283	2h35m12.3s	BCAO	2088.5	112.8	593 \pm 75	0.6 \pm 0.2
011184	18h40m29.6s	BCAO	1568.9	138.6	768 \pm 78	0.5 \pm 0.5
011484	13h36m10.3s	BCAO	1686.2	139.8	413 \pm 19	0.6 \pm 0.3
083084	10h26m49.4s	BCAO	1694.5	141.3	599 \pm 57	0.5 \pm 0.2
101484	20h41m17.9s	BCAO	1277.2	148.2	396 \pm 42	0.4 \pm 0.2
103084	15h24m7.5s	BCAO	1162.8	132.8	530 \pm 33	0.6 \pm 0.1
111784	11h42m45.1s	BCAO	1668.7	141.2	614 \pm 39	0.4 \pm 0.3
022385	14h45m35.9s	BCAO	1864.7	132.4	646 \pm 156	0.5 \pm 0.5
022385	16h55m47.2s	BCAO	3063.7	30.3	797 \pm 32	0.2 \pm 0.1
052385	6h1m32.3s	BCAO	1699.5	127.6	587 \pm 57	0.6 \pm 0.4
062185	20h41m4.1s	BCAO	1673.1	141.4	401 \pm 26	0.7 \pm 0.3
062385	22h46m19.8s	BCAO	1381.9	123.3	544 \pm 42	0.6 \pm 0.2
090385	9h49m22.9s	BCAO	1323.5	116.5	430 \pm 21	0.5 \pm 0.2
011373	6h5m42.4s	BUL	369.7	355.9	641 \pm 53	0.4 \pm 0.1
011473	13h36m59.8s	BUL	1480.1	7.3	454 \pm 50	0.5 \pm 0.1
030973	13h1m46.5s	BUL	882.7	190.0	628 \pm 49	0.4 \pm 0.1
031173	10h40m6.2s	BUL	400.6	350.6	681 \pm 65	0.3 \pm 0.2
040873	0h28m18.7s	BUL	1344.6	17.1	573 \pm 55	0.5 \pm 0.1
041573	13h13m33.4s	BUL	1443.6	7.4	560 \pm 66	0.5 \pm 0.1
041973	2h12m12.7s	BUL	376.5	352.7	672 \pm 57	0.5 \pm 0.2
050373	2h27m13.0s	BUL	1367.1	19.6	545 \pm 60	0.4 \pm 0.1
050773	18h1m2.2s	BUL	412.8	348.9	694 \pm 68	0.3 \pm 0.2
051473	15h22m41.2s	BUL	507.8	88.6	660 \pm 46	0.3 \pm 0.1
051473	20h16m26.8s	BUL	1537.5	6.0	506 \pm 63	0.4 \pm 0.2
052773	9h26m0.7s	BUL	1239.2	30.3	533 \pm 48	0.4 \pm 0.1
053173	4h19m35.8s	BUL	1374.4	19.1	561 \pm 54	0.5 \pm 0.2
070773	16h4m9.9s	BUL	2027.8	22.6	509 \pm 79	0.5 \pm 0.2
071673	18h8m20.0s	BUL	1223.9	30.5	598 \pm 39	0.4 \pm 0.1
072573	16h59m39.2s	BUL	1011.6	44.3	528 \pm 60	0.5 \pm 0.2
090173	11h23m54.6s	BUL	894.3	327.0	759 \pm 69	0.3 \pm 0.1
090773	23h27m50.9s	BUL	531.2	105.8	705 \pm 64	0.3 \pm 0.1
092173	11h12m48.8s	BUL	1606.6	36.0	563 \pm 78	0.3 \pm 0.2
121473	15h4m10.5s	BUL	1707.5	358.4	652 \pm 53	0.3 \pm 0.2
020474	1h29m48.8s	BUL	388.4	353.9	714 \pm 49	0.3 \pm 0.1
021074	16h29m26.4s	BUL	1994.9	342.7	747 \pm 48	0.3 \pm 0.2
032174	12h17m37.0s	BUL	686.4	189.8	643 \pm 39	0.4 \pm 0.1
042474	18h59m53.0s	BUL	747.3	343.1	661 \pm 45	0.4 \pm 0.1
051474	6h51m15.4s	BUL	687.3	189.0	617 \pm 43	0.4 \pm 0.1

Table 2. (continued)

Event Date	Origin Time †	Recording Station	Epicentral Distance(km)	Back Azimuth °	Q_0	η
062474	15h12m57.8s	BUL	691.6	191.3	649 ± 52	0.3 ± 0.1
062574	15h27m32.7s	BUL	687.1	191.6	623 ± 55	0.4 ± 0.2
072374	14h9m56.0s	BUL	733.9	192.7	581 ± 63	0.3 ± 0.2
091774	14h30m54.9s	BUL	1387.8	16.1	527 ± 67	0.5 ± 0.2
100474	17h4m52.6	BUL	1122.3	33.0	633 ± 29	0.3 ± 0.1
101174	12h3m43.7s	BUL	1269.0	200.5	544 ± 56	0.4 ± 0.2
011373	6h5m42.4s	GRM	1386.3	16.5	379 ± 31	0.5 ± 0.1
030973	13h1m46.5s	GRM	592.0	4.6	346 ± 33	0.5 ± 0.1
052473	7h15m3.5s	GRM	2646.4	17.8	369 ± 41	0.5 ± 0.2
030973*	13h1m46.5s	GRM	735.9	5.9	381 ± 40	0.5 ± 0.1
022765	11h30m0.0s	HLW	2672.0	262.4	842 ± 63	0.2 ± 0.1
030573	23h59m46.6s	HLW	336.0	135.2	659 ± 44	0.4 ± 0.1
022574	16h5m15.7s	HLW	2395.2	155.8	667 ± 71	0.3 ± 0.1
031774	7h31m25.2s	HLW	1834.6	181.6	784 ± 72	0.3 ± 0.1
042574	0h3m49.1s	HLW	3193.8	182.4	662 ± 58	0.4 ± 0.1
063074	13h26m24.7s	HLW	1755.5	149.0	382 ± 25	0.6 ± 0.1
092374	19h28m17.2s	HLW	3857.1	213.5	780 ± 72	0.3 ± 0.1
020873	16h14m38.5s	ICA**	3400.0	78.5	646 ± 51	0.6 ± 0.2
060773	7h21m21.5s	ICA**	3015.9	42.7	757 ± 56	0.6 ± 0.1
120973	7h12m52.4s	ICA**	3859.7	56.4	746 ± 66	0.5 ± 0.1
121178	8h56m36.7s	ICA**	3017.2	9.5	804 ± 42	0.6 ± 0.1
101080	14h44m52.6s	ICA**	3359.9	10.4	608 ± 32	0.8 ± 0.2
101380	6h37m39.2s	ICA**	3365.7	10.8	676 ± 74	0.8 ± 0.2
120380	10h31m20.1s	ICA**	3376.6	10.3	651 ± 45	0.5 ± 0.1
111481	9h5m29.0s	ICA**	4438.8	60.4	768 ± 43	0.6 ± 0.1
091182	21h40m12.2s	ICA**	3379.7	11.2	681 ± 61	0.5 ± 0.1
093083	18h58m14.3s	ICA**	5321.7	79.8	565 ± 61	0.6 ± 0.1
031584	19h0m37.2s	ICA**	3341.4	21.9	701 ± 66	0.5 ± 0.1
070284	1h46m58.9s	ICA**	4683.8	59.2	662 ± 67	0.6 ± 0.1
010773	12h17m12.6s	NAI	722.3	0.4	455 ± 49	0.5 ± 0.2
011473	13h36m59.8s	NAI	948.4	229.3	436 ± 35	0.5 ± 0.1
031173	10h40m6.2s	NAI	1945.5	209.2	499 ± 40	0.4 ± 0.1
040573	2h56m48.0s	NAI	1940.9	209.1	507 ± 37	0.5 ± 0.2
040773	19h17m38.7s	NAI	1584.0	24.5	421 ± 50	0.5 ± 0.1
040873	0h28m18.7s	NAI	946.4	212.5	409 ± 55	0.5 ± 0.1
041373	14h13m56.9s	NAI	1651.4	27.7	440 ± 50	0.5 ± 0.1
041573	13h13m33.4s	NAI	974.5	227.8	419 ± 45	0.5 ± 0.1
041973	2h12m12.7s	NAI	1955.7	208.4	460 ± 40	0.5 ± 0.1
042273	22h3m43.5s	NAI	848.4	312.5	403 ± 35	0.5 ± 0.1
050373	2h27m13.5s	NAI	910.6	209.3	428 ± 29	0.5 ± 0.2
051473	15h22m41.2s	NAI	2097.1	189.7	457 ± 46	0.5 ± 0.1
051473	20h16m26.8s	NAI	932.8	233.3	449 ± 31	0.5 ± 0.1
052473	7h15m8.5s	NAI	1056.4	198.4	435 ± 59	0.5 ± 0.2
070773	16h4m9.9s	NAI	245.8	214.8	431 ± 48	0.5 ± 0.1
071873	19h39m13.0s	NAI	-1126.0	133.3	420 ± 48	0.5 ± 0.2
090173	11h23m54.6s	NAI	1927.7	225.8	497 ± 51	0.5 ± 0.1
092173	11h12m48.8s	NAI	767.4	177.2	430 ± 51	0.4 ± 0.2
120173	16h51m14.0s	NAI	837.4	284.6	395 ± 34	0.5 ± 0.1
121473	15h4m10.5s	NAI	1028.4	248.2	441 ± 57	0.5 ± 0.2

Table 2. (continued)

Event Date	Origin Time *	Recording Station	Epicentral Distance(km)	Back Azimuth *	Q_0	η
121973	3h6m58.8s	NAI	3044.6	199.7	557 ± 60	0.4 ± 0.2
012174	15h15m54.0s	NAI	2896.2	198.0	513 ± 47	0.5 ± 0.1
020174	15h49m29.2s	NAI	2178.9	212.0	558 ± 39	0.4 ± 0.1
020474	13h16m55.3s	NAI	1957.0	208.8	442 ± 51	0.5 ± 0.1
021074	16h29m26.4s	NAI	1506.2	263.1	471 ± 44	0.5 ± 0.2
021374	9h59m45.7s	NAI	841.5	254.9	460 ± 39	0.5 ± 0.1
022574	16h5m15.7s	NAI	1278.9	16.2	443 ± 37	0.5 ± 0.2
031774	7h31m25.2s	NAI	1740.8	337.7	478 ± 45	0.4 ± 0.2
062474	15h12m57.8s	NAI	2945.5	199.5	573 ± 47	0.4 ± 0.1
072374	14h9m56.0s	NAI	2990.1	199.7	581 ± 40	0.4 ± 0.1
011373	6h5m42.4s	PRE	989.9	1.1	779 ± 67	0.3 ± 0.2
011473	13h36m59.8s	PRE	2101.7	6.5	612 ± 79	0.4 ± 0.2
022073	15h19m51.7s	PRE	1005.4	358.5	685 ± 68	0.4 ± 0.2
031173	10h40m6.2s	PRE	1016.4	358.9	651 ± 79	0.4 ± 0.2
040573	2h56m48.0s	PRE	1019.0	359.1	742 ± 74	0.3 ± 0.1
041573	13h13m33.4s	PRE	2065.2	6.5	673 ± 43	0.4 ± 0.2
041973	2h12m12.7s	PRE	994.4	359.8	782 ± 58	0.3 ± 0.1
050073	18h1m2.2s	PRE	1973.3	15.0	639 ± 49	0.5 ± 0.1
050873	5h22m22.9s	PRE	983.5	358.2	772 ± 67	0.3 ± 0.1
051473	15h22m41.2s	PRE	838.4	41.2	681 ± 45	0.4 ± 0.1
051473	20h16m26.8s	PRE	2159.6	5.6	623 ± 49	0.5 ± 0.1
052473	7h15m8.5s	PRE	1802.3	20.0	569 ± 55	0.4 ± 0.1
052773	9h26m0.7s	PRE	1817.9	21.8	608 ± 47	0.5 ± 0.1
053173	4h19m35.8s	PRE	1981.6	14.7	645 ± 57	0.5 ± 0.1
071673	18h8m20.0s	PRE	1801.3	21.9	635 ± 48	0.4 ± 0.1
071873	19h39m13.0s	PRE	1739.7	23.4	611 ± 57	0.4 ± 0.1
082873	22h43m16.7s	PRE	1912.9	9.8	623 ± 56	0.4 ± 0.2
090173	11h23m54.6s	PRE	1440.9	342.1	761 ± 53	0.3 ± 0.1
090773	23h27m50.9s	PRE	730.1	49.5	632 ± 39	0.4 ± 0.1
110373	21h35m44.4s	PRE	719.3	45.9	713 ± 51	0.4 ± 0.1
020174	15h49m29.2s	PRE	898.5	345.3	751 ± 71	0.3 ± 0.2
020474	1h29m48.8s	PRE	1007.2	0.2	687 ± 56	0.3 ± 0.2
020474	13h16m55.3s	PRE	998.8	359.3	730 ± 68	0.3 ± 0.2
021074	16h29m26.4s	PRE	2584.5	347.6	761 ± 51	0.3 ± 0.1
040874	6h12m49.2s	PRE	2377.5	21.3	545 ± 62	0.5 ± 0.2
042474	18h59m53.0s	PRE	1347.2	352.6	754 ± 53	0.4 ± 0.1
022765	11h30m0.0s	SDB	4406.6	347.7	590 ± 61	0.5 ± 0.1
040982	2h33m58.7s	SLR	885.0	351.2	650 ± 32	0.4 ± 0.1
062582	18h0m0.8s	SLR	288.4	217.5	475 ± 72	0.6 ± 0.1
070482	2h22m1.4s	SLR	2428.4	1.7	670 ± 75	0.3 ± 0.1
080482	1h42m15.3s	SLR	1087.7	41.6	623 ± 66	0.5 ± 0.1
080682	21h43m23.7s	SLR	1124.3	347.5	625 ± 88	0.4 ± 0.1
081982	14h6m13.1s	SLR	292.0	21.3	505 ± 72	0.5 ± 0.1
120482	18h3m45.4s	SLR	1979.4	10.3	612 ± 70	0.4 ± 0.1
061884	10h50m1.1s	SLR	2021.2	359.0	708 ± 150	0.3 ± 0.1
082584	20h37m49.8s	SLR	1929.6	14.0	600 ± 124	0.4 ± 0.1
022385	14h45m35.9s	SLR	2094.2	8.2	464 ± 48	0.6 ± 0.1
050885	11h35m45.7s	SLR	506.8	218.4	504 ± 42	0.4 ± 0.2
051485	13h24m57.8s	SLR	2175.1	41.9	639 ± 83	0.4 ± 0.2

Table 2. (continued)

Event Date	Origin Time [†]	Recording Station	Epicentral Distance(km)	Back Azimuth [*]	Q_0	η
062885	7h32m19.9s	SLR	2158.2	41.6	623 ± 76	0.6 ± 0.3
011373	6h5m42.4s	WIN	295.0	42.4	715 ± 53	0.3 ± 0.1
011473	13h36m59.8s	WIN	2207.2	40.0	648 ± 96	0.5 ± 0.2
020673	9h50m41.4s	WIN	1171.3	113.3	722 ± 67	0.3 ± 0.1
022073	15h19m51.7s	WIN	1264.8	60.8	750 ± 78	0.3 ± 0.2
030973	13h1m46.5s	WIN	1124.4	124.2	680 ± 59	0.3 ± 0.1
031173	10h40m6.2s	WIN	1275.9	60.5	760 ± 78	0.3 ± 0.1
041573	13h13m33.4s	WIN	2176.3	40.5	600 ± 57	0.5 ± 0.2
041973	2h12m12.7s	WIN	1278.9	61.7	680 ± 53	0.3 ± 0.2
050373	2h27m13.0s	WIN	2249.3	48.4	590 ± 56	0.5 ± 0.1
050873	5h22m22.9s	WIN	1294.4	61.5	730 ± 68	0.3 ± 0.1
051473	15h22m41.4s	WIN	1669.8	83.0	580 ± 40	0.5 ± 0.1
051473	20h16m26.8s	WIN	2239.8	38.5	580 ± 56	0.5 ± 0.1
052473	7h15m8.5s	WIN	2187.9	54.4	550 ± 51	0.5 ± 0.2
052773	7h15m8.5s	WIN	2229.8	55.5	580 ± 49	0.5 ± 0.1
053173	4h19m35.8s	WIN	2250.8	48.1	590 ± 61	0.5 ± 0.2
070773	16h4m9.9s	WIN	2893.6	44.5	510 ± 52	0.6 ± 0.2
071673	18h8m20.0s	WIN	2217.6	55.8	580 ± 48	0.4 ± 0.1
071873	19h39m13.0s	WIN	2187.3	57.7	490 ± 57	0.5 ± 0.1
082873	22h43m16.7s	WIN	2106.2	45.3	590 ± 54	0.5 ± 0.1
090173	11h23m54.6s	WIN	1234.8	35.0	690 ± 63	0.3 ± 0.2
090673	20h13m35.7s	WIN	1097.5	123.9	760 ± 58	0.3 ± 0.1
110373	21h35m44.4s	WIN	1614.4	87.3	570 ± 52	0.5 ± 0.1
121473	15h4m10.5s	WIN	2280.4	31.5	550 ± 56	0.4 ± 0.1
020174	15h49m29.2s	WIN	1023.1	61.1	760 ± 75	0.2 ± 0.2
020474	13h16m55.3s	WIN	1272.6	61.3	690 ± 48	0.3 ± 0.1
021074	16h29m26.4s	WIN	2265.7	16.7	540 ± 52	0.5 ± 0.1
040874	6h12m49.2s	WIN	2715.5	48.8	500 ± 57	0.6 ± 0.2
042674	12h18m24.4s	WIN	1143.9	112.2	720 ± 57	0.2 ± 0.2
062474	15h12m57.8s	WIN	1060.9	114.6	690 ± 61	0.4 ± 0.1
072374	14h9m56.0s	WIN	1050.3	117.0	770 ± 77	0.2 ± 0.1

[†] The origin times for the two explosional events dated 10-20-63 and 02-28-65 were given by Bolt (1976). The origin times for all the other events were given in PRE.

^{*} Q_0 and η listed in this line were estimated from averaging spectral ratios obtained from events 03-09-73, 06-10-73, 08-05-73, 09-06-73, 04-26-74, 05-14-74, 06-24-74.

^{**} ICA denotes the Ivory Coast Array. The averaged spectral ratios collected from all the stations were used to estimate Q_0 and η for each event.

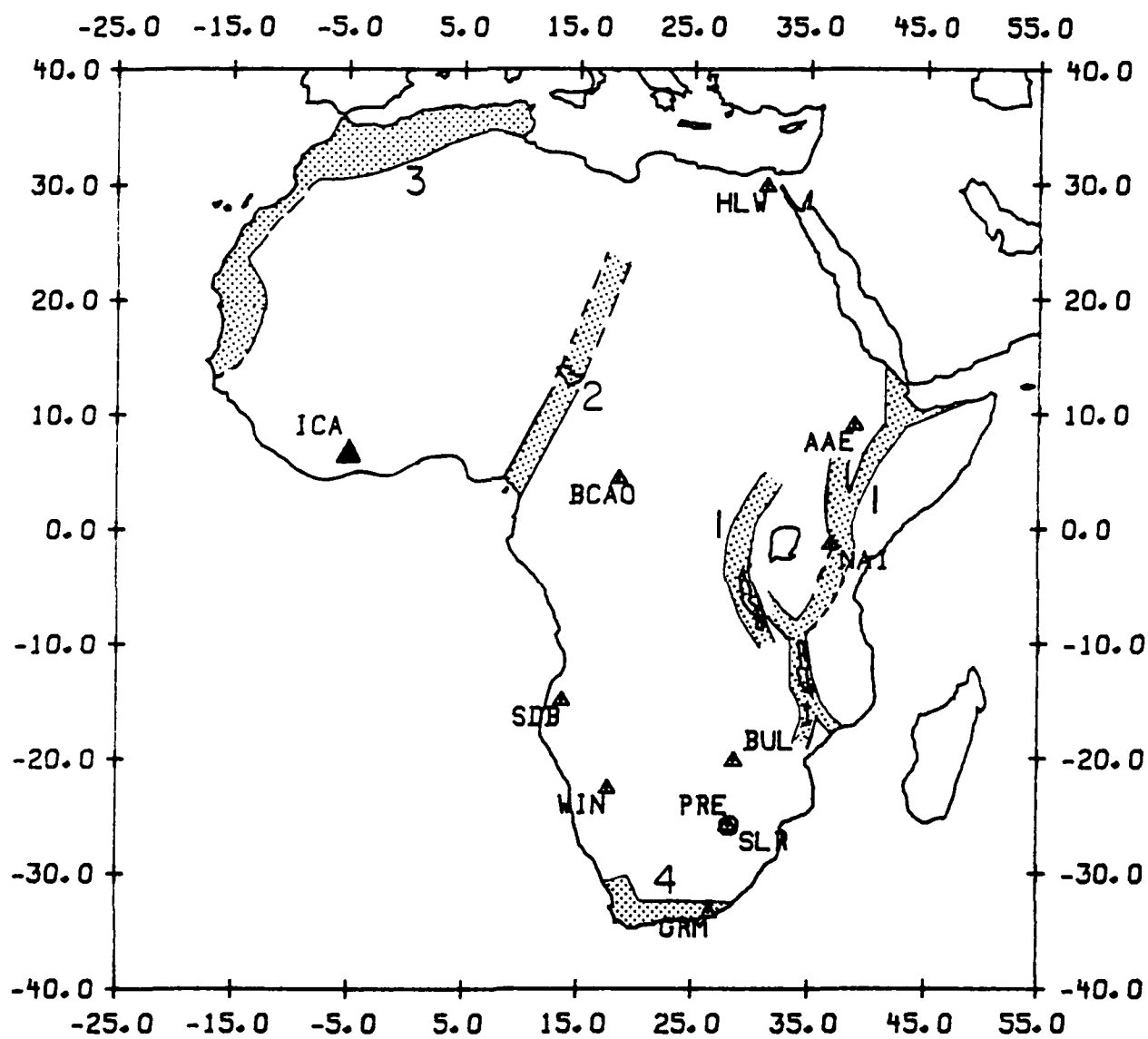


Figure 1

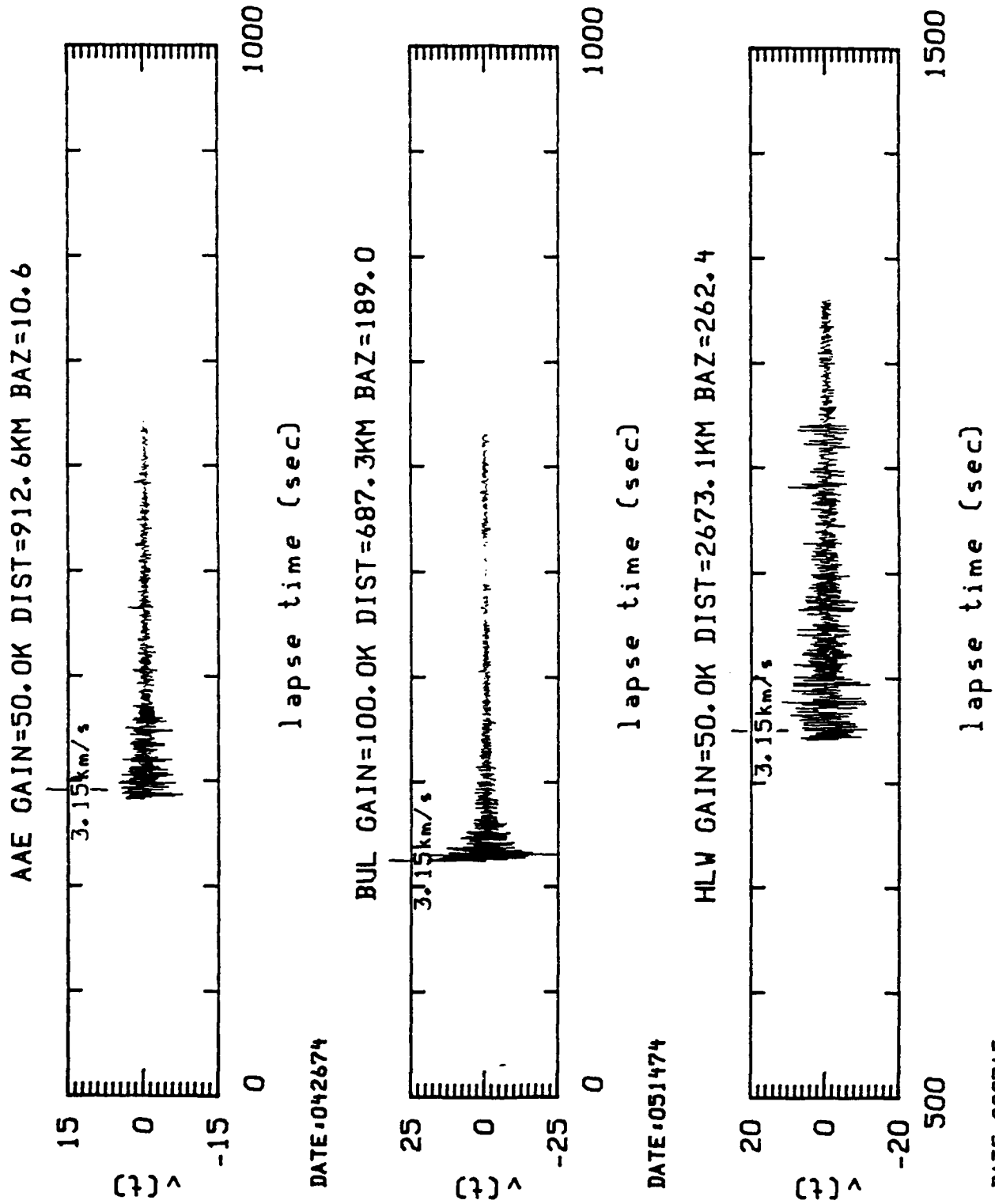


Figure 2

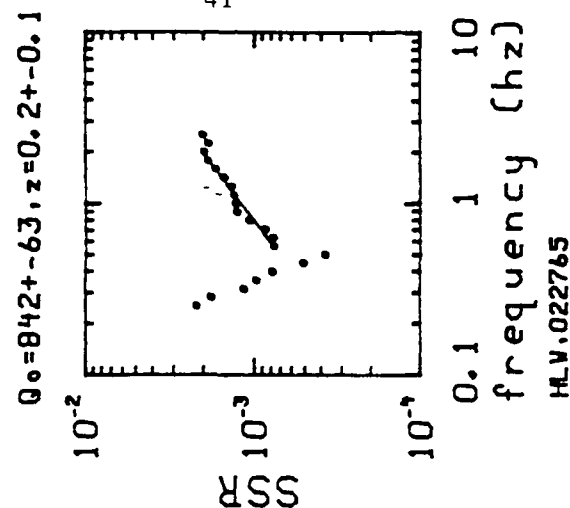
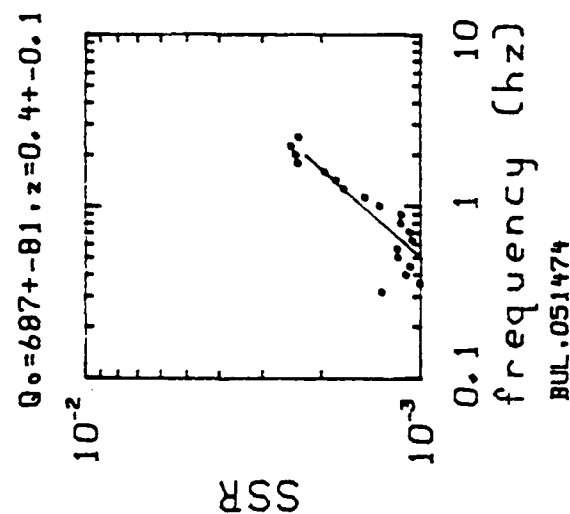
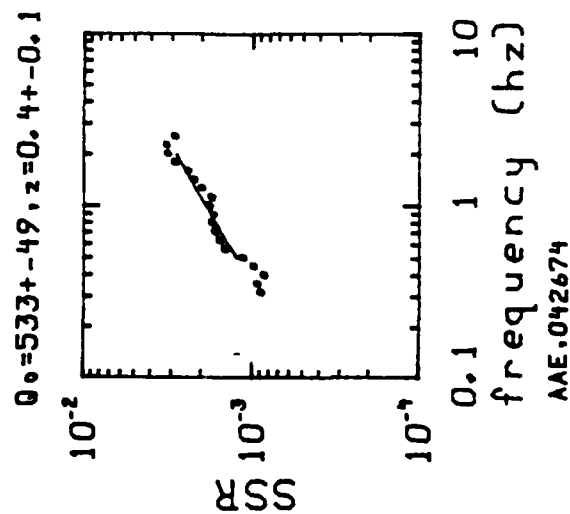
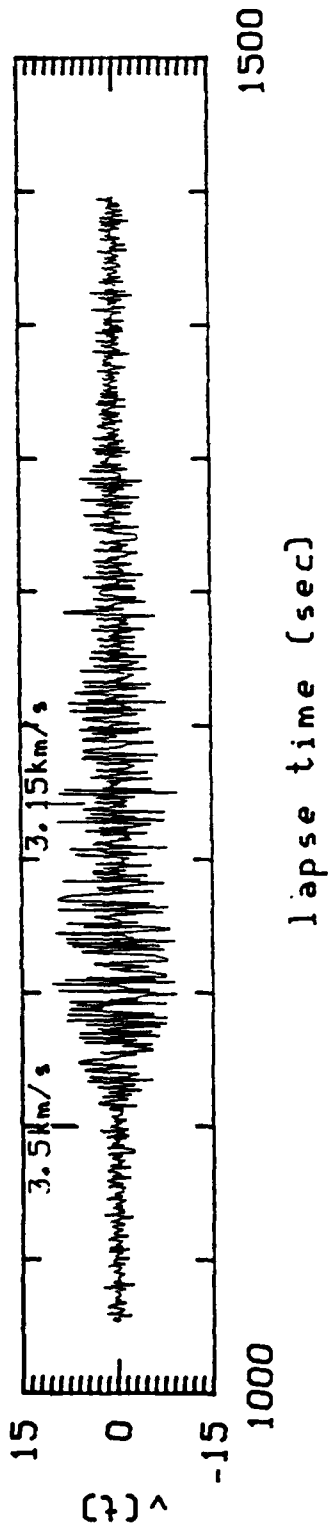


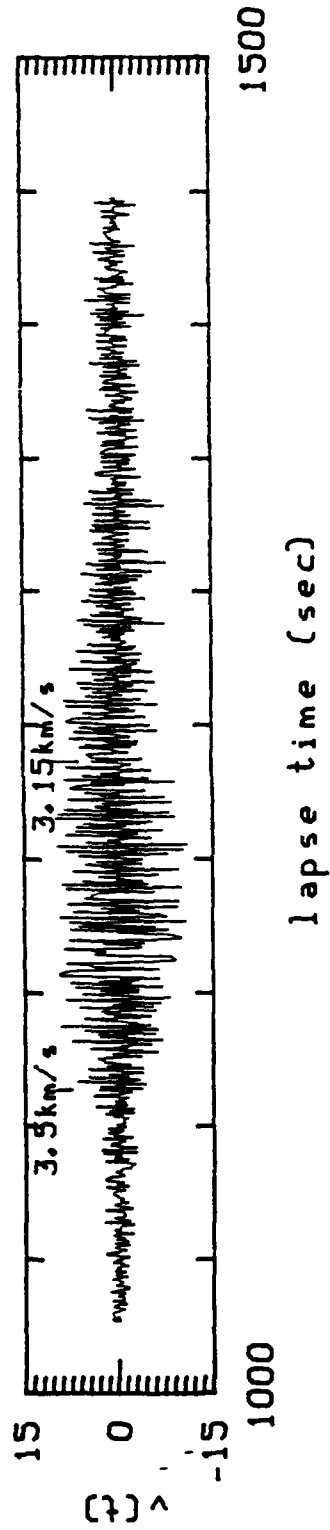
Figure 3

KIC GAIN=500K DIST=3847.3KM BAZ=56.3



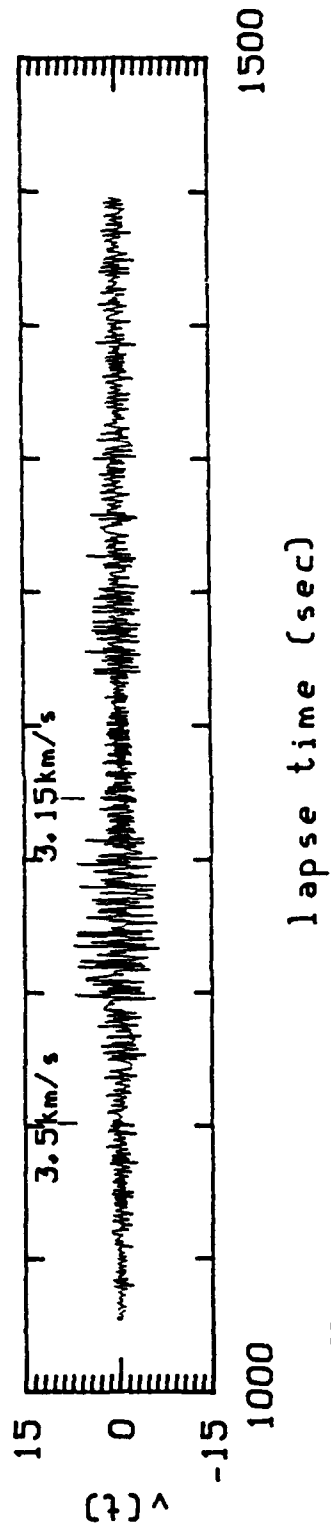
DATE.120978

LIC GAIN=552K DIST=3904.9KM BAZ=56.5



DATE.120978

TIC GAIN=353K DIST=3855.7KM BAZ=56.8



DATE.120978

Figure 4

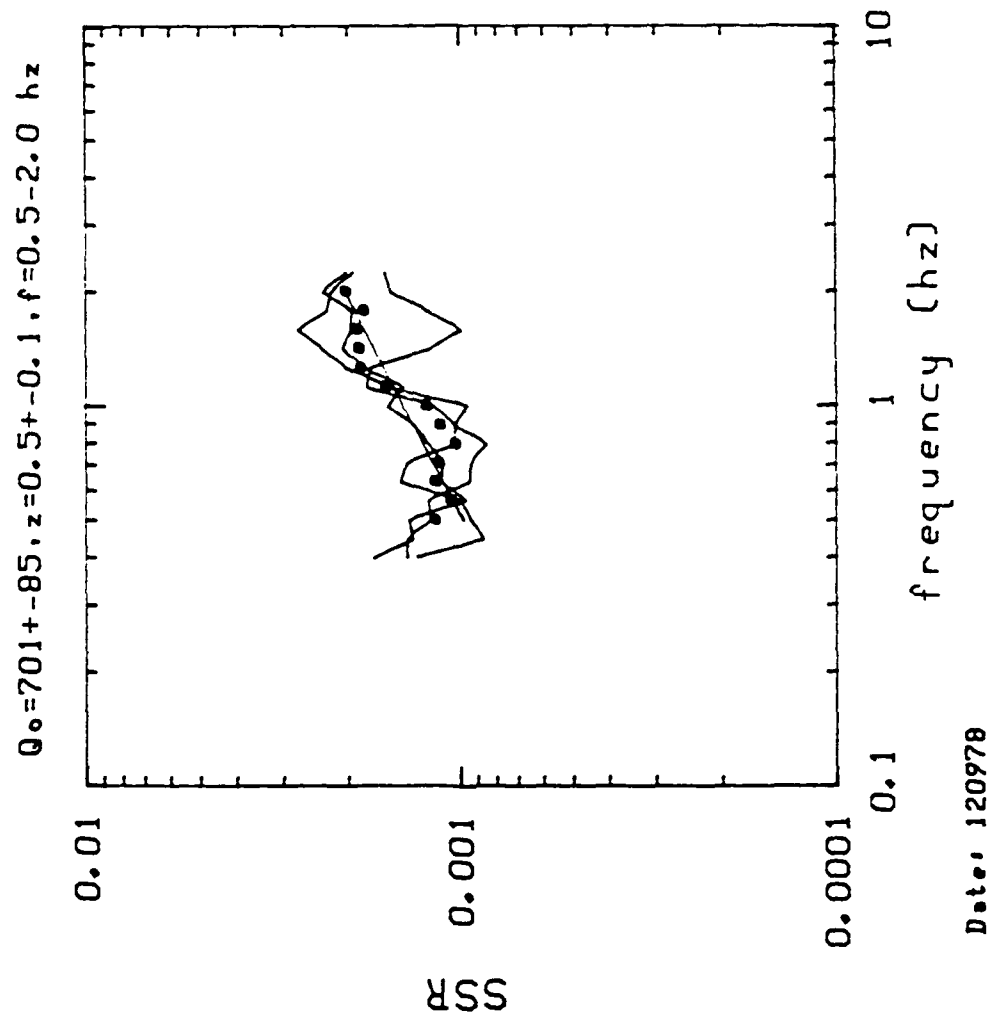


Figure 5

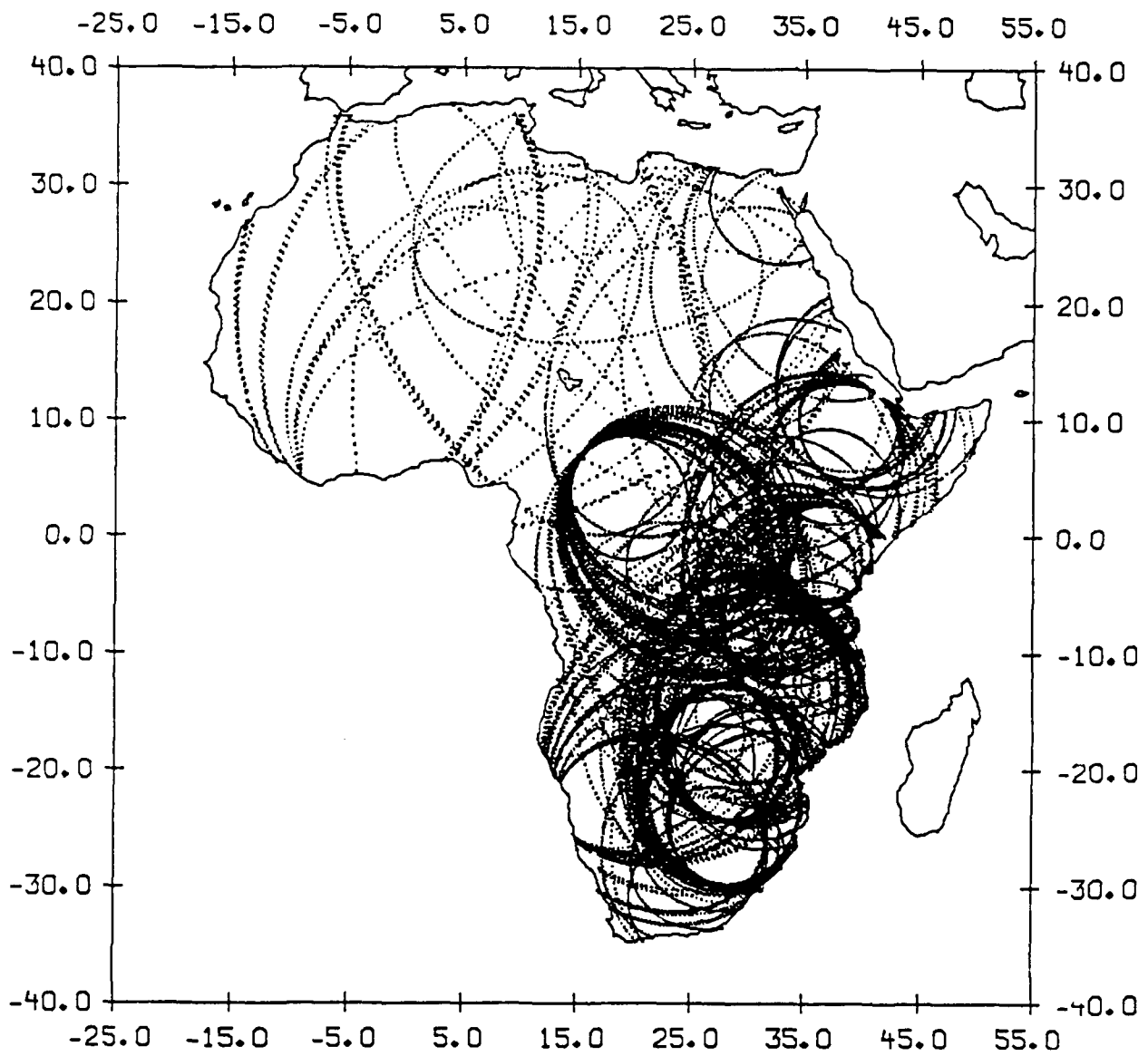


Figure 6

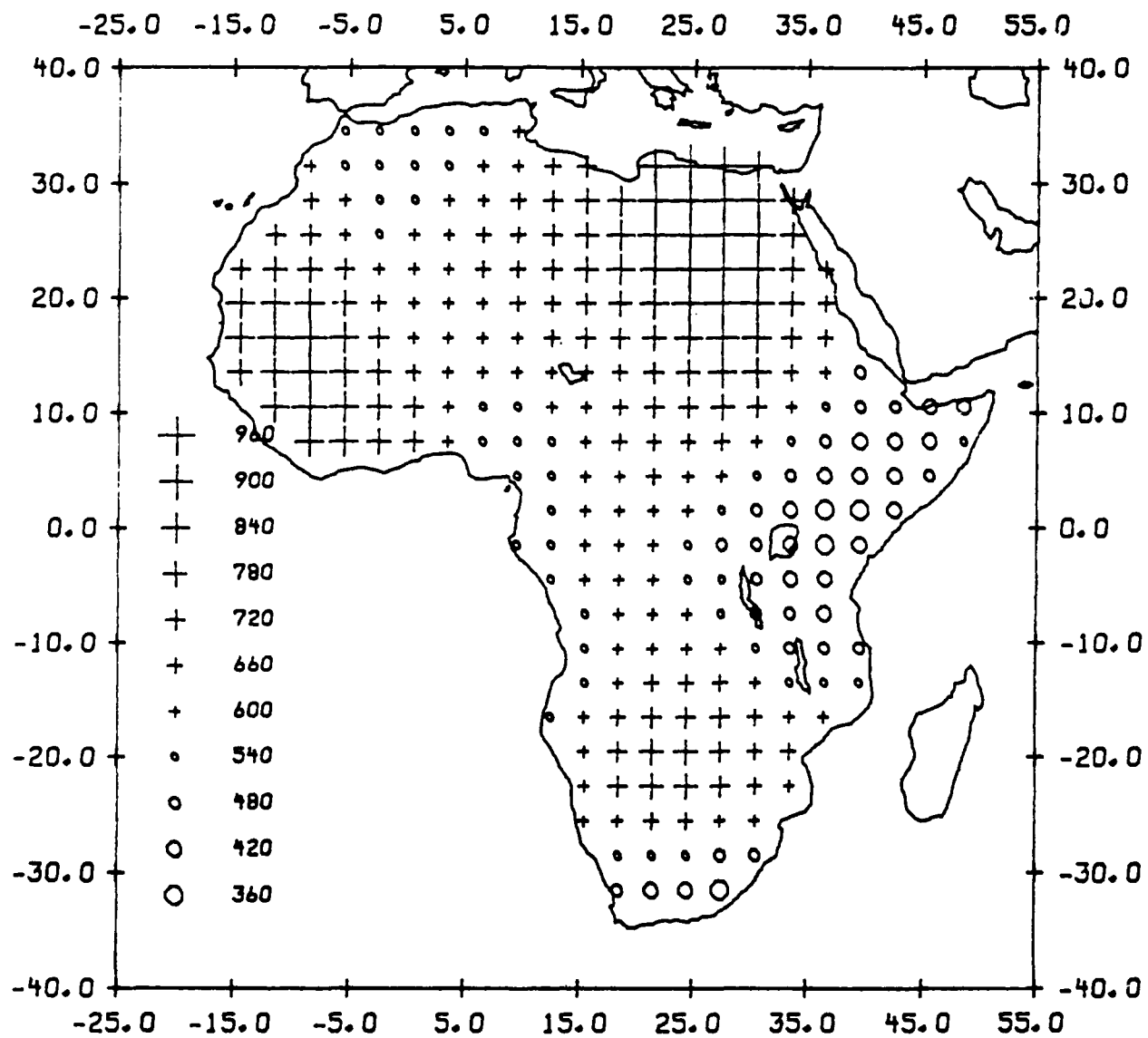


Figure 7

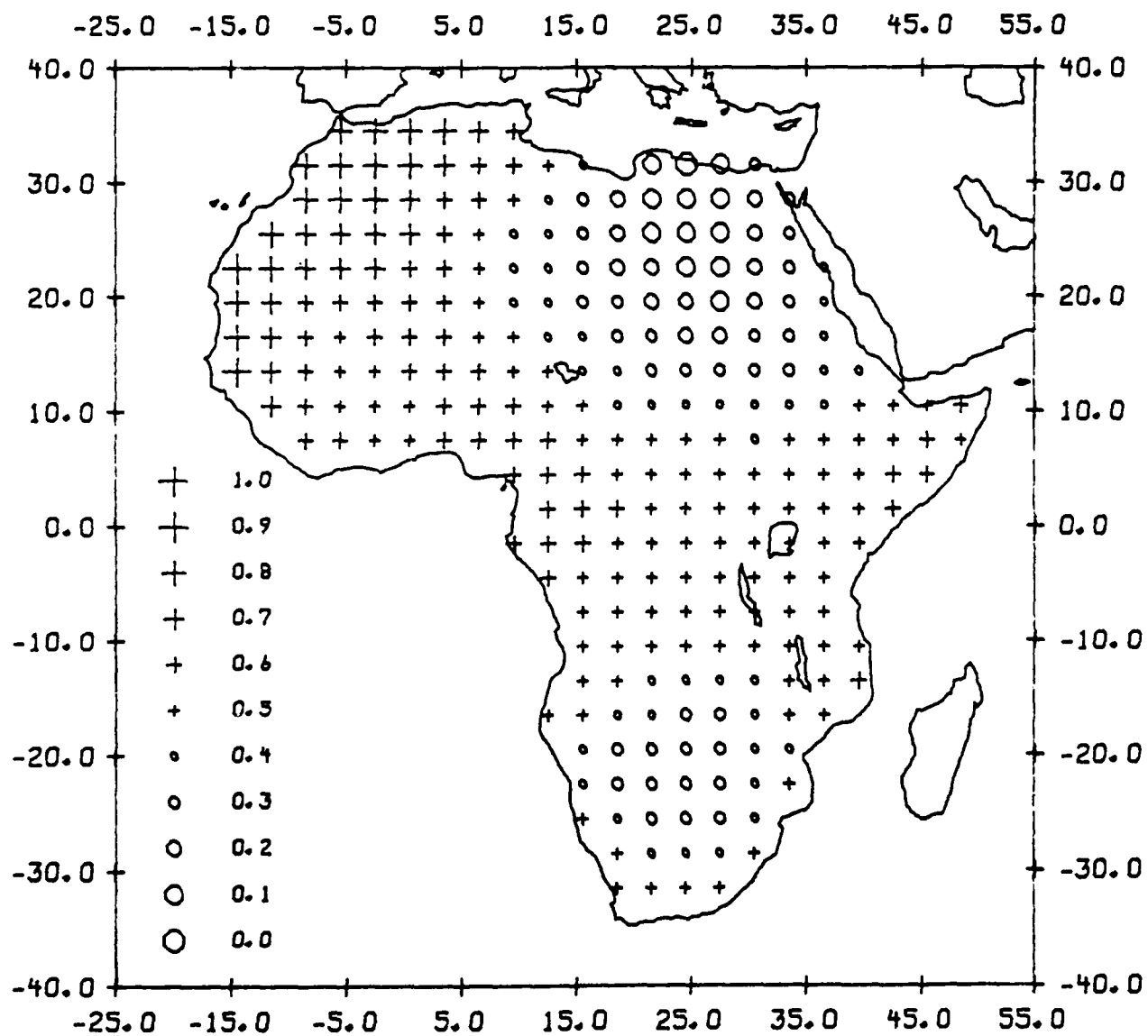


Figure 8

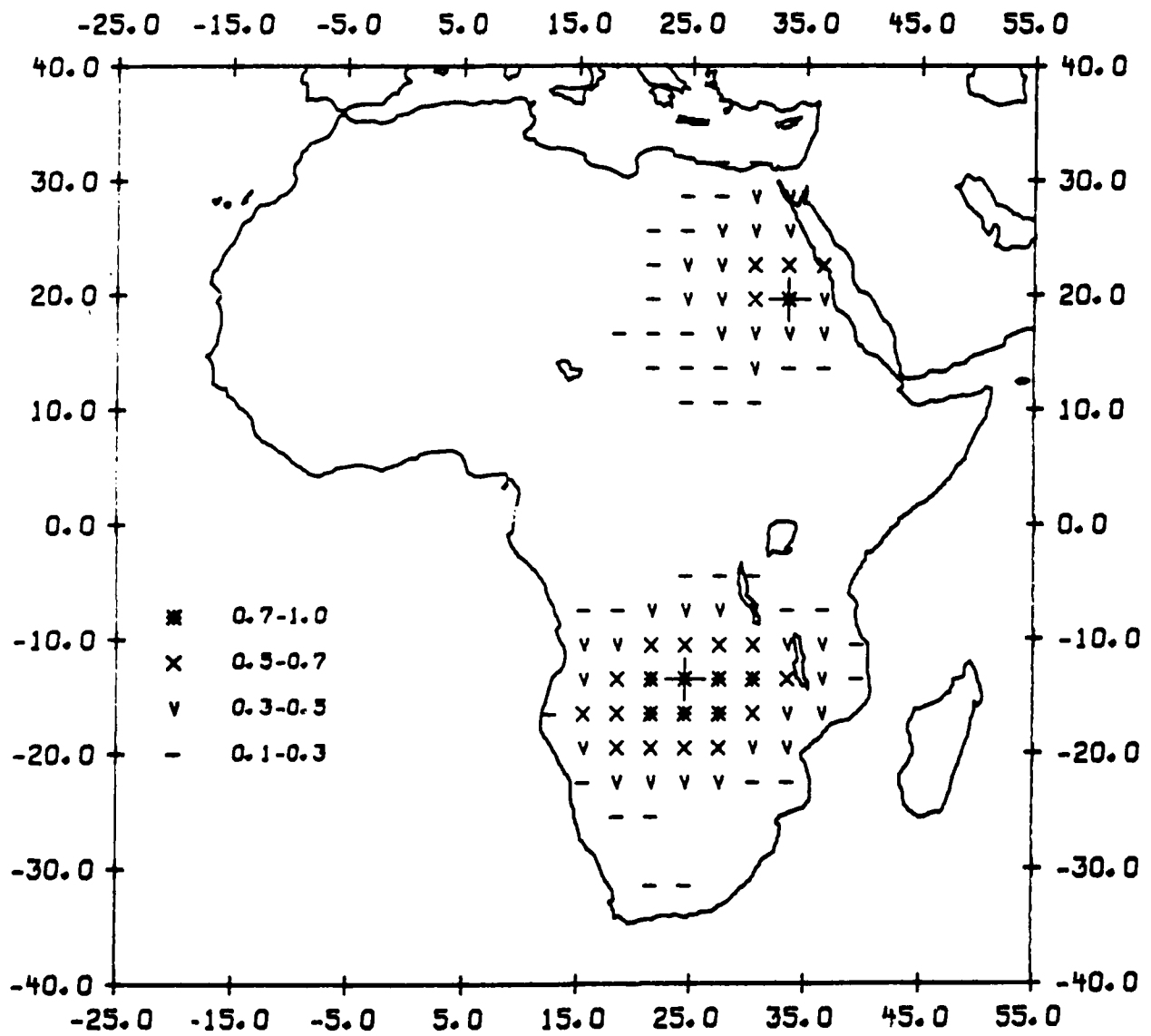


Figure 9a

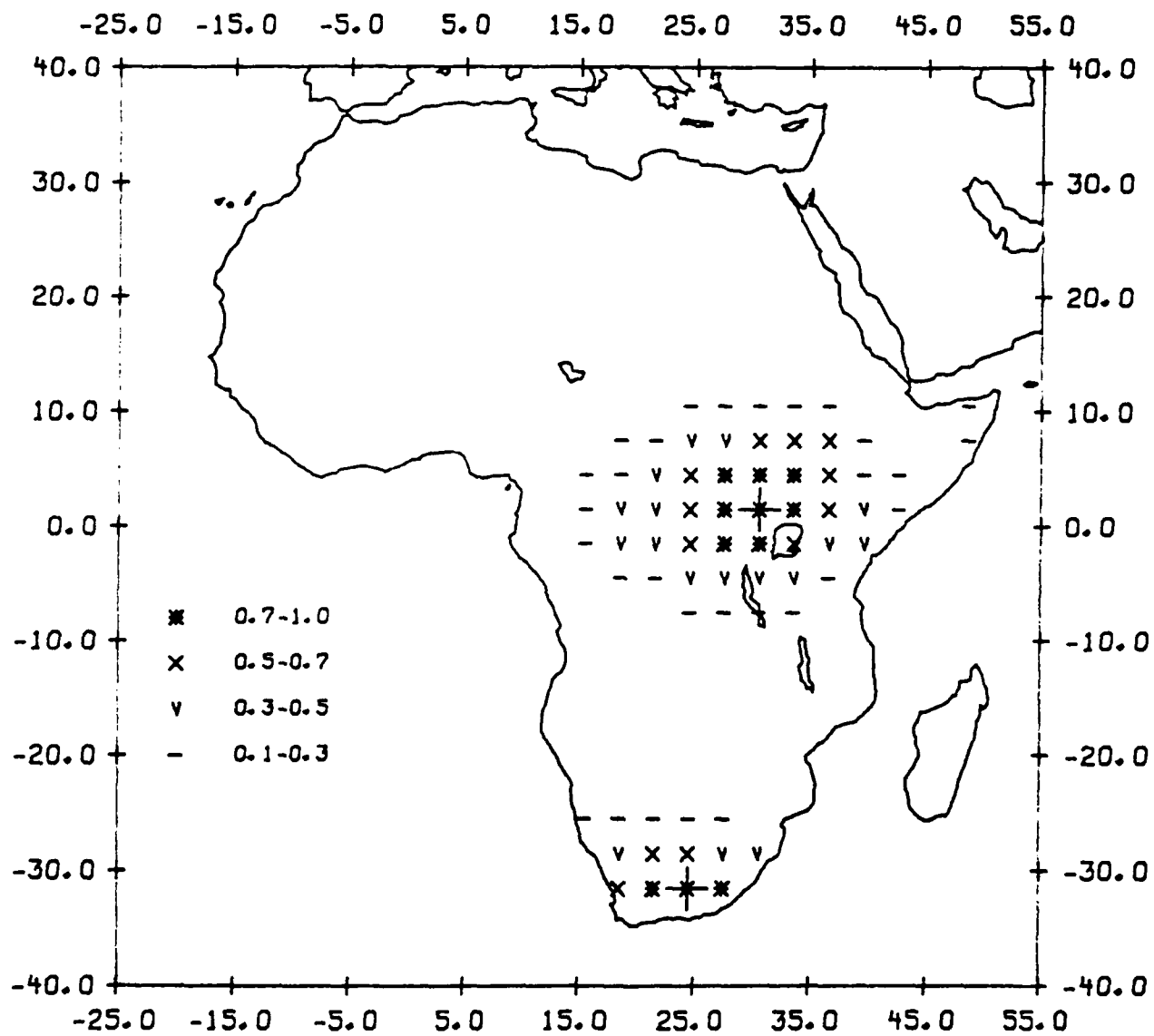


Figure 9b

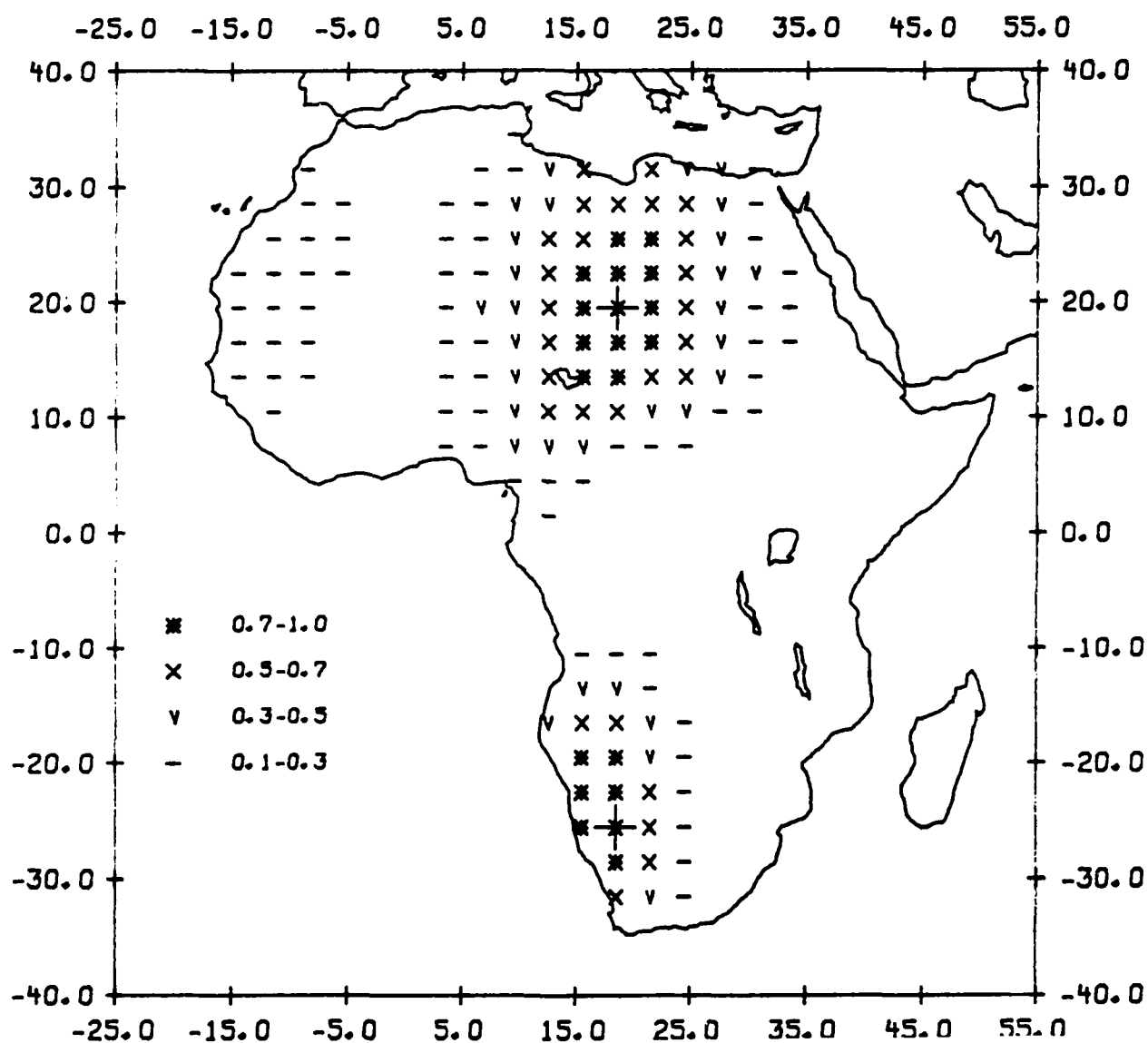


Figure 9c

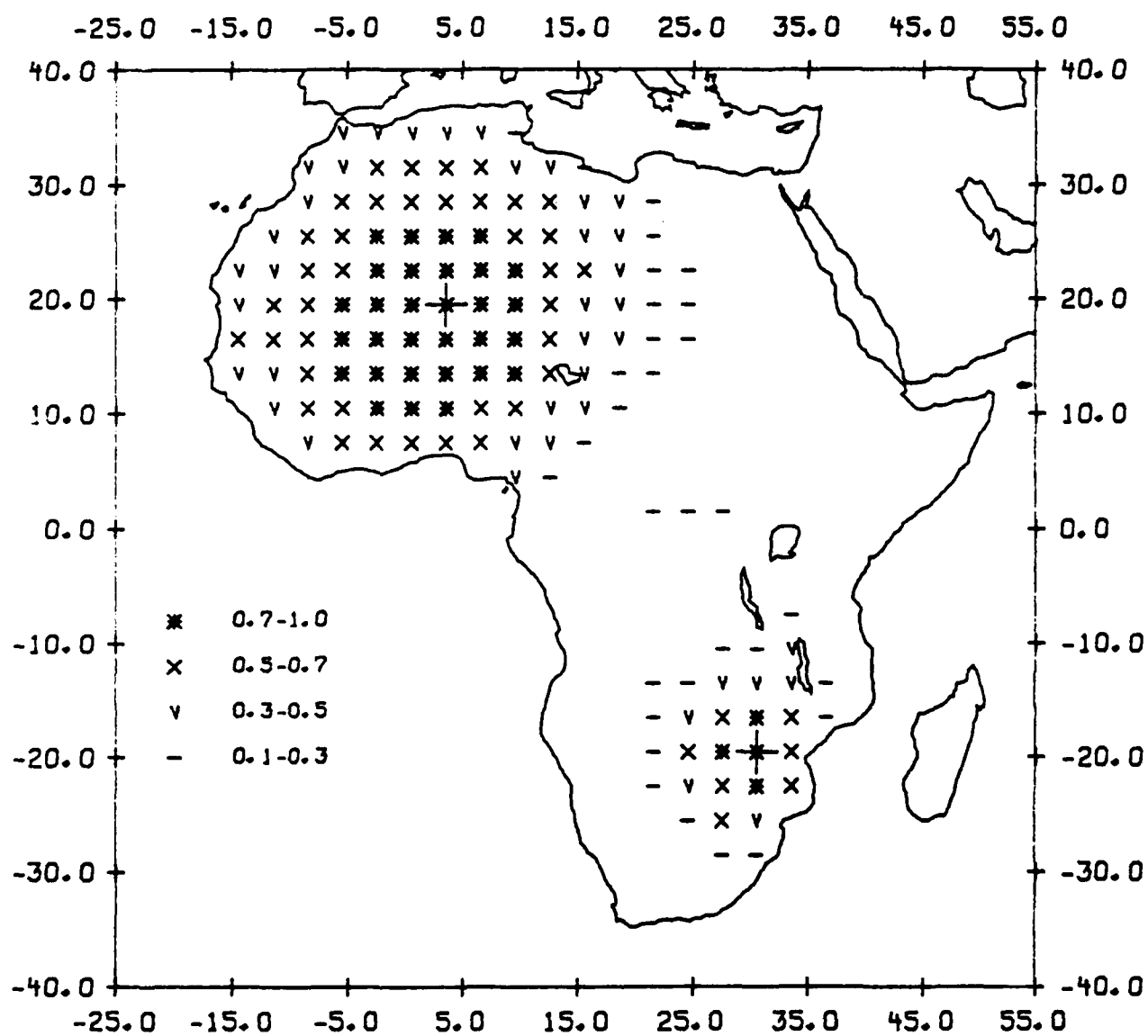


Figure 9d

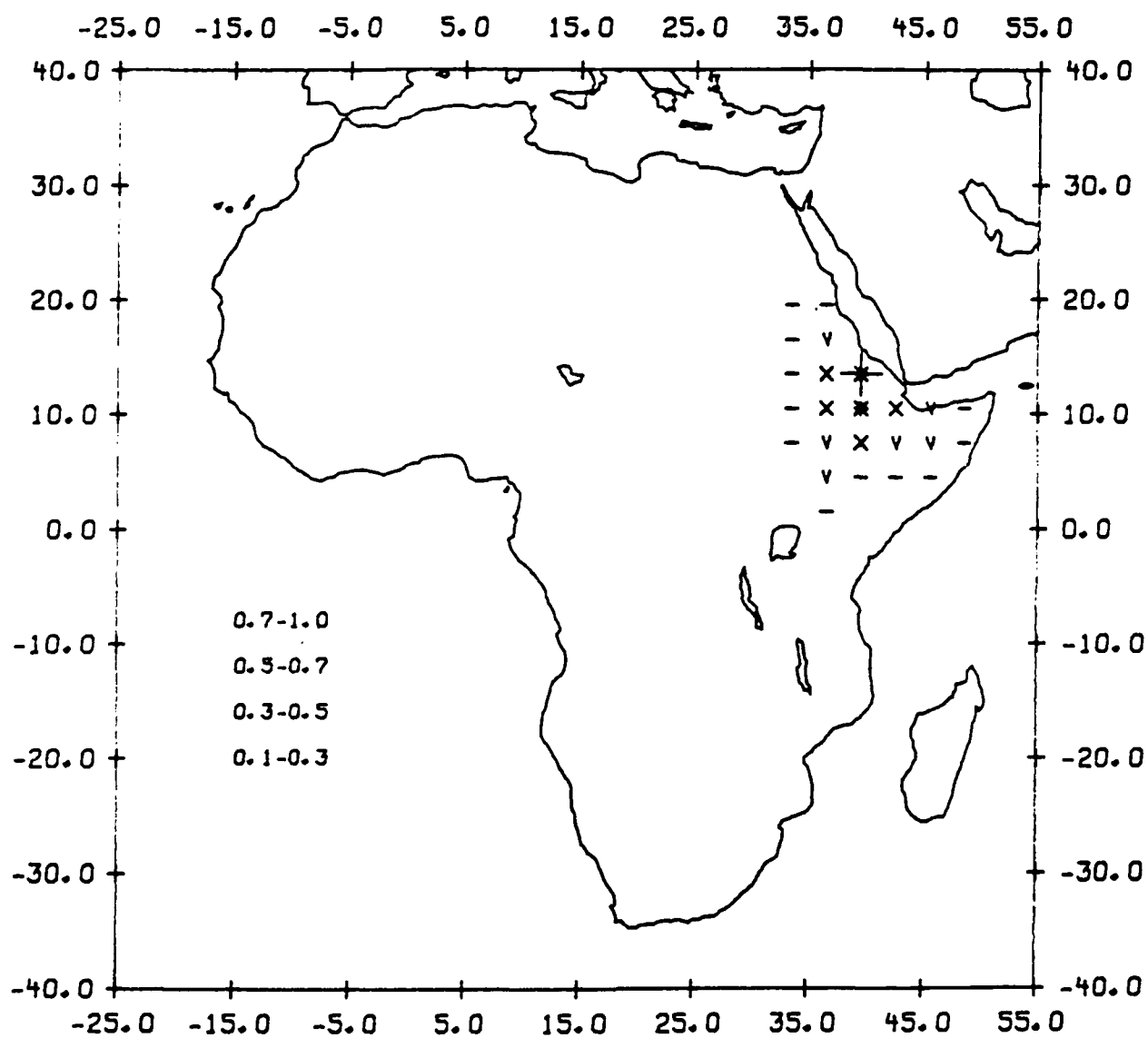


Figure 9e

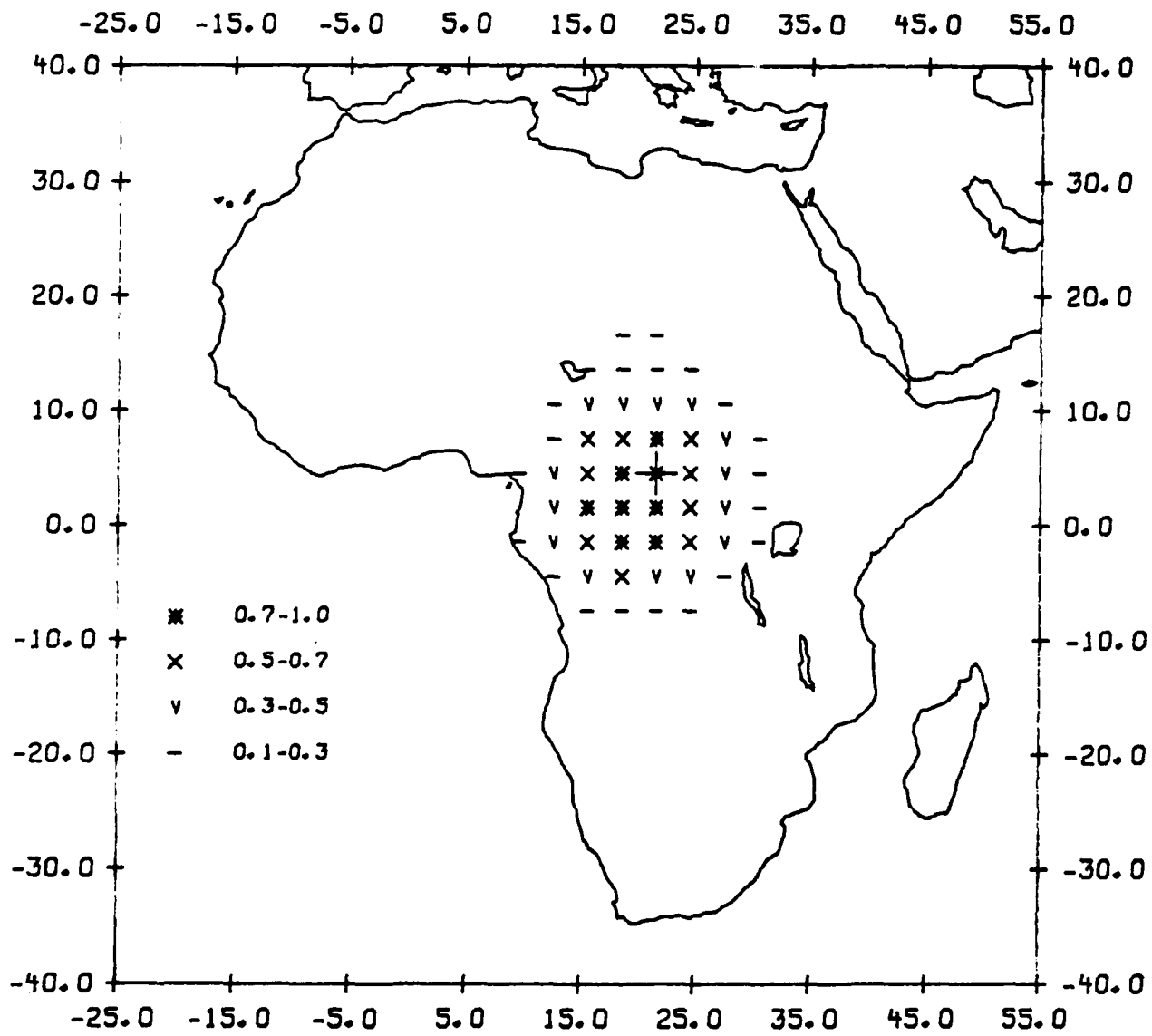


Figure 9f

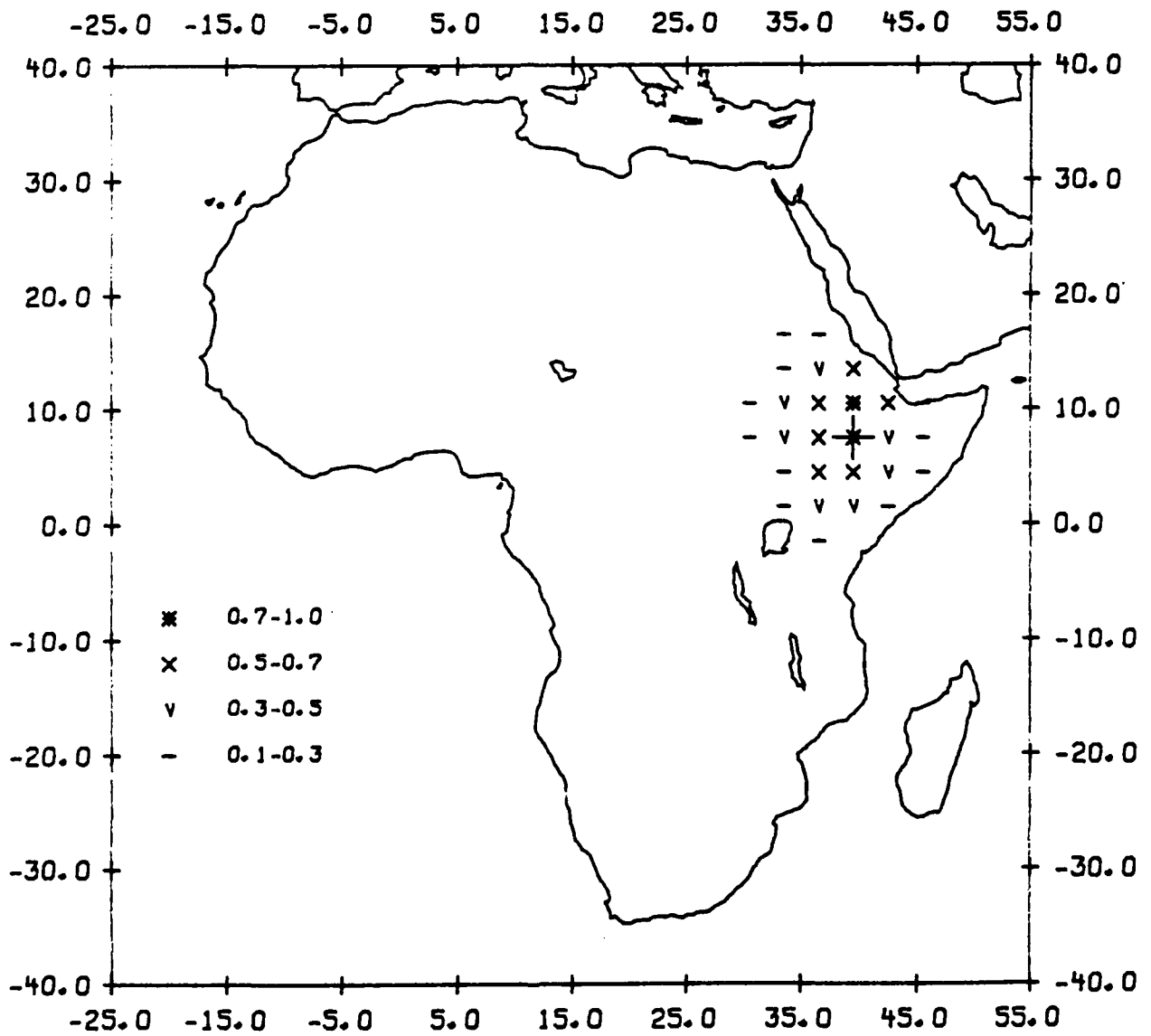


Figure 9g

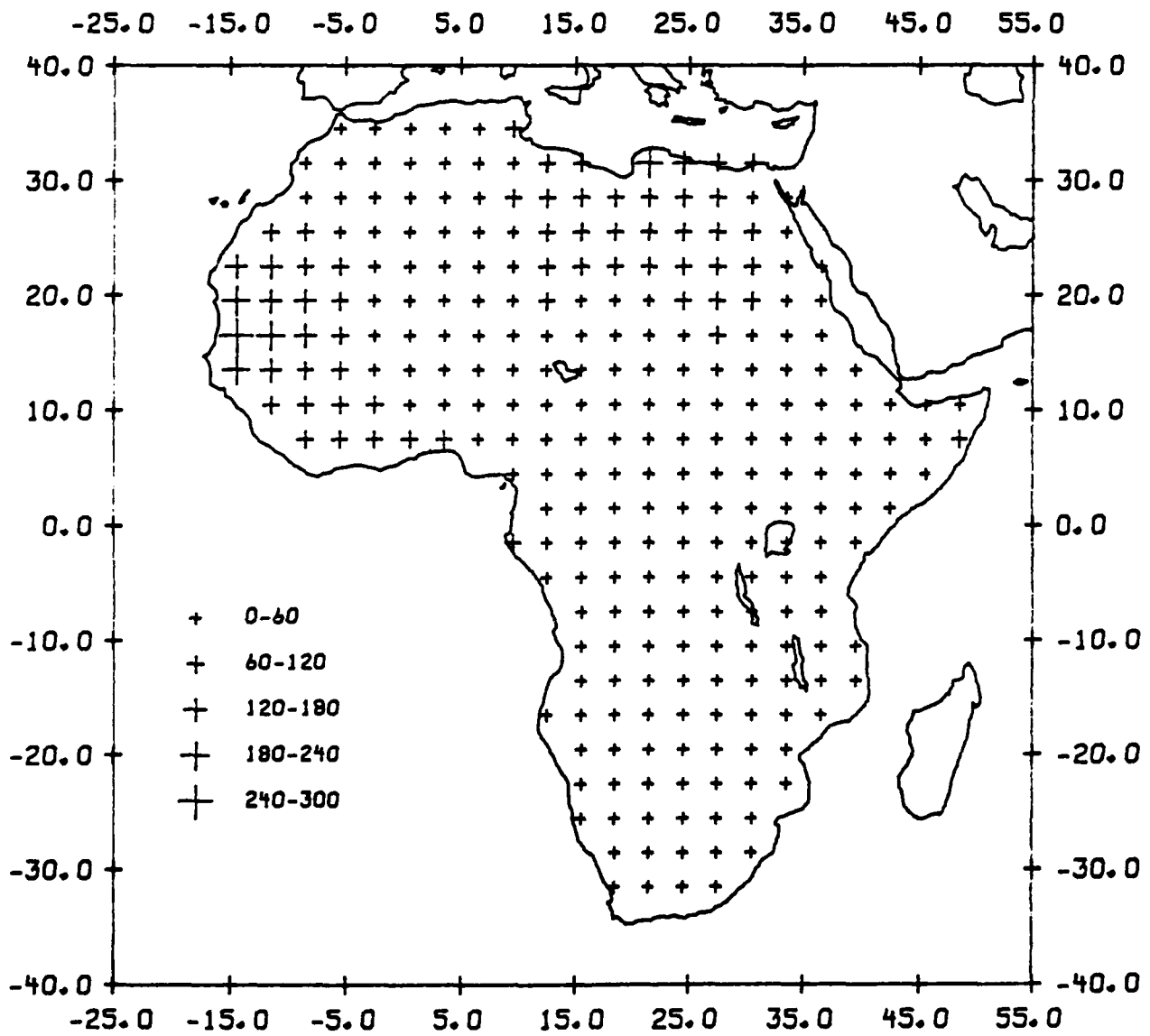


Figure 10

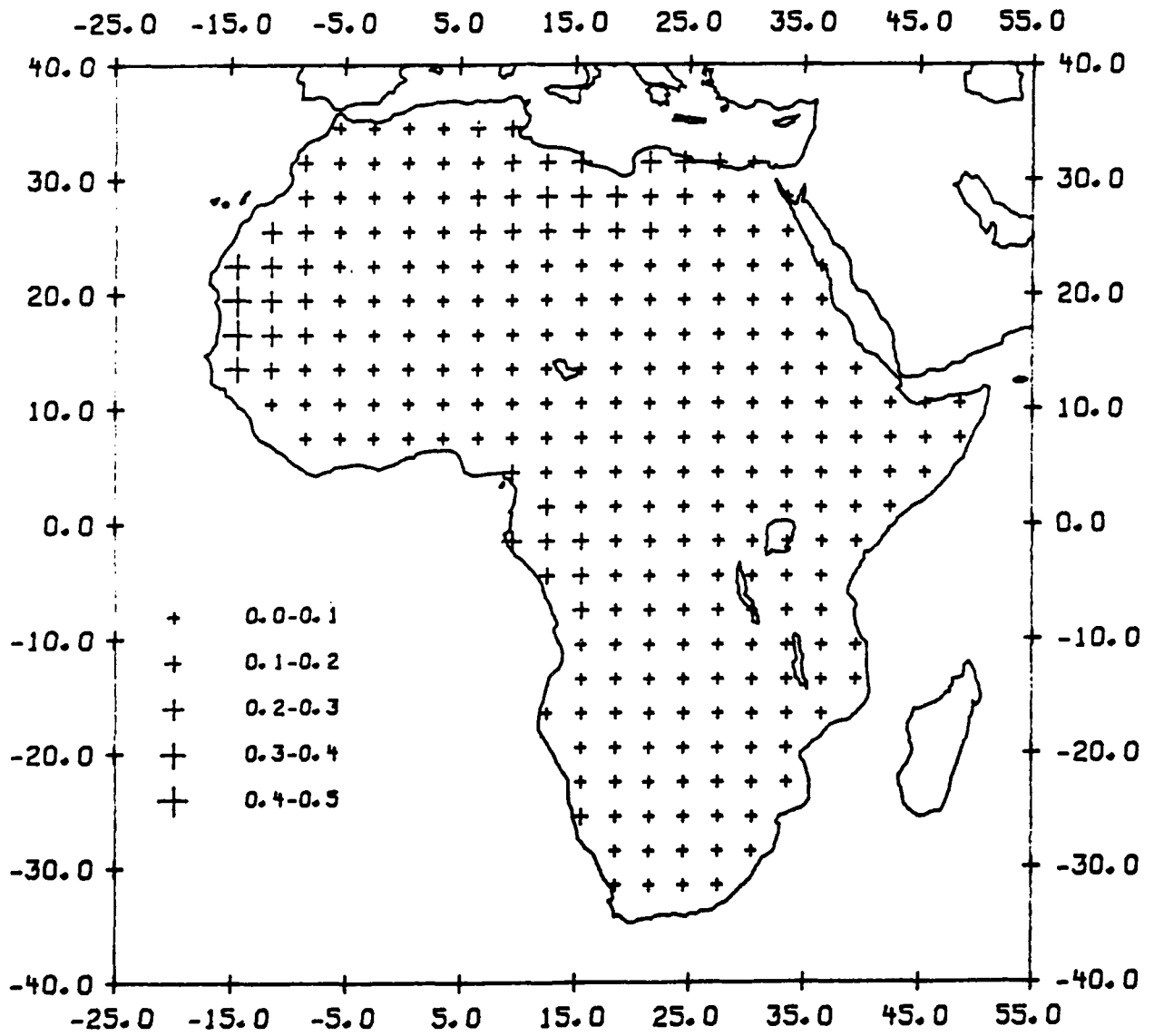


Figure 11

V. Three-Dimensional Attenuation structure in and around the New Madrid Seismic Zone

Haydar J. Al-Shukri and B. J. Mitchell Department of Earth and Atmospheric Sciences, St. Louis University, 3507 Laclede, St. Louis, MO 63103

ABSTRACT

Digital seismograms from the Central Mississippi Valley seismic network have been used to study the attenuation of body waves (Q_p^{-1}) in the New Madrid seismic zone and its surroundings. Q_p^{-1} were calculated for 252 seismograms using a spectral decay technique assuming that Q_p^{-1} is independent of frequency. The observed Q_p^{-1} values were inverted using a stochastic least-squares inversion scheme to determine a three-dimensional image of Q_p^{-1} in the upper crust. Homogeneous and heterogeneous upper crustal starting models produce similar images of Q_p^{-1} . The resulting models include a dramatic increase of attenuation within and close to the zones that contain the most active faults of the New Madrid seismic zone. This region was previously found (Al-Shukri and Mitchell, 1988) to be characterized by lower velocities than surrounding regions. The reduction in velocity and Q_p in the active portion of the New Madrid seismic zone are most easily explained as being caused by fluid-filled cracks in the upper crust. The presence or absence of fluid may govern whether or not faults in this region are active or inactive.

INTRODUCTION

The New Madrid seismic zone is the most seismically active region of central and eastern North America and was the site of the largest earthquakes to have occurred there (Fuller, 1912; Nuttli, 1973a). Most present-day activity in that zone occurs along three or four linear trends (Stauder *et al.*, 1976). Figure 1 shows those trends as well as faults

mapped in the region. The New Madrid region was the site of continental rifting during late Precambrian - early Paleozoic time (Ervin and McGinnis, 1975) which created a system of faults or zones of weakness that are thought to have been reactivated during periods when the regional stress field became favorably oriented with respect to those zones (Sbar and Sykes, 1973; Sykes, 1978; Zoback and Zoback, 1981; Braile *et al.*, 1982). Three-dimensional velocity models of a broad region around the seismically active zone (Mitchell *et al.*, 1977; Al-Shukri and Mitchell, 1987) indicate that both the crust and upper mantle beneath that zone are characterized by low seismic velocities.

Most of the seismicity of the New Madrid seismic zone occurs on a relatively small portion of a large fault system. That localization of activity to only part of the fault system suggests that the deviatoric stress required to generate motion along those portions is less than that required for other portions of system. Al-Shukri and Mitchell (1988), in a detailed study around the fault system, showed that the regions of enhanced seismic activity are also regions where seismic velocities are lower than those in surrounding rock. They attributed that reduction in velocity to interstitial fluids which, not only reduce velocities, but are conducive to the occurrence of earthquakes.

Another property which should be affected by the presence of interstitial fluids is the quality factor (Q) or its inverse, internal friction (Q^{-1}). Mitchell (1975, 1981) observed very large reductions in crustal Q in the western United States, as compared to the eastern United States, and attributed them to enhanced levels of fluid-filled cracks.

In the present study we use seismic attenuation data collected in the New Madrid region to obtain a three-dimensional model of internal friction for compressional waves (Q_p^{-1}). We build upon earlier work (Al-Shukri *et al.*, 1988) in which qualitative results suggested that paths through the active portion of the New Madrid seismic zone exhibit greater attenuation than do paths outside the zone. The general features of the model are compared to features of velocity models found earlier (Al-Shukri and Mitchell, 1987, 1988) to see if variations in both the Q_p^{-1} structure and velocity structure of the region

can be attributed to a single mechanism.

ATTENUATION OF SEISMIC WAVES

Spectral decay method

Although the attenuation of seismic waves has been given much scientific attention in recent years it is still a very difficult property to measure accurately to understand in terms of a causative mechanism. The difficulty is due largely to lateral variations in velocity structure which can cause systematic biases in measurement of attenuation and can produce scattering, the effects of which are difficult or impossible to separated from intrinsic Q mechanisms. The difficulty in measuring attenuation is partially offset by the large spatial variation in Q which can occur. Thus, if we are interested in determining regional variations of Q we can often resolve those variations even though the uncertainties in the Q values are large.

Our procedure for calculating attenuation (Q^{-1}) is the same that has been followed by Al-Shukri *et al*, (1988) and Hough *et al*, (1988). This procedure uses a single-station spectral-decay method described by Cormier (1982) for which we need to assume the slope of the source spectrum. To summarize the technique used to calculate Q^{-1} we utilized the definition of Anderson and Hough (1984) for the instrumentally corrected spectrum observed at a station located a distance r from the source. This definition is

$$A(r,f) = A_0(r,f) e^{-\pi f t^*} \quad (1)$$

where f is the frequency and t^* is the attenuation time which is defined (Cormier, 1982) as

$$t^* = \int_{\text{path}} \frac{dr}{QV} \quad (2)$$

where Q is the attenuation quality factor, V is the seismic wave velocity, and the integral is over the ray path. Following Hough *et al*, (1988) it is possible to redefine $A_0(r,f)$ as

$$A_o(r,f) = (2\pi f)^2 S(f) G(r) \quad (3)$$

where $S(f)$ is the source displacement spectrum and $G(r)$ is the geometric spreading which assumed to be independent of frequency. At high frequencies a widely accepted assumption is that the source displacement spectrum varies as ω^{-2} which occurs if $S(f) \propto f^{-2}$ (Brune, 1970; Madariaga, 1977; Hanks, 1979). This model has been assumed in studies which calculate attenuation from high frequency waves from teleseismic sources (Der and McElfresh, 1976; Lundquist and Cormier, 1980; Der *et al*, 1982; Der *et al*, 1985) as well as local or regional sources (Modiano and Hatzfeld, 1982; Anderson and Hough, 1984; Hough and Anderson 1988; Hough *et al*, 1988; Al-Shukri *et al*, 1988). If the source displacement spectrum has a form of ω^{-n} where n is different from 2 (e.g. Haskell, 1966; Aki, 1967; 1972; Madariaga, 1976; Archambeau, 1968; Evernden *et al*, 1986) then attenuation computations using the procedure described below will lead to values for Q^{-1} which are too high or too low depending on whether n is less than or greater than 2 respectively. Since our primary interest is not the absolute value of Q^{-1} but its spatial variation within the crust, assuming the ω^{-2} model should cause no difficulties in our results. According to this assumption A in (3) becomes independent of frequency; thus equation (1) can be rewritten, after taken the natural logarithm of both sides, as

$$\ln A(r,f) = \ln A_o(r) - \pi f t^*. \quad (4)$$

If t^* is frequency-independent then equation (4) can be differentiated with respect to f to obtain

$$\frac{d(\ln A(r,f))}{df} = -\pi t^*. \quad (5)$$

Equation (5) define the slope of the straight line described by equation (4). The value for the slope, $-\pi t^*$, is determined by fitting the observed spectrum by a straight line using a least-squares fit over the desired frequency range. Equation (2) can be

rewritten to yield

$$t^* = \int_{\text{path}} \frac{dt}{Q} \quad (6)$$

where t is the travel time. The attenuation (Q^{-1}) of body waves has a strong dependency on travel time or epicentral distance (Cormier, 1982; Modiano and Hatzfeld, 1982; Anderson and Hough 1984; Hough and Anderson, 1988; Hough *et al.*, 1988; Ho-Liu *et al.*, 1988; Al-Shukri *et al.*, 1988). This makes the numerical calculation of t^* in equation (6) impossible without *a priori* knowledge of Q^{-1} along the ray path. If we assume that Q_0^{-1} represent an average value of Q^{-1} along the ray path (Der and Lees, 1985) t^* in (6) become

$$t^* = \frac{t}{Q_0} \quad (7)$$

There have been many indications that attenuation is frequency dependent (e.g. Mitchell, 1980) and the degree of dependence also varies regionally (Mitchell, 1981). It is not possible, however, with the data used in this study to determine the nature of this dependence. Furthermore, the primary goal of this study is to investigate the spatial variations of attenuation in the upper crust of the New Madrid area, hence the use of frequency - independent attenuation is an appropriate approximation for this study.

Data and Computation

The central Mississippi Valley seismic network has monitored seismicity in the New Madrid seismic zone since 1974 and began recording digitally in 1980. Digital seismograms from local earthquakes were used to obtain body-wave spectra for 82 local events in the network region. Those earthquakes range in magnitude between 1.3 and 3.4 and they are chosen because of their fairly accurate location and origin time. Figure 2 shows the earthquakes and stations used in this study. The procedure used to determine the spectrum and calculating attenuation of body waves is the same that has been used by

Hough *et al*, (1988) to calculate attenuation of P and S waves and Al-Shukri *et al*, (1988) for calculating Q_p , and it will not be repeated here. The procedure followed here differs from that of Hough *et al*, (1988) by using a Parzen window instead of a cosine window. In previous studies we found the Parzen window to produce the smoother spectrum of the two. Windowing the time series with a Parzen window eliminates the need for smoothing the spectrum before fitting the general trend with a least-squares straight line. Figure 3 shows examples of time series and their acceleration spectra used for calculating attenuation.

Earlier work on attenuation in the New Madrid region (Al-Shukri and Mitchell, 1988) indicates that the average Q_p^{-1} increases greatly with distance suggesting that it also increases with depth. Its values range between about 0.025 for epicentral distances less than 10 km to less than 0.001 for epicentral distances of over 200 km. Figure 4 indicates the dependence of Q_p^{-1} on distance. This figure also indicates that average Q_p^{-1} has a very wide range of values for distances less than about 40 km. A reasonable explanation for this observation is that the data were collected from a region with large lateral variations of attenuation. For short distances Q_p^{-1} was averaged over small volume of crustal material and its value represents the local effect of this material. If lateral variation in attenuation exists, Q_p^{-1} values calculated for waves traveled short distances represent the localized values of attenuation in the region. For a longer ray paths Q_p^{-1} values are averaged over a larger volume of crustal material and the lateral variation will be smoothed out. Q_p^{-1} calculated for longer ray paths represent the regional average and the variation with distance is smooth. These features appear clearly in Figure 4.

The relationship between attenuation and epicentral distance can be examined further by plotting t^* versus distance as shown in Figure 5. The scatter in the t^* data is larger than that in the Q_p^{-1} data suggesting that velocity, as well as Q_p^{-1} , varies regionally (Al-Shukri and Mitchell, 1988). A least-squares straight-line fit to this data results

$$t_p^* = 0.034 \text{ (sec)} + (0.000012 \text{ (sec/km)}) R \quad (8)$$

where R is the source-receiver distance. Anderson and Hough (1984) indicate that the finite intercept of the line (0.034 sec in our case) corresponds to attenuation which the waves encounter in traveling vertically through the subsurface geological structure to the surface of the earth. The slope (0.000012 sec/km in our case) corresponds to attenuation caused predominantly from horizontal propagation of waves in the crust. Those authors also indicate that attenuation properties at shallow depths dominate the total wave attenuation. The New Madrid attenuation data also appear to be affected most strongly by near-surface structure.

The extremely low value for the slope for the t^* data in Figure 5 is an indication of the efficient transmission of seismic energy that characterizes central and eastern North America. This results is consistent with the conclusions of Nuttli (1973b) and Mitchell (1973) that attenuation is very low in those regions, thus providing an explanation for the much larger area of perceptibility in central and eastern North America as compared to western North America.

Al-Shukri *et al.*, (1988) showed that, in addition to the general increase with distance, Q_p^{-1} also varies spatially in the New Madrid region. Figure 6 shows examples of Q_p^{-1} values for different ray paths. This figure indicates that for an approximately equal path length Q_p^{-1} values within the highly active zone are substantially higher than those for paths which lie predominantly outside the zone. Al-Shukri *et al.*, (1988) indicate that Q_p^{-1} values for paths that are confined to the active region are 2 to 3 times higher than for those paths which are predominantly outside this region.

LINEAR INVERSION OF Q_p^{-1}

Method

Least - squares inversion scheme was developed for determining a three - dimensional image of Q^{-1} within a specific volume of the earth beneath a local or regional

seismic network. The data used by this technique are the observed average Q^{-1} values calculated for P or S waves. The inversion procedure starts by dividing the volume of the Earth beneath the network into a number of layers, each layer is subdivided into a number of right rectangular prisms (blocks) in which both velocity and Q^{-1} are assumed to be constant. This discretization permits the calculation of the theoretical t^* (t_{th}^*) in each block traced by a seismic ray. The integral of equation (2) can then be written for the parameterized Earth model as

$$t_{th}^* = \sum_{i=0}^N t_i Q_i^{-1} \delta_i \quad (9)$$

where N is the number of block in the model and δ_i is a Dirac delta function equal to unity inside each block that has been traced by the ray and zero elsewhere. Assuming that the observed t^* (t_{ob}^*) can be parametrized in a fashion similar to that in equation (9), the difference between t_{ob}^* and t_{th}^* can be written as follow

$$t_{ob}^* - t_{th}^* = \sum_{i=1}^N \delta_i \left(t_{iob} Q_{iob}^{-1} - t_{ith} Q_{ith}^{-1} \right) . \quad (10)$$

If t_{ith} is factored from the right hand side, equation 10 becomes

$$\delta t^* = \sum_{i=1}^N \delta_i t_{ith} \left(\frac{t_{iob}}{t_{ith}} Q_{iob}^{-1} - Q_{ith}^{-1} \right) . \quad (11)$$

where δt^* is $t_{ob}^* - t_{th}^*$. Al-Shukri and Mitchell (1987, 1988) indicate that the rms travel-time residuals of P waves in their final three - dimensional velocity models is less than 0.2 sec. This represents, on the average, about 2% of the average travel-time of 10 sec. Assuming that their models are unique, it is possible to approximate the ratio t_{iob}/t_{ith} in (11) by unity. For M observations a system of equations can be formed as

$$\begin{pmatrix} \delta t_1^* \\ \vdots \\ \delta t_M^* \end{pmatrix} = \begin{pmatrix} \delta_1 t_{11} & \delta_2 t_{21} & \cdot & \cdot & \cdot & \delta_N t_{N1} \\ \cdot & \cdot & \cdot & \cdot & \cdot & \cdot \\ \cdot & \cdot & \cdot & \cdot & \cdot & \cdot \\ \cdot & \cdot & \cdot & \cdot & \cdot & \cdot \\ \cdot & \cdot & \cdot & \cdot & \cdot & \cdot \\ \delta_1 t_{1M} & \delta_2 t_{2M} & \cdot & \cdot & \cdot & \delta_N t_{NM} \end{pmatrix} \begin{pmatrix} \delta Q_1^{-1} \\ \cdot \\ \cdot \\ \cdot \\ \delta Q_N^{-1} \end{pmatrix}, \quad (12)$$

where δQ_i^{-1} is the unknown attenuation perturbation ($Q_{i_{ob}}^{-1} - Q_{i_{th}}^{-1}$) for the i^{th} block through which rays have traveled for a particular time. Note that t_{ij} in (12) is the theoretical travel time in the i^{th} block from the j^{th} observation. Equation (12) can be rewritten in a matrix form as

$$y = \mathbf{T} \mathbf{q}, \quad (13)$$

where y is the δt^* vector, \mathbf{T} is the travel time matrix and \mathbf{q} is the unknown vector of attenuation perturbations. A stochastic least-squares solution to (13) is given by

$$\hat{\mathbf{q}} = [\mathbf{T}^T \mathbf{T} + \theta^2 \mathbf{I}]^{-1} \mathbf{T}^T \mathbf{q}, \quad (14)$$

where $\hat{\mathbf{q}}$ is the approximate solution to \mathbf{q} , θ^2 is a positive constant damping parameter and \mathbf{I} is the identity matrix. Due to the expected errors in computing t_{ob}^* using the spectral decay technique, the system of equations in (13) is set to be overdetermined. The stochastic least-squares solution was preferred because it produces a more stable solution than the undamped solution. The resolution matrix for the solution is given by

$$\mathbf{R} = [\mathbf{T}^T \mathbf{T} + \theta^2 \mathbf{I}]^{-1} \mathbf{T}^T \mathbf{T} \quad (15)$$

and the covariance matrix by

$$\mathbf{C} = \sigma_d^2 [\mathbf{T}^T \mathbf{T} + \theta^2 \mathbf{I}]^{-1} \mathbf{R} \quad (16)$$

where σ_d^2 is the variance of the error in the data. The standard errors of the solution equal the square root of the diagonal element of \mathbf{C} . The above scheme permits us to

obtain the final solution iteratively and the convergence of the solution can be examined at each step.

The singular value decomposition method of Lawson and Hanson (1974) was used to obtain the stochastic least-squares solution (14). This method uses efficient orthogonal decomposition of matrices with Housholder transformations. Eigenvalues of transformed system are modified according to stochastic inverse theory (Franklin, 1970; Wiggins, 1972). Al-Shukri and Mitchell (1987, 1988) used this inversion technique to obtain three - dimensional velocity models for the New Madrid region.

The essential step of the forward solution for setting the system of equations in (12) is the calculation of the travel time matrix. The travel time in each individual block traced by a ray was calculated using a ray tracing algorithm in which blocks are assumed to be homogeneous and rays within these blocks are approximated by a straight-line paths (Figure 7). Thurber and Ellsworth (1980) showed that on the bases of numerical integration through a heterogeneous medium the straight line segments provide an excellent approximation to the actual travel time. A numerical integration procedure similar to the one used by Thurber and Ellsworth (1980) was used to calculate travel times. In the procedure used here the ray is divided into a number of segments having equal lengths. The travel time for each segment of a particular ray was calculated and the times for all segments that belong to the individual block were added to form the total travel time in this block. If a ray hits a block or layer boundary the length of the segment is modified to become the distance between the end of the last segment and the boundaries. The travel-time for this modified segment was calculated accordingly.

The inversion procedure has been tested extensively using a number of starting models and synthetic data sets. Both homogeneous and heterogeneous models were used to generate synthetic data for average Q^{-1} . These data were then inverted using a number of different starting models. In all cases, with sufficient number of observations, solutions using error - free synthetic data converged perfectly to the expected solutions.

Random errors of different percentage (5, 10, 20, 50 %) were added to the synthetic data to examine their effect on the solution. The errors in the final solution (difference between final solution and the expected one) are usually less than the level of the data errors. These errors, as expected, are inversely proportional to the number of observations in the data set. A continuous increase in the number of observations for a particular noisy data set is found to gradually improve the solution. Improving the solution does not however, mean reducing the Q_p^{-1} rms residuals ($Q_{ob}^{-1} - Q_{th}^{-1}$). For a certain error level these rms residuals reach a value which are simply proportional to the error level in the data.

Result

The inversion procedure requires a velocity model for ray tracing and a starting Q_p^{-1} model. A number of combinations of velocity and Q_p^{-1} model have been used to invert the 252 Q_p^{-1} observations collected in the New Madrid region. Only two of these models will be presented here. The first one has a velocity model which assumes that the upper crust consists of two layers, the upper layer having a thickness of 5.0 km and a velocity of 5.95 km/sec, the lower layer having a thickness of 9.0 km and a velocity of 6.20 km/sec. This model is a simplified form of a model given by Mooney *et al*, (1983) for the region. The starting Q_p^{-1} model is also a two layer model having the same thicknesses and Q_p^{-1} values of 0.005 for all blocks in the upper layer and 0.002 for all blocks in the lower layer. The half space was assigned a starting Q_p^{-1} value of 0.001 (the Q_p^{-1} value for the half space was considered to be an unknown and was solved for). The final solution and its standard errors using the first starting model is shown in Figures 8a and 8b for the upper and lower layers, respectively. The second model has the same starting Q_p^{-1} model, but the velocity model is a three - dimensional heterogeneous model derived by Al-Shukri and Mitchell (1987, 1988) using travel-time residuals from local earthquakes. Figure 9 shows the three - dimensional velocity assigned for the blocks in the second model. Figures 10a and 10b show Q_p^{-1} variations and their standard

errors in the upper and lower layers respectively. In both models the two layers were subdivided into a number of blocks having horizontal dimensions of 60 by 60 km.

The three - dimensional variation of Q_p^{-1} obtained using the first starting model (Figure 8) is almost identical to variation resulting from the second model (Figure 10). This indicates that the difference in travel-time residuals for the two starting models have a very small effect on the Q_p^{-1} inversion. The travel-time residuals do, however, show some effect on the final Q_p^{-1} value when the difference in block velocity in the two models become large. For example in the lower layer of both models (Figure 8b and 10b) block number 3 of the first row has one of the largest velocity difference (Figure 9) between the two velocity models and also has the greatest difference in Q_p^{-1} values (0.00214 and 0.00135).

The attenuation within the upper 5 km of the crust (Figures 8a and 10a) varies by about factor of 3 between the highest (0.016) and lowest (0.004) values. The pattern of Q_p^{-1} variations in this layer is a gradual increase in values from the outside to the inside in almost all directions. This increase in attenuation correlates with a general increase of earthquake activity in the region. The highest value of Q_p^{-1} (0.016) occurs in the block that has the highest level of seismic activity of the New Madrid earthquake zone (Figures 8a and 10a).

The lateral variations of attenuation in the upper layer indicate that the alluvium layer, which covers the southwest part of the region (Figure 1), has little effect on the Q_p^{-1} values. The thickness of alluvium increases gradually to the southwest and reaches a maximum thickness of about 1 km in the extreme southwest of the studied region. If attenuation in the alluvium has a measurable effect on Q_p^{-1} , a trend of increasing attenuation should parallel the increase in thickness, but Figures 8a and 10a show no such trend. In addition the models show no difference in attenuation between the northern part of the region (no alluvial cover) and the southwest part (alluvium is about 1 km thick), indicating that alluvial cover has little effect on the average Q_p^{-1} in the

blocks.

In the depth range of 5 - 14 km (lower layer) the Q_p^{-1} values range between 0.0033 and 0.00001 (Figures 8b and 10b). These highest value occurs in a region of intense earthquake activity, while the lowest value occurs in the extreme northern part of the region. The lateral variation of Q_p^{-1} in this layer is much smaller than the variation in the upper layer. This is possibly caused by greater of variations in the local subsurface geology in the upper layer, but may also be related to the closing of cracks in the crust as discussed in the following section.

Both starting models resulted in a comparable value of Q_p^{-1} in the half space (0.00033 and 0.00027 for models 1 and 2 respectively). In the ray tracing and inversion the half space was considered as a single unit that extended below the lower boundary of the lower layer at a depth of 14 km. The lateral changes in Q_p^{-1} in the half space were not considered because very few regions of the half space were sampled by rays. Accordingly it is reasonable to consider the half space to be homogeneous and the value of Q_p^{-1} given in the model represents an average value for few kilometers below the lower layer.

DISCUSSION

Al-Shukri and Mitchell (1987) used travel-time residuals from teleseismic and local earthquakes to derive three - dimensional velocity models for the crust and upper mantle for the New Madrid seismic zone. Their models show that the upper crust exhibits a regional low velocity trend that correlates in position with the rift complex identified by Hildenbrand *et al*, (1977). These models show also the existence of a localized low velocity zone that correlate spatially with a region of high seismic activity. A more detailed analysis by Al-Shukri and Mitchell (1988) indicates a remarkable correlation between low P-wave velocities and earthquake activity in the region. In an attempt to explain this observation, they propose a physical model based on the laboratory results of Nur and

Simmons (1969). This model stated that the reduction in seismic velocities in the part of the crust containing the active trends of seismicity was caused by an increase in the concentration of fluid - filled cracks in which the pore pressure is a substantial fraction of the external pressure in the region.

If fluid - filled cracks cause the reduction in seismic velocities observed in the New Madrid region, they should also increase seismic wave attenuation. Laboratory measurements have indicated that interstitial fluids greatly reduce Q values in rock samples (Gardner *et al.*, 1964; Toksöz *et al.*, 1970; Winkler and Nur, 1979; Johnston, 1981; Tittmann *et al.*, 1981; Winkler and Nur, 1982). Although other mechanisms cannot be definitely be ruled out at the present time, the correlation of low velocities and low Q values and their association with enhanced seismic activity, makes our model a very compelling one.

In addition to the lateral correlation between velocity and Q , there is a correlation with depth, both velocity and Q showing smaller variation at greater depths. These smaller variations with depth are most easily be explained by the closing of cracks as pressure becomes greater at larger depths.

The three - dimensional P-wave velocity models of Al-Shukri and Mitchell (1987, 1988) and the three - dimensional Q_p^{-1} model presented here can be most readily explained as being produced by fluid-filled cracks and microcracks in the crust. In addition to reducing velocities and increasing attenuation, it is likely that the fluids within preexisting zones of weakness will reduce the amount of the deviatoric stress required to generate motion. The presence of fluids in the crustal material of this region may therefore explain the observed abnormal concentration of earthquake activity of the New Madrid seismic zone.

ACKNOWLEDGMENTS

We thank H. Ghalib for providing us with his program for computing amplitude spectra.

This report was partially supported by the Advanced Research Projects Agency of the Department of Defense and was monitored by the Air Force Geophysics Laboratory under contract F19628-87-k-0036.

REFERENCES

- Aki, K. (1967). Scaling law of seismic spectrum, *J. Geophys. Res.* **72**, 1217-1231.
- Aki, K. (1972). The scaling law of the earthquake source time spectrum, *Geophys. J. R. Astr. Soc.* **31**, 3-25.
- Al-Shukri, H. J. and B. J. Mitchell (1987). Three-dimensional velocity variations and their relation to the structure and tectonic evolution of the New Madrid seismic zone, *J. Geophys. Res.* **92**, 6377-6390.
- Al-Shukri, H. J. and B. J. Mitchell (1988). Reduced seismic velocities in the source zone of New Madrid earthquakes, *Bull. Seism. Soc. Am.* **78**, 1491-1509.
- Al-Shukri, H. J., B. J. Mitchell, and H. A. A. Ghalib (1988). Attenuation of seismic waves in the New Madrid seismic zone, *Seismo. Res. Lett.* (in press).
- Anderson, J. G. and S. Hough (1984). A model for the shape of the Fourier amplitude spectrum of acceleration at high frequencies, *Bull. Seism. Soc. Am.* **74**, 1969-1993.
- Archambeau, C. B. (1968). General theory of elastodynamic source fields, *Rev. Geophys.* **6**, 241-288.
- Braile, L. W., G. R. Keller, W. J. Hinze, and E.G. Lidiak (1982). An ancient rift complex and its relation to contemporary seismicity in the New Madrid seismic zone, *Tectonics* **1**, 225-237.
- Brune, J. N. (1970). Tectonic stress and the spectra of seismic shear waves from earthquakes, *J. Geophys. Res.* **75**, 4997-5009.

- Cormier, V. F. (1982). The effect of attenuation on seismic body waves, *Bull. Seism. Soc. Am.* **72**, S169-S200.
- Der, Z. A. and A. C. Lees (1985). Methodologies of estimating $t^*(f)$ from short period body waves and regional variations of $t^*(f)$ in the United States, *Geophys. J. R. Astr. Soc.* **82**, 125-140.
- Der, Z. A. and T. W. McElfresh (1976). Short period P wave attenuation along various paths in North America as determined from P wave spectra of the Salmon Nuclear Explosion, *Bull. Seism. Soc. Am.* **66**, 1609-1622.
- Der, Z. A., T. McElfresh, and A. O'Donnell (1982). An investigation of the regional variation and frequency dependence of unelastic attenuation in the mantle under the United States in the 0.5-4 Hz band, *Geophys. J. R. Astr. Soc.* **69**, 67-100.
- Der, Z., T. McElfresh, R. Wagner, and J. Burnetti (1985). Spectral characteristics of P wave from nuclear explosions and yield estimation, *Bull. Seism. Soc. Am.* **75**, 379-390.
- Ervin, C. P. and L. D. McGinnis (1975). Reelfoot rift: Reactivated precursor to the Mississippi Embayment, *Geol. Soc. Am. Bull.* **86**, 1287-1295.
- Evernden, J. F., C. B. Archambeau, and E. Cranswick (1986). An evaluation of seismic decoupling and underground nuclear test monitoring using high frequency seismic data, *Rev. Geophys.* **24**, 143-215.
- Gardner, G. H. F., M. R. J. Wyllie and D. M. Droschak (1964). Effects of pressure and fluid saturation on the attenuation of elastic waves in sands, *J. Petroleum. Tech.* **16**, 189-198.
- Franklin, J. (1970). Well-posed stochastic extensions of ill-posed linear problems, *J. Math. Anal. Appl.* **21**, 682-716.
- Fuller, M. L. (1912). The New Madrid earthquake, *U. S. Geol. Surv. Bull.* **494**, Washington, D.C.
- Hanks, T. C. (1979). b-values and $\omega^{-\gamma}$ seismic source models: implications for tectonic

- stress variations along active crustal fault zones and the estimation of high-frequency strong ground motion, *J. Geophys. Res.* **84**, 2235-2242.
- Haskell, N. A. (1966). Total energy and energy spectral density of elastic wave propagation from propagating faults. Part II, *Bull. Seism. Soc. Am.* **56**, 125-140.
- Heyl, A. V. and F. A. McKeown (1978). Preliminary seismotectonic map of central Mississippi valley and environs, *U.S. Geol. Surv. Misc. Field stud. Map*, **MF-1011**.
- Hil'enbrand, T. G., M. F. Kane, and W. Stauder (1977). Magnetic and gravity anomalies in the northern Mississippi Embayment and their spatial relation to seismicity, *U.S. Geol. Surv. Misc. Field Stud. Map*, **MF-914**.
- Hough, S. E., J. G. Anderson, J. Brune, F. Vernon, III, J. Berger, J. Fletcher, L. Haar, T. Hanks, and L. Baker (1988). Attenuation near Anza, California, *Bull. Seism. Soc. Am.* **78**, 672-691.
- Hough, S. E. and J. G. Anderson (1988). High-frequency spectra observed at Anza, California: implications for Q structure, *Bull. Seism. Soc. Am.* **78**, 692-707.
- Ho-Liu P., H. Kanamori, and R. W. Clayton (1988). Application of attenuation tomography to Imperial Valley and Coso-Indian Wells region, Southern California, *J. Geophys. Res.*, **93**, 10,501-10,520.
- Johnston, D. H. (1981). Attenuation: a state of the art summary, in seismic wave attenuation, Toksöz, M. N. and D. H. Johnston (Eds), *Soc. Explor. Geophys.*, Tulsa, Okla.
- Lawson, C. L. and R. J. Hanson (1974). *Solving Least Squares Problems*. Prentice-Hall, Inc., Englewood Cliffs, New Jersey.
- Lundquist, G. M. and V. F. Cormier (1980). Constraints on the absorption band model of Q, *J. Geophys. Res.* **85**, 5244-5265.
- Madariaga, R. (1976). Dynamics of an expanding circular fault, *Bull. Seism. Soc. Am.* **66**, 639-666.

- Madariaga, R. (1977). High-frequency radiation from crack (stress drop) models of earthquake faulting, *Geophys. J. R. Astr. Soc.* **51**, 625-651.
- Mitchell, B. J. (1973). Radiation and attenuation of Rayleigh waves from the southeastern Missouri earthquake of October 21, 1965, *J. Geophys. Res.*, **78**, 886-899.
- Mitchell, B. J. (1975). Regional Rayleigh wave attenuation in North America, *J. Geophys. Res.* **80**, 4904-4916.
- Mitchell, B. J. (1980). Frequency dependence of shear wave internal friction in the continental crust of eastern North America, *J. Geophys. Res.* **85**, 5212-5218.
- Mitchell, B. J. (1981). Regional variation and frequency dependence on Q_β in the crust of the United States, *Bull. Seism. Soc. Am.* **71**, 1531-1538.
- Mitchell, B. J., C. C. Cheng, and W. Stauder (1977). A three-dimensional model of the lithosphere beneath the New Madrid seismic zone, *Bull. Seism. Soc. Am.* **67**, 1061-1074.
- Modiano, T. and D. Hatzfeld (1982). Experimental study of the spectral content for shallow earthquakes. *Bull. Seism. Soc. Am.* **72**, 1739-1758.
- Mooney, W. D., M. C. Andrews, A. Ginzburg, D. A. Peters, and R. M. Hamilton (1983). Crustal structure of the northern Mississippi Embayment and a comparison with other continental rift zone, *Tectonophysics* **94**, 327-348.
- Nur, A. and G. Simmons (1969). The effect of saturation on velocity in low porosity rocks, *Earth and Planet. Sci. Ltr.* **7**, 183-193.
- Nuttli, O. W. (1973a). The Mississippi Valley earthquakes of 1811 and 1812: Intensities, ground motion and magnitudes, *Bull. Seism. Soc. Am.* **63**, 227-248.
- Nuttli, O. W. (1973b). Seismic wave attenuation and magnitude relations from eastern North America, *J. Geophys. Res.* **78**, 876-885.
- Sbar, M. L., and L. R. Sykes (1973). Contemporary compressive stress and seismicity in eastern North America: An example of intraplate tectonics, *Geol. Soc. Am.*

Bull. **84**, 1861-1882.

- Stauder, W., M. Kramer, G. Fischer, S. Schaefer, and S. T. Morrissey (1976). Seismic characteristics of southeast Missouri as indicated by a telemetered microearthquake array, *Bull. Seism. Soc. Am.* **66**, 1953-1964.
- Sykes, L. R. (1978). Intraplate seismicity, reactivation of pre-existing zones of weakness, alkaline magmatism, and other tectonism postdating continental fragmentation, *Rev. Geophys. Space Phys.*, **16**, 621-688.
- Thurber C. H. and W. L. Ellsworth (1980). Rapid solution or ray tracing problems in heterogeneous media, *Bull. Seismo. Soc. Am.*, **70**, 1137-1148.
- Tittmann, B. R., H. Nadler, V. A. Clark, and L. A. Ahlberg (1981). Frequency dependence of seismic dissipation in saturated rocks, *Geophys. Res. Lett.* **8**, 36-38.
- Toksöz, M. N., D. H. Johnston, and A. Timur (1979). Attenuation of seismic waves in dry and saturated rocks: I. Laboratory measurements, *Geophysics* **44**, 681-690.
- Wiggins, R. A. (1972). The general linear inverse problem: Implication of surface waves and free oscillations for earth structure, *Rev. Geophys. Space. Phys.* **10**, 251-285.
- Winkler, K. and A. Nur (1979). Pore fluids and seismic attenuation in rocks, *Geophys. Res. Lett.* **6**, 1-4.
- Winkler, K. W. and A. Nur (1982). Seismic attenuation: effect of pore fluids and frictional sliding, *Geophysics* **47**, 1-15.
- Zoback, M. D., and M. L. Zoback (1981). State of stress and intraplate earthquakes in the United States, *Science* **213**, 96-104.

DEPARTMENT OF EARTH AND ATMOSPHERIC SCIENCES
 SAINT LOUIS UNIVERSITY
 SAINT LOUIS, MO 63103

LIST OF FIGURE CAPTIONS

Figure 1

Map of the northern Mississippi Embayment (shaded) and surrounding tectonic features (modified from Heyl and McKeown, 1978). Circles denote some of the earthquake epicenters located by the U.S. Geological Survey/Nuclear Regulatory Commission Central Mississippi Valley seismic stations operated by Saint Louis University (triangles) (Stations OLY, EBZ, and SFTN operated by the Center for Earthquake Research and Information).

Figure 2

Ray path coverage from local earthquakes used to determine Q_p^{-1} variations in the upper crust. The shaded area indicates the Mississippi Embayment.

Figure 3

Representative examples of time series with the corresponding acceleration spectra and average Q_p value. fl and fh are low and high frequency limits, respectively, between which each spectrum is fitted by a straight line. Date and name of recording site are given in the lower left-hand corner of each diagram.

Figure 4

Q_p^{-1} versus distance for the data used in the three - dimensional inversion.

Figure 5

t^* as a function of distance. The solid line is a least squares fit through the data and is described by the equation

$t^* = 0.0034(\text{sec}) + (0.000012(\text{sec/km})) R(\text{km})$, where R is distance in km.

Figure 6

Q_p^{-1} values ($\times 10^5$) determined for several selected paths. The shading delineates the most seismically active areas.

Figure 7

Schematic diagram of a multi-layer Earth model. Ray segments indicate possible first arrival P-wave paths.

Figure 8

Q_p^{-1} values ($\times 10^5$) in the 5-km thick upper layer (a) and the 9-km thick lower layer (b) resulting from an inversion in which the velocity model is assumed to consist of two homogeneous layers.

Figure 9

Velocities assigned to the upper 5-km thick layer (upper number) and to the lower 9-km thick layer (lower number) for a Q_p^{-1} inversion using a laterally heterogeneous velocity model. Each block is 60 km by 60 km in area and the indicated velocities are averages of velocities obtained by Al-Shukri and Mitchell (1987) using 30 km by 30 km blocks.

Figure 10

Same as Figure 8 using the laterally heterogeneous starting model of Figure 9.

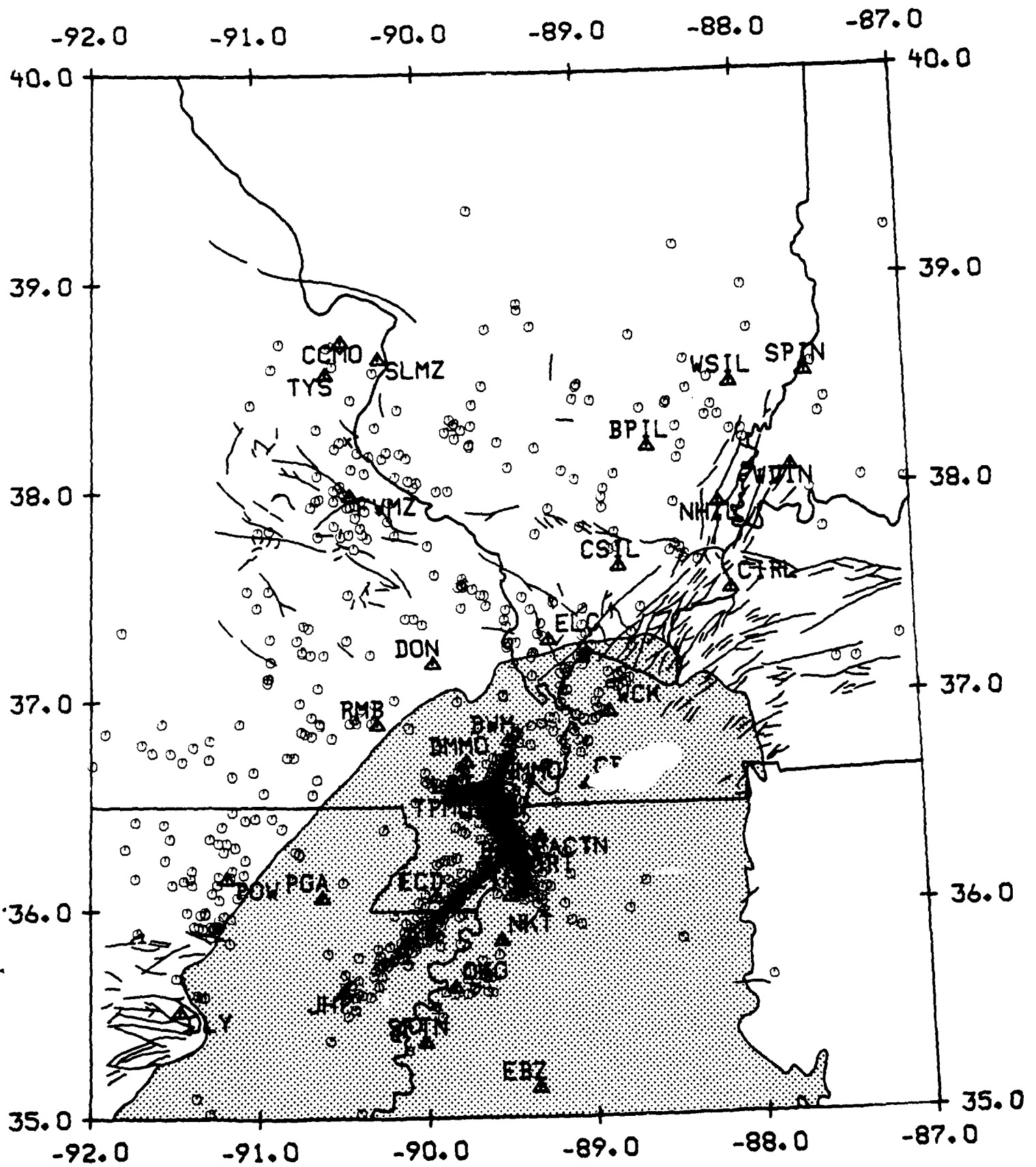


FIGURE 1

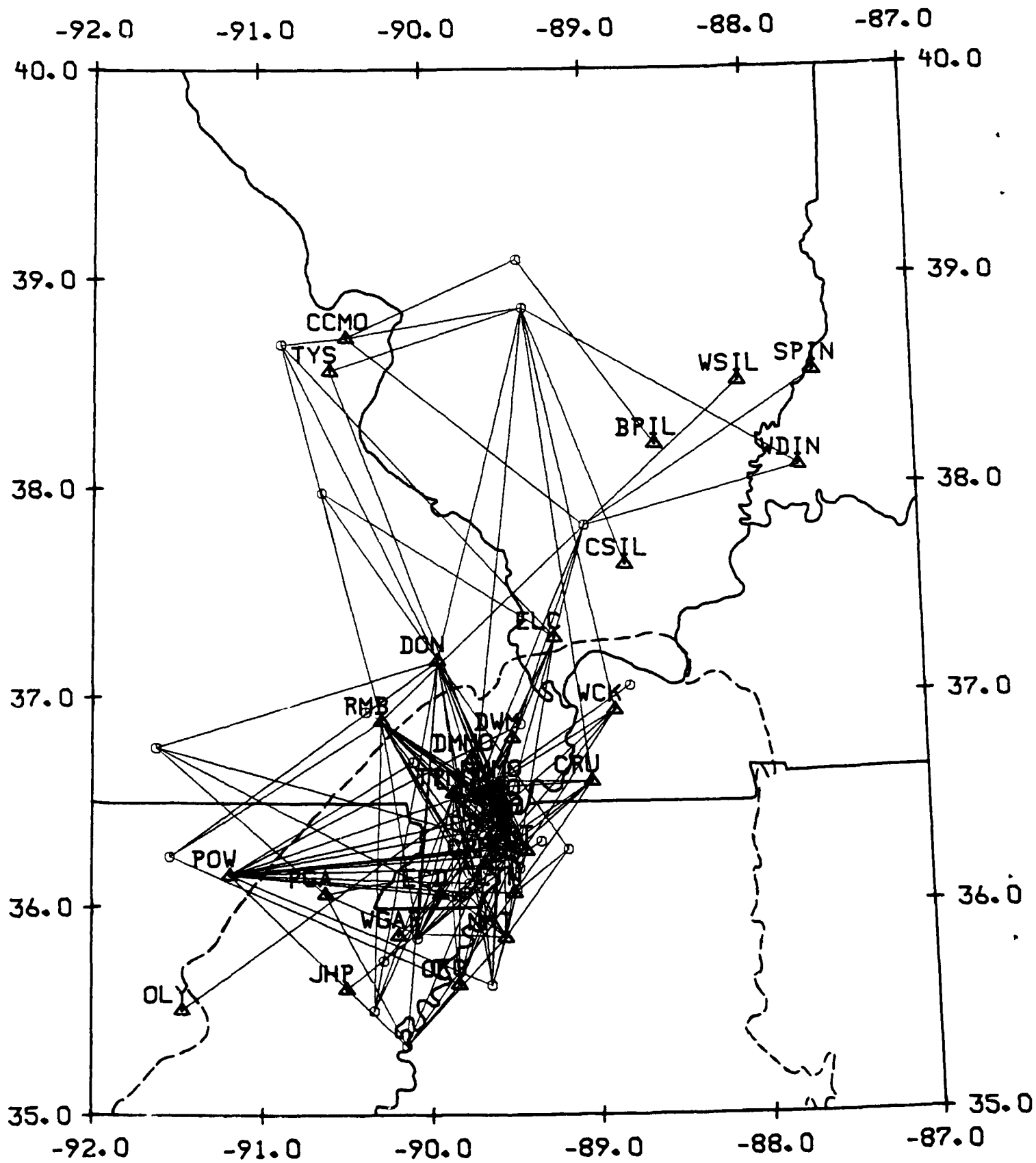


FIGURE 2

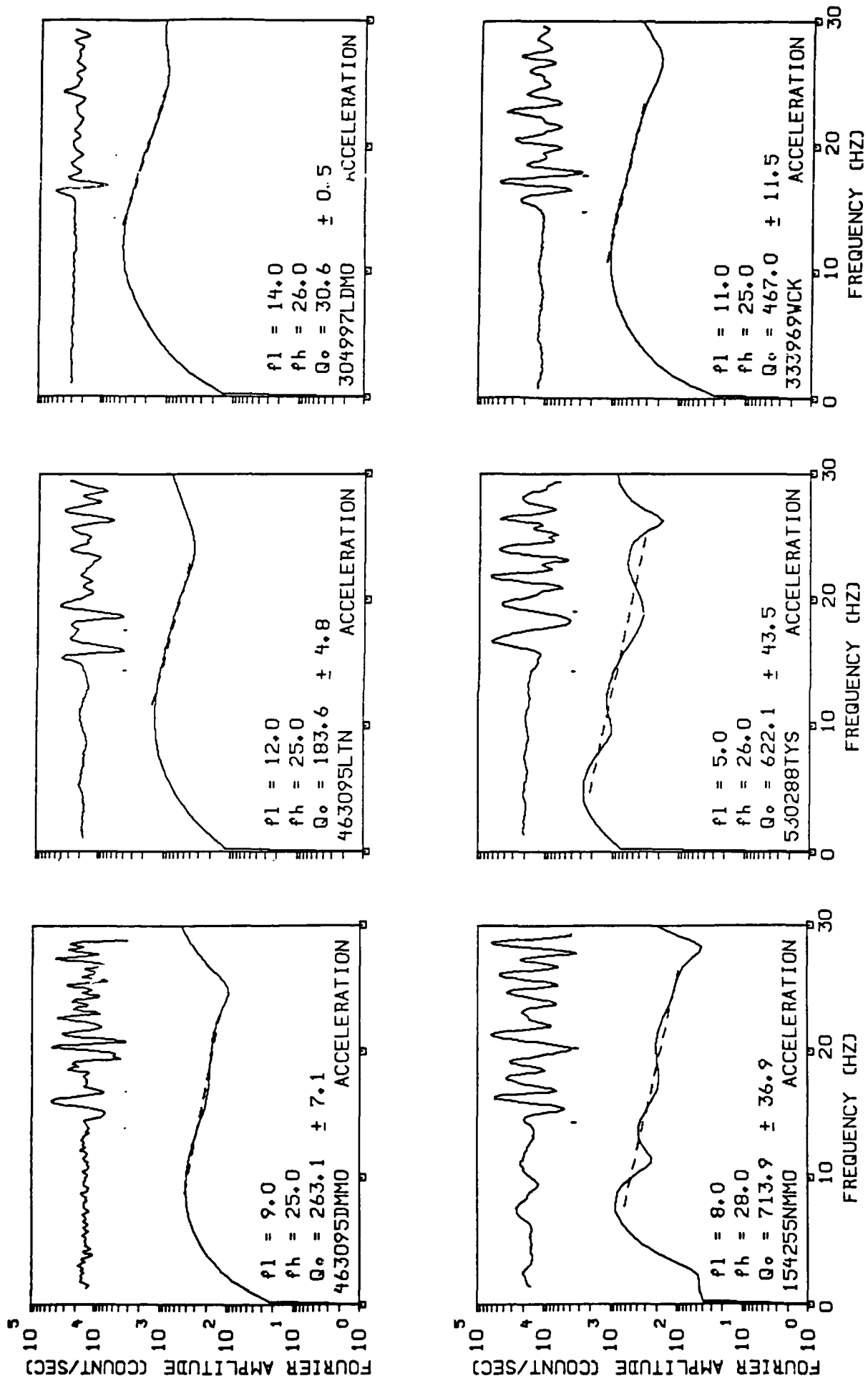


FIGURE 3

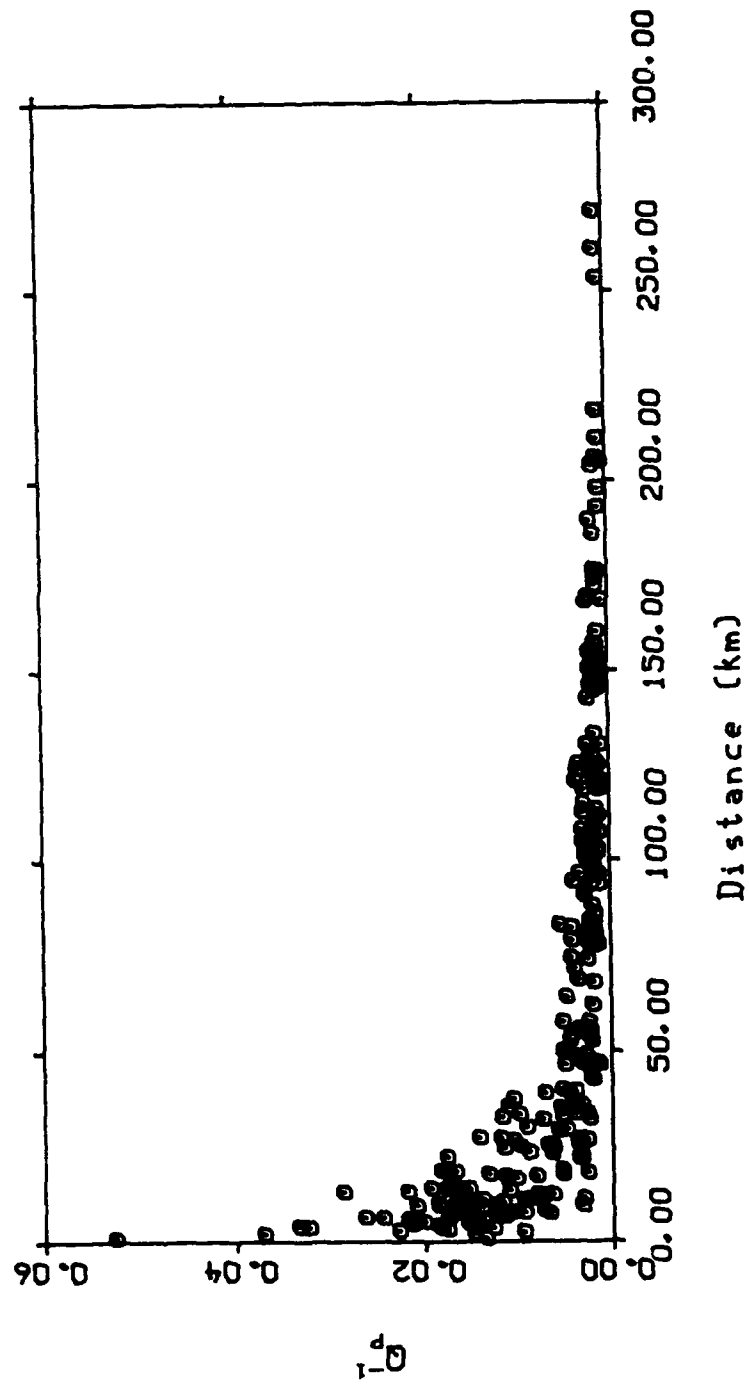


FIGURE 4

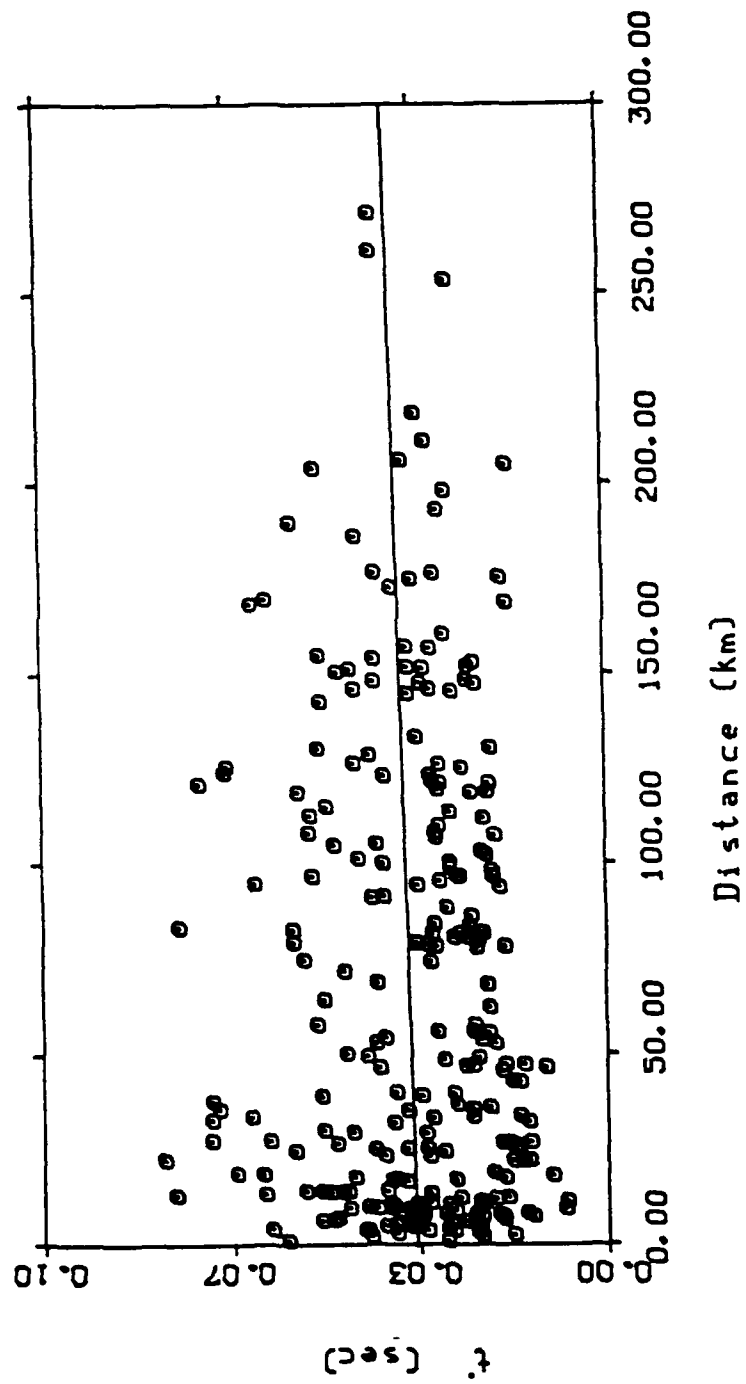


FIGURE 5

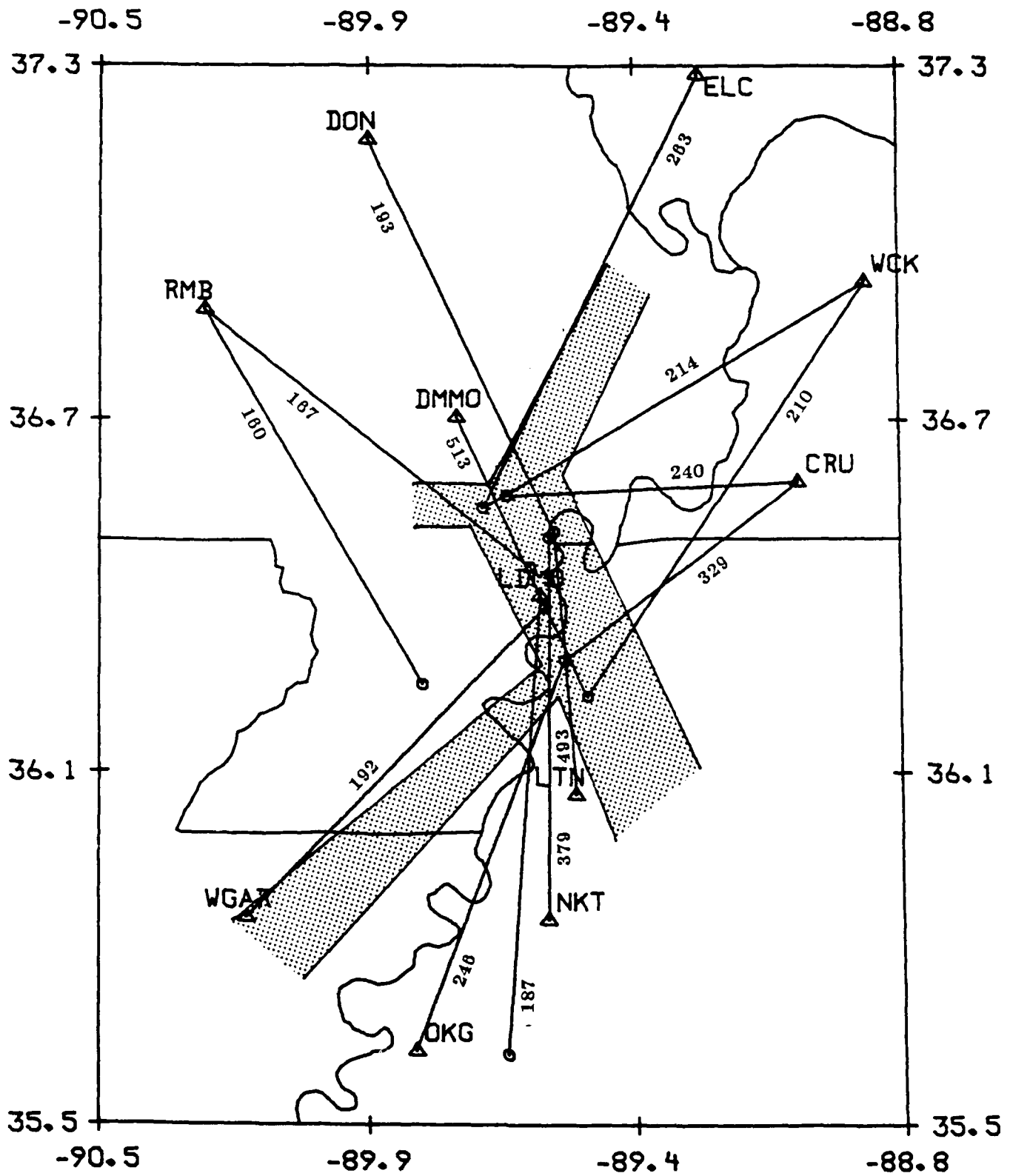


FIGURE 6

1 ▽				2 ▽				3 ▽			
1				$T_{1,2}$	2			3			$T_{3,3}$
4	5	$T_{1,5}$		$T_{1,6}$	6			8		$T_{3,9}$	9
10	$T_{1,10}$		$T_{1,11}$	12	$T_{2,12}$		$T_{2,13}$	14	$T_{3,14}$		15
	$T_{2,16}$										
16	$T_{3,16}$	$T_{2,17}$	17	18		19	$T_{3,20}$	20			21
		$T_{3,17}$					$T_{3,19}$				
				$T_{3,22}$				22			

FIGURE 7

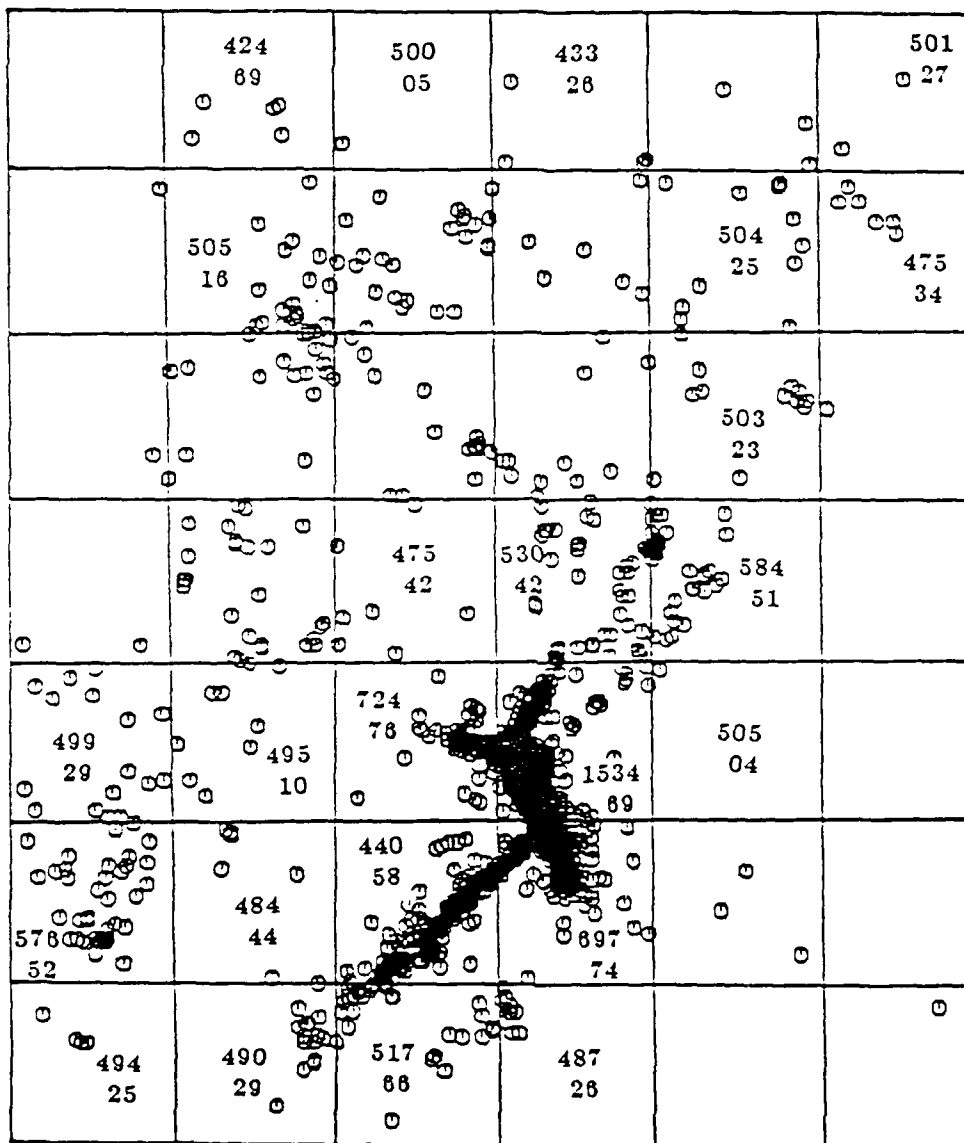


FIGURE 8a

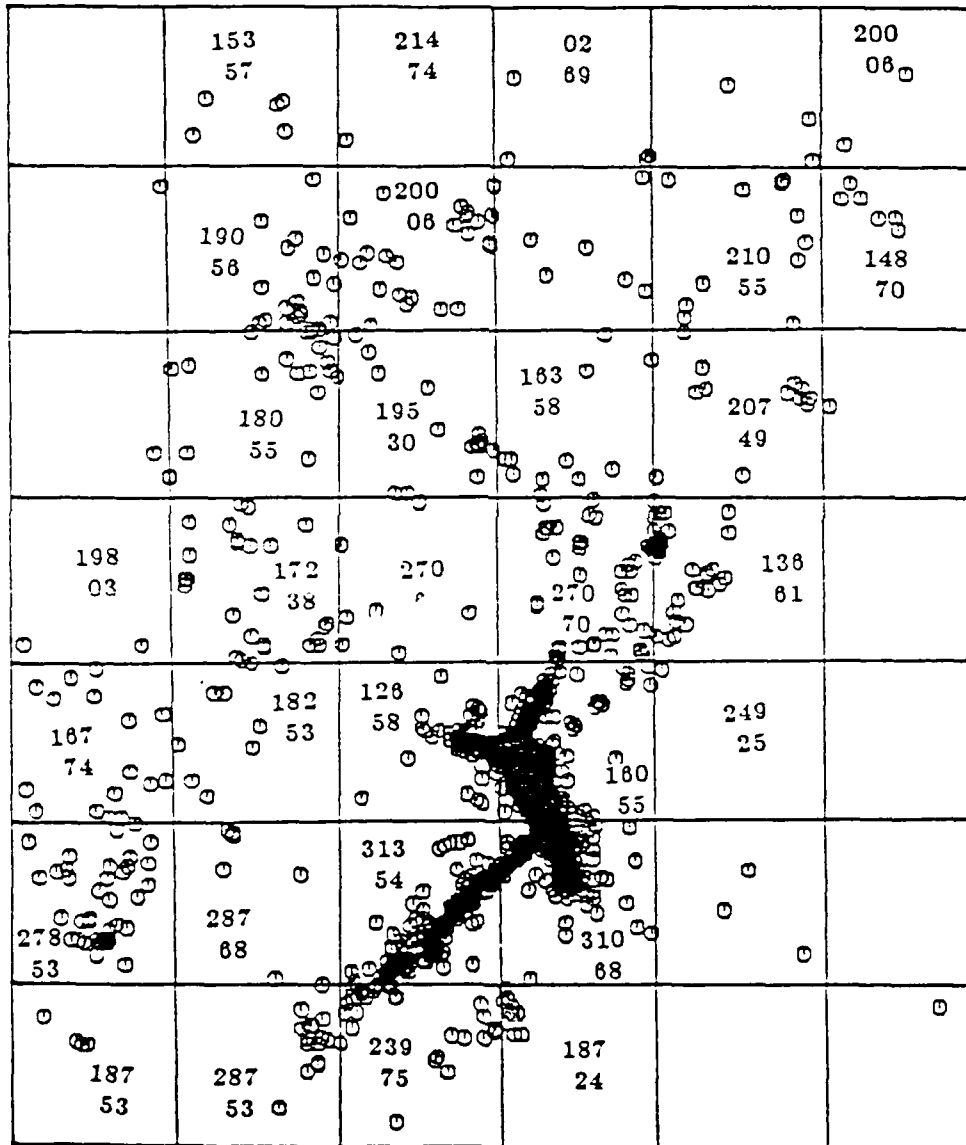


FIGURE 8b

-	6.03	6.23	6.26	6.19	6.18
-	6.28	6.49	6.52	6.45	6.44
-	6.00	6.13	6.21	6.20	5.15
-	6.25	6.39	6.47	6.46	6.41
-	6.02	6.03	6.06	5.89	-
-	6.27	6.28	6.32	6.14	-
-	5.90	6.03	6.03	5.95	-
-	6.14	6.28	6.28	6.20	-
6.09	5.97	5.88	5.78	5.97	-
6.34	6.21	6.12	6.02	6.22	-
6.08	5.95	5.79	5.98	6.08	-
6.33	6.20	6.39	6.23	6.33	-
6.04	6.02	6.00	6.15	6.04	-
6.29	6.27	6.24	6.41	6.29	-

FIGURE 9

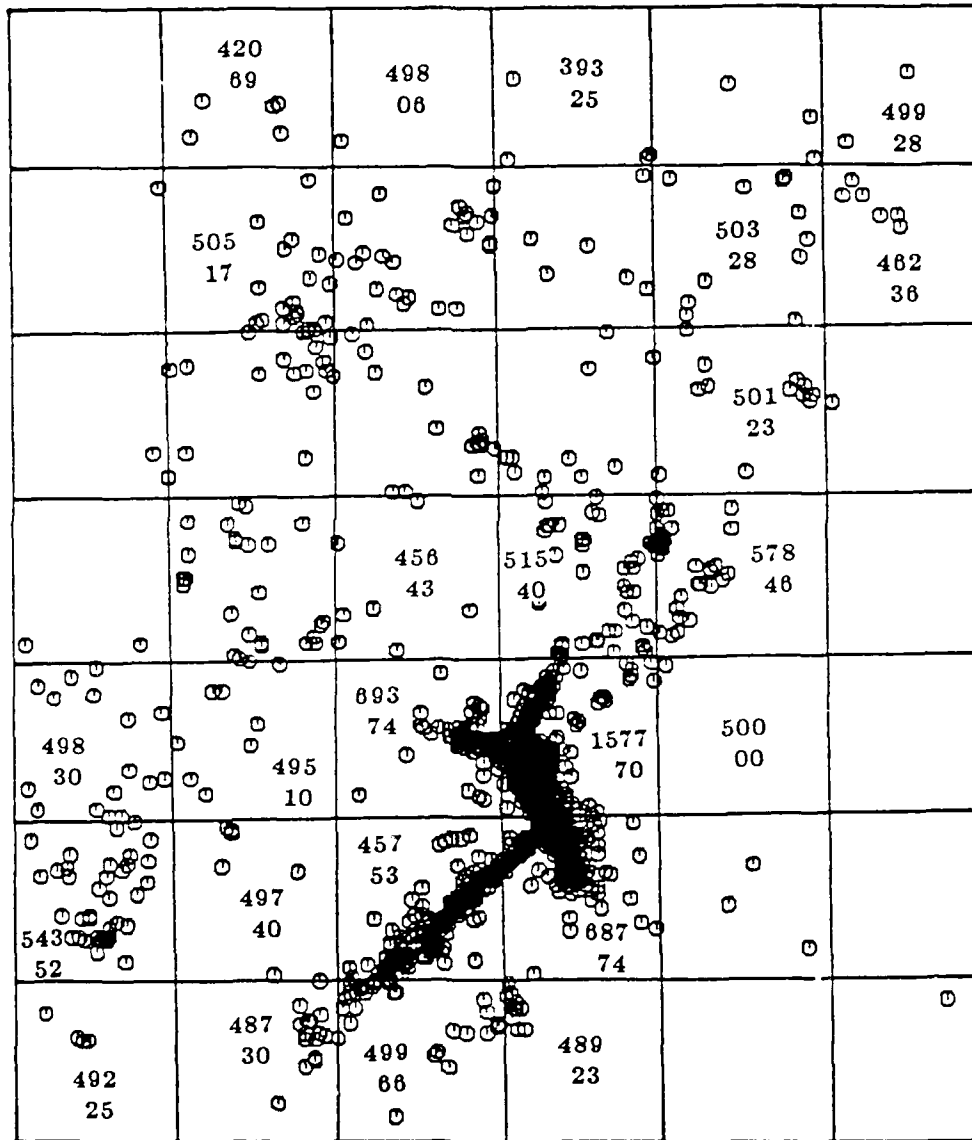


FIGURE 10

VI. ATTENUATIVE BODY WAVE DISPERSION AT LA Cerdanya (Eastern Pyrenees)

by

Antoni M. Correig (1), (3)
Brian J. Mitchell (2)

- (1) Laboratori d'Estudis Geofísics "Eduard Fontserè", Institut d'Estudis Catalans
- Facultat de Física, Martí Franques s/n. 08028 - Barcelona, Spain
- (2) Department of Earth and Atmospheric Sciences, Saint Louis University, 3507
Laclede, St. Louis, MO 63103, U.S.A.
- (3) DGDP - Geofísica, Facultat de Física, Universitat de Barcelona, Martí
Franques s/n. 08028 - Barcelona, Spain

ABSTRACT

Coda-Q for P- and S-waves has been measured from digitally recorded events occurring in the La Cerdanya region of the Eastern Pyrenees. Interpreted in terms of a power law, $Q(f) = Q_0 f^\eta$, Q-coda for P-waves is characterized by $Q_0 = 14$ and $\eta = 1.07$, and S-waves by $Q_0 = 14$ and $\eta = 1.13$. Using a generalization of a model due to Dainty (1981), we obtain a Q model for S-waves in which intrinsic Q is 23, the frequency dependence (ζ) of intrinsic Q is 1.17, and the turbidity factor is $5.1\text{E-}2$. Interpreted in terms of a continuous relaxation model, where Q_m is minimum Q and τ_1 and τ_2 are high- and low-frequency cutoffs, respectively, the values of the parameters are $Q_m = 5$ and $\tau_1 = 0.37$ when τ_2 is assumed to be 10.000. Body wave dispersion, as computed from the differences in arrival times of the wave filtered at 3, 6, 12 and 24 Hz relative to that at 6 Hz has been measured and found to range from 0.067 at 3 Hz to -0.075 at 24 Hz. This dispersion constrains τ_2 to be 43.

INTRODUCTION

In a previous paper (Correig *et al.*, 1988), first estimates of coda-Q values for S-waves were obtained from analog data registered at La Cerdanya Seismic Network. It was found that coda-Q values range between 17 and 120 at a frequency of 1.5 Hz, the lowest values occurring in the most seismically active regions. Coda-Q was also found to increase with increasing distance, a result indicative of decreasing seismic attenuation with increasing depth in the crust.

A digital recording system, designed for monitoring volcanic activity in the Antarctic (Ortiz *et al.*, 1987), was added to the analog system in 1986. One month of operation yielded 45 recordings from 15 events which were selected for analysis. Location parameters for those events appear in Table 1 and also in Figure 1, along with station designations and mapped faults. Absolute time was not

recorded, so that no origin time is given for the earthquakes. Because of the short duration of the recordings (16 sec), magnitudes could not be computed, although the analog data indicate that they range between 0 and 2. The data were recorded digitally at a rate of 64 samples/sec and the selected signals were band-pass filtered using 3-pole Butterworth filters with center frequencies of 1.5, 3, 6, 12 and 24 Hz and corresponding band-widths of 1, 2, 4, 8 and 16 Hz. The average peak-to-peak amplitudes were determined in consecutive 1-sec time windows at intervals of 0.25 sec.

In this paper we use the digital data to determine the contributions of intrinsic Q and scattering to the attenuation of P- and S-waves in the region of La Cerdanya. We use the notation of Mitchell (1989), which distinguishes between the frequency dependence of intrinsic Q (denoted by ζ) and apparent Q (denoted by η) which may refer to Q observed for Lg or various coda waves. We find that intrinsic Q is the dominating factor; thus it is possible to make several assumptions regarding the nature of scattering which have little effect on our results. We will determine a continuous relaxation model which explains the observed attenuation and dispersion of body waves in that region.

METHOD OF ANALYSIS

Because of the short recording times, only the earlier parts of the coda were used for both S-waves and P-waves. For this reason it was necessary to consider the source-receiver separation, a factor not necessary in the approach of Aki and Chouet (1975) where late coda was used. That separation is, however, included in the single scattering model developed by Sato (1977).

According to Sato's model, and following Correig *et al.* (1988), the reduced amplitude can be written

$$\ln[A(r, t, \omega) r K(\alpha)^{-1/2}] = \ln C(\omega) - bt/2 \quad (1)$$

where

$$b = \omega/Q_c. \quad (2)$$

$A(r, t, \omega)$ is the rms amplitude observed at a distance r and frequency ω , t is the lapse time, $C(\omega)$ is the source factor, and $K(\alpha)$ is defined by

$$K(\alpha) = \frac{1}{\alpha} \ln \frac{\alpha + 1}{\alpha - 1}$$

where $\alpha = t/t_0$ and t_0 is the arrival-time of the P-wave or S-wave under study.

Fitting the data to equation (1) by linear regression and using equation (2), Q_c values are obtained for P and S coda waves from filtered seismograms at each of several center frequencies. As a final step, the mean Q_c value obtained for the frequencies 1.5, 3, 6, 12 and 24 Hz were fit to the power law function

$$Q_c(f) = Q_0 f^\eta \quad (3)$$

where η indicates the frequency dependence of Q_c .

RESULTS

Figure 2 shows an example of fitting Equation (1) to the filtered data and S-wave filtered at a center frequency of 3 Hz. Table 2 shows the results obtained for Q_0 and η for both S-waves and P-waves, along with the correlation coefficient r^2 from the linear regression. Q_0 values are abnormally low and η values appear to be abnormally high. The Q_0 values for S-waves agree well with results previously obtained by Correig *et al.* (1988) from frequency master curves and the method of Sato (1977) for a frequency of 1.5 Hz.

Studies of coda usually report that coda-Q values vary with frequency. For short-period body-waves, for instance, Orcutt (1987) reports that Q increases with frequency. The low values obtained for P-wave coda-Q (Q_{cp}) and S-wave coda-Q (Q_{cs}) can be explained by the strongly inhomogeneous nature of the zone under study and by the small volume sampled by the coda. We computed the mean

semi-major axis of the ellipsoid sampled by the waves (Pulli, 1984) and found it to be about 15 km, so that the sampled region represents only the upper crust, which includes the seismogenic zone. Several estimates of the exponent η have been reported in, or can be inferred from, the literature. These include estimates of Scherbaum and Kisslinger (1985) where $Q_0 = 214$ and $\eta = 1.05$ for coda Q in the Adak seismic zone. Console and Rovelli (1981) where values of $Q_0 = 80$ and $\eta = 1.1$ were obtained from strong motion accelerogram spectra in Friuli. Peng *et al.* (1987) where η ranges between 1.06 and 1.33 in the Mammoth Lakes-Bishop area. van Eck (1988) where $Q_0 = 65$ and $\eta = 1.05$ were found for the Dead Sea Region. and Roecker *et al.* (1982) where η was found to vary and have values of 1.0 for depths less than 100 km, a value of 0.75 for depths to 400 km, and a value of 0.5 for depths to 1000 km in central Asia.

INTRINSIC Q FOR S-WAVES AND MEAN FREE PATH

Dainty (1981), using a single backscattering model and assuming that attenuation is mostly due to scattering, found that Q_c profiles for S-coda waves in the 1-30 Hz band satisfied

$$1/Q_c(\omega) = 1/Q_i + g*v/\omega \quad (4)$$

where Q_c stands for coda- Q , Q_i intrinsic Q of shear waves, v the shear velocity, and g the turbidity. The inverse of g is the mean-free path between scatterers, a constant taken to be independent of frequency, although this assumption could be replaced by the weaker assumption that g does not increase substantially between 1 Hz and 30 Hz. Dainty also assumed that Q_i is independent of frequency, but provided no theoretical reason to support that assumption.

We assume the validity of (4), but allow Q_i to be frequency-dependent or $Q_i = Q_i(f)$. Further, we assume that equation (4) holds for both S-coda and P-coda waves, by letting v be the velocity for either S waves or P waves. Hence, we

can write

$$1/Q_{cp,s}(\omega) = 1/Q_{ip,is}(\omega) + g^*v_{p,s}/\omega \quad (5)$$

where the subscripts p or s stand for P or S-waves. The turbidity g is independent of the propagating wave type so by assuming Q_{ip} proportional to Q_{is} , Equation (5) can be solved for Q_i and g . Following Anderson *et al.* (1965) and Minster (1980), we have assumed that $Q_{ip} = (9/4)Q_{is}$.

Solving for Q_{is} and g using (5) and the data of Table 2, we obtained the results in Table 3 where ζ refers to the frequency dependence of intrinsic Q . Q_{is} values in that table are slightly higher than the Q_o values of Table 2.

The entire process of obtaining Q_{is} and ζ by solving (5) was repeated by assuming $Q_{ip} = Q_{is}$ and $Q_{ip} = 3Q_{is}$. Results were nearly the same, with only slight changes in the value of Q_{is} , being 14 for the case $Q_{ip} = Q_{is}$ and 27 for the case $Q_{ip} = 3Q_{is}$. In all cases the value of ζ remains the same.

The values obtained for the turbidity g_o show a remarkably low dependence on frequency and are very consistent at the different stations. The observed values correspond to a mean free path of approximately 20 km. However, two interesting exceptions occur at stations URU and MON, located in the Cadi Mountains; for frequencies of 1.5 and 3 Hz the turbidity is found to be 0.12-0.13, corresponding to a mean-free-path of about 8 km. At the higher frequencies the mean free path is again about 20 km. This result may indicate that scattering is greater in the Cadi Mountains than in nearby regions at frequencies in the 1.5 - 3.0 Hz range.

In using (5) we have assumed that Q_c depends upon frequency as $Q_c^{-1} \propto f^{-n}$, where n is close to unity, and that attenuation due to scattering is proportional to f^{-1} . If this assumption is incorrect, solutions of (5) for intrinsic Q may contain large errors and results may not be reliable. The stability of the values for the turbidity factor, as predicted by the theory, however, suggest that

the results obtained for intrinsic-Q are correct and indicate that coda-Q is more representative of intrinsic Q than of scattering Q in the region of La Cerdanya. Other evidence in favor of this interpretation is the short duration of the coda (shorter than in surrounding areas), the small travel-time (a few seconds), the similarity in the values of coda-Q for P- and S-waves (Clements, 1982), and the frequency content of the coda where lower frequencies have greater lapse-times (Richards and Menke, 1983). Although we believe that coda Q is indeed representative of intrinsic Q in this region, that result is not crucial for the remainder of this paper.

We interpreted the intrinsic Q values obtained for S-waves in terms of a continuous relaxation model (CRM) as described by Ben-Menahem and Singh (1981). Because the interpretation of Q in terms of relaxation phenomena is phenomenological, it can be carried out for the case of intrinsic Q as well as for apparent Q.

For a CRM the specific dissipation function Q^{-1} satisfies the relation (Liu *et al.*, 1976)

$$Q^{-1}(\omega) = \frac{2}{\pi Q_m} \tan^{-1} \left[\frac{\omega(s_2 - s_1)}{\omega^2 + s_1 s_2} \right] \quad (6)$$

where ω is frequency, s_1 and s_2 are the high- and low-frequency cutoffs, respectively, and Q_m is a constant which defines the flat part of the Q-spectrum. Q^{-1} varies as ω at the low-frequency limit and as ω^{-1} at the high frequency limit. In the present study the deduced Q values lie on the high-frequency limit. The relaxation times of the absorption band are defined as $\tau_1 = 1/s_1$ and $\tau_2 = 1/s_2$. We obtained values of Q_m and τ_2 by trial and error which minimize

$$\sum |Q_{pr} - Q_o|^2 \quad (7)$$

where Q_{pr} is the predicted Q value from (6) and Q_o is the measured value. τ_1 was assigned an arbitrary value of 10,000 (Minster, 1980).

The best fit corresponds to $\tau_2 = 0.37$ s and $Q_m = 5$. It should be noted

that the best fit to the model was found by looking at the lowest residual obtained by varying the parameter τ_2 for a given Q_m . Starting with a value of Q_m of $1E + 4$ and varying τ_2 from $1E - 4$ to $1E + 4$, the process converged to the Q_m and τ_2 values given above. Lower values of Q_m , along with higher values of τ_2 , also produced fits to the model, but with no improvement in the residual. We have chosen the highest value obtained for Q_m along with the corresponding τ_2 value to be representative of the crust in the La Cerdanya region. Figure 3 shows the fit of the observed data to the CRM.

BODY WAVE DISPERSION

It is well known (see, for example, Ben-Menahem and Singh, 1981) that in an attenuating medium body waves must be dispersive in order to satisfy causality. Attenuation and dispersion are related through the Kramers-Kronig relations. Dispersion of body waves have been measured and correctly predicted from anelasticity through the Kramers-Kronig relations by Wuenschel (1965), Doornbos (1983), Jacobson (1987) and McLaughlin and Anderson (1987). We attempted to determine whether such dispersion of body waves could be measured from the data registered at La Cerdanya. The seismograms were filtered at center-frequencies of 1.5, 3, 6, 12 and 24 Hz and the arrival times were read for each filtered seismogram. The arrival-times of the filtered signals were obtained relative to that of the signal filtered at 6 Hz. Figure 4 shows an example of this process. The signals filtered at 12 and 24 Hz are clearly advanced relative to the signal at 6 Hz, whereas signals filtered at 3 and 1.5 Hz are clearly delayed. All readings were corrected for the group delays of the instrument and the Butterworth filter (Claerbout, 1976; Seidl and Stammer, 1984; Vila, 1988). Corner frequencies of the spectra are located between 25 and 30 Hz, so that no corrections are needed for the source-time function. Results for a travel time of 2.5 ± 0.5 s are presented in Table 4. The negative value of the corrected data for 1.5 Hz that appears in

Table 4 may be due either to the large value of the group delay at this frequency, which occurs because this frequency (1.5 Hz) is very close to the resonant frequency of the geophone (1 Hz), or because of the difficulty in reading the arrival time at this frequency, due to a low signal-to-noise ratio. In view of this uncertainty, we have not included the dispersion at 1.5 Hz in our results.

We attempted to determine if the P-wave dispersion which we measured is consistent with that predicted by the model derived earlier. Doornbos (1983) proposed, as a measure of the dispersion, the following form of the Kramers-Kronig relation

$$D(\omega) = \frac{C_\infty}{C(\omega)} - 1 \quad (8)$$

where C_∞ and $C(\omega)$ are the phase velocities at infinity frequency and at frequency ω , respectively. To adapt the above definition (as a function of phase velocity) to our measurements (as a function of travel time) we substituted $C_\infty = x/t_u$ and $C(\omega) = x/t(\omega)$, where x is distance, t_u is the travel time of the unfiltered signal, and $t(\omega)$ is the travel time of the filtered signal at frequency ω . Although, strictly speaking, travel time is related to group velocity, the use of phase velocity instead of group velocity is justified because for $\omega \rightarrow \infty$, $C(\omega) \rightarrow U(\omega)$ and $C^{-1}(\omega) \approx U^{-1}(\omega)$. We computed both phase and group velocities as a function of frequency for an absorption-band model and found them to differ at most by 0.018 s. Hence equation (8) can be rewritten as

$$D(\omega) = \frac{t(\omega) - t_u}{t_u} \quad (9)$$

from which $t(\omega)$ can be computed if $C_\infty/C(\omega)$ is known, and $(t(f) - t(6 \text{ Hz}))$ can be directly compared with our data. $C_\infty/C(\omega)$ is given by Ben-Menahem and Singh (1981) as

$$\frac{C_\infty}{C(\omega)} = \frac{1}{2\pi Q_m} \ln \frac{\omega^2 + s_2^2}{\omega^2 + s_1^2} + 1 \quad (10)$$

$t(\omega)$ was computed from (9) at frequencies of 1.5, 3, 6, 12 and 24 Hz for the model parameters previously found ($Q_m = 5$ and $\tau_2 = 0.37$) and the travel-time difference $t(f) - t(6 \text{ Hz})$ was obtained for each frequency. The agreement is reasonably good at low frequencies as shown by Figure 5 (dashed line), but diverges at higher frequencies. In an attempt to get a better fit, $t(f) - t(6 \text{ Hz})$ was recomputed for different values of τ_1 and a τ_1 value of 43 was found to provide a good fit to the data at all frequencies as shown by the solid line in Figure 5. It thus appears that if data on body wave dispersion are available along with a Q model, the three parameters that define a continuous relaxation model can be well constrained.

Note that the use of the Kramers-Kronig relations make no distinction between intrinsic and coda Q , so that the apparent Q and body-wave dispersion values can be used instead of intrinsic Q and body-wave dispersion.

CONCLUSIONS

Coda- Q values for P- and S-waves were determined at La Cerdanya at frequencies between 1.5 and 25 Hz. The turbidity coefficients and frequency-dependent values for intrinsic Q_s were obtained through a generalization of Dainty's model in which intrinsic Q was allowed to vary with frequency. The Q_s values were interpreted in terms of a continuous relaxation model which can explain the low-frequency data if $Q_m = 5$ and the relaxation time corresponding to the high-frequency cutoff is 0.37. Body-wave dispersion, computed as differences of the arrival times of the wave filtered at several frequencies relative to a reference frequency, allows the determination of the relaxation time for the low-frequency cutoff for the relaxation models and leads to the value $\tau_2 = 43$. Thus, a combination of observed attenuation and observed body-wave dispersion permits a complete description of the relaxation model which describes intrinsic

attenuation in the region of La Cerdanya.

ACKNOWLEDGEMENTS

Roel Snieder and Anton Dainty critically read the manuscript and contributed helpful suggestions. Ramon Ortiz designed and built the digital system which recorded the events. This research has been partially supported by the U.S. - Spain Joint Committee for Scientific and Technological Cooperation under grant CCB-8504007, by the Comision Asesora para la Inivestigacion Cientifica y Tecnica under grant 1666, and by the Advanced Research Projects Agency of the U.S. Department of Defense, and was monitored by the Air Force Geophysics Laboratory under Contract F19628-87-K-0036.

REFERENCES

- Aki, K. and B. Chouet (1975). Origin of coda waves: source, attenuation and scattering effects, *J. Geophys. Res.* **80**, 3322-3342.
- Anderson, D.L., A. Ben-Menahem, and C.B. Archambeau (1965). Attenuation of seismic energy in the upper mantle, *J. Geophys. Res.* **70**, 1441-1448.
- Ben-Menahem, A. and J.S. Singh (1981). *Seismic waves and sources*, Springer-Verlag, New York.
- Claerbout, J.F. (1976). *Fundamentals of Geophysical Data Processing*, McGraw-Hill.
- Clements, J. (1982). Intrinsic Q and its frequency dependence, *Phys. Earth Planet. Int.* **27**, 286-299.
- Console, R. and A. Rovelli (1981). Attenuation parameters for Friuli region from strong-motion accelerogram spectra, *Bull. Seism. Soc. Am.* **71**, 1981-1991.
- Correig, A.M., B.J. Mitchell and R. Ortiz (1988). Seismicity and coda Q values in the eastern Pyrenees: First results from the La Cerdanya Seismic Network, *PAGEOPH*, in press.
- Dainty, A.M. (1981). A scattering model to explain seismic Q observations in the lithosphere between 1 and 30 Hz, *Geophys. Res. Let.* **81**, 1126-1128.
- Doornbos, D.J. (1983). Observable effects of the seismic absorption band in the Earth, *Geophys. J.R. astr. Soc.* **75**, 693-711.
- van Eck, T. (1988). Attenuation of coda waves in the Dead Sea region, *Bull. Seism. Soc. Am.* **78**, 770-779.

- Herraiz, M. and A.F. Espinosa (1986). Scattering and attenuation of high-frequency seismic waves: Development of the theory of coda waves, *U.S. Geological Survey Open-File Report 86-455*.
- Herraiz, M. and A.F. Espinosa (1987). Coda waves: A review, *PAGEOPH* **125**, 499-577.
- Jacobson, R.S. (1987). An investigation into the fundamental relationships between attenuation, phase dispersion, and frequency using seismic refraction profiles over sedimentary structures, *Geophysics* **52**, 72-87.
- Liu, H.P., D.L. Anderson and H. Kanamori (1976). Velocity dispersion due to anelasticity; implications for seismology and mantle composition, *Geophys. J.R. astr. Soc.* **47**, 41-58.
- McLaughlin, K.L. and L.M. Anderson (1987). Stochastic dispersion of short-period P-waves due to scattering and multipathing, *Geophys. J.R. astr. Soc.* **89**, 933-964.
- Minster, J.B. (1980). Anelasticity and attenuation, in Dziewonski, A.M. and E. Boschi (eds.), *Physics of the Earth's Interior*, 152-212.
- Mitchell, B.J. (1989). Frequency dependence of Q_{Lg} and Q_{β} in the continental crust, *Geophys. Res. Lett.*, submitted.
- Orcutt, J.A. (1987). Structure of the Earth's Oceanic Crust and Uppermost Mantle, *Rev. of Geophys.* **25**, 1177-1196.
- Ortiz, R., A. Garcia and E. Gimenez (1987). Desarrollo de instrumentacion geofisica para su operacion en condiciones antarticas, *Actas del Segundo Symposium Espanol de Estudios Antarticos*, Madrid, 13-15 Julio 1987, CSIC, 197-

TABLE 1

EARTHQUAKE LOCATIONS

<u>EVENT #</u>	<u>LATITUDE</u>	<u>LONGITUDE</u>	<u>DEPTH</u>
1	42.397	1.945	13.7
2	42.474	1.673	11.6
3	42.398	1.938	13.1
4	42.627	1.861	2.0
5	42.265	1.775	2.8
6	42.217	1.797	2.0
7	42.379	1.9	13.3
8	42.278	1.975	0.1
9	42.379	1.77	2.1
10	42.387	1.78	1.2
11	42.406	1.843	11.5
12	42.335	2.095	2.1
13	42.389	1.628	9.5
14	42.406	1.764	2.3
15	42.365	1.65	2.2

TABLE 2

POWER LAW FIT OF Q_c

Station	Q_0	S-waves	r^2	Q_0	P-waves	r^2
		η			η	
LVA	11 ± 1.3	1.21 ± 0.13	0.90	16 ± 1.4	1.00 ± 0.15	0.82
LES	14 ± 1.4	1.13 ± 0.15	0.89	10 ± 1.5	1.13 ± 0.20	0.86
URU	15 ± 1.3	1.21 ± 0.14	0.87	20 ± 1.7	1.02 ± 0.24	0.77
MON	14 ± 1.3	1.18 ± 0.13	0.90	12 ± 1.8	1.13 ± 0.28	0.86
ALL	14 ± 1.2	1.13 ± 0.08	0.95	14 ± 1.3	1.07 ± 0.14	0.95

TABLE 3

VALUES OBTAINED FOR g AND Q_{is}

Station	$g \times 10^{-2}$	Q_{is}	ζ	r^2
LVA	4.79 ± 0.22	15 ± 2.5	1.38 ± 0.46	0.99
LES	6.22 ± 0.56	30 ± 2.5	1.04 ± 0.46	0.99
ALL	5.10 ± 0.35	23 ± 2.5	1.17 ± 0.46	0.99

TABLE 4

P-wave dispersion for a travel time of 2.5 ± 0.5 s relative to the arrival-time of 6 Hz waves. The data in column 3 have been corrected for responses of the instrument and Butterworth filter.

Frequency (Hz)	Uncorrected Data	Corrected Data
1.5	0.225 ± 0.060	-0.045
3	0.133 ± 0.044	0.058
6	0.000	0.000
12	-0.071 ± -0.018	-0.044
24	-0.113 ± 0.029	-0.073

FIGURE CAPTIONS

Figure 1. Location of the seismic stations (LVA, URU, MON, LES) and the events used in this study. Broken lines represent faults.

Figure 2. Example of an exponential fit of the data to equation (1) for obtaining Q_c for the case of S-coda at 3 Hz.

Figure 3. Fit of the Q -values to the continuous relaxation model with $Q_m = 5$, $\tau_2 = 0.37$ and an assumed value of $\tau_1 = 10,000$.

Figure 4. Example of the process of measurement of P-wave dispersion. The wave has been band-pass filtered at 1.5, 3, 6, 12 and 24 Hz. The vertical line indicates the arrival time of the signal filtered at 6 Hz. The signals filtered at 12 and 24 Hz are advanced with respect to that of 6 Hz, and the signals filtered at 3 and 1.5 Hz are delayed. The arrival times have been corrected for the instrument response and Butterworth filter group delay.

Figure 5. Observed arrival times relative to those at 6 Hz (symbols) compared with values predicted for the continuous relaxation model when $\tau_1 = 43$ (solid line) and $\tau_1 = 10,000$ (dashed line). In both cases $Q_n = 5$ and $\tau_2 = 0.37$

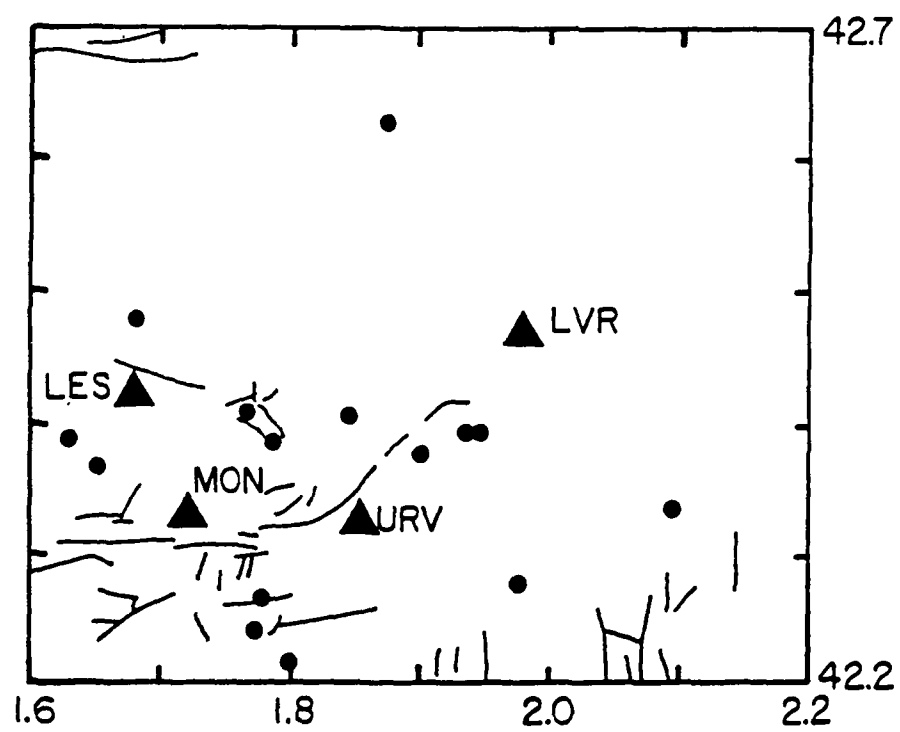


Figure 1

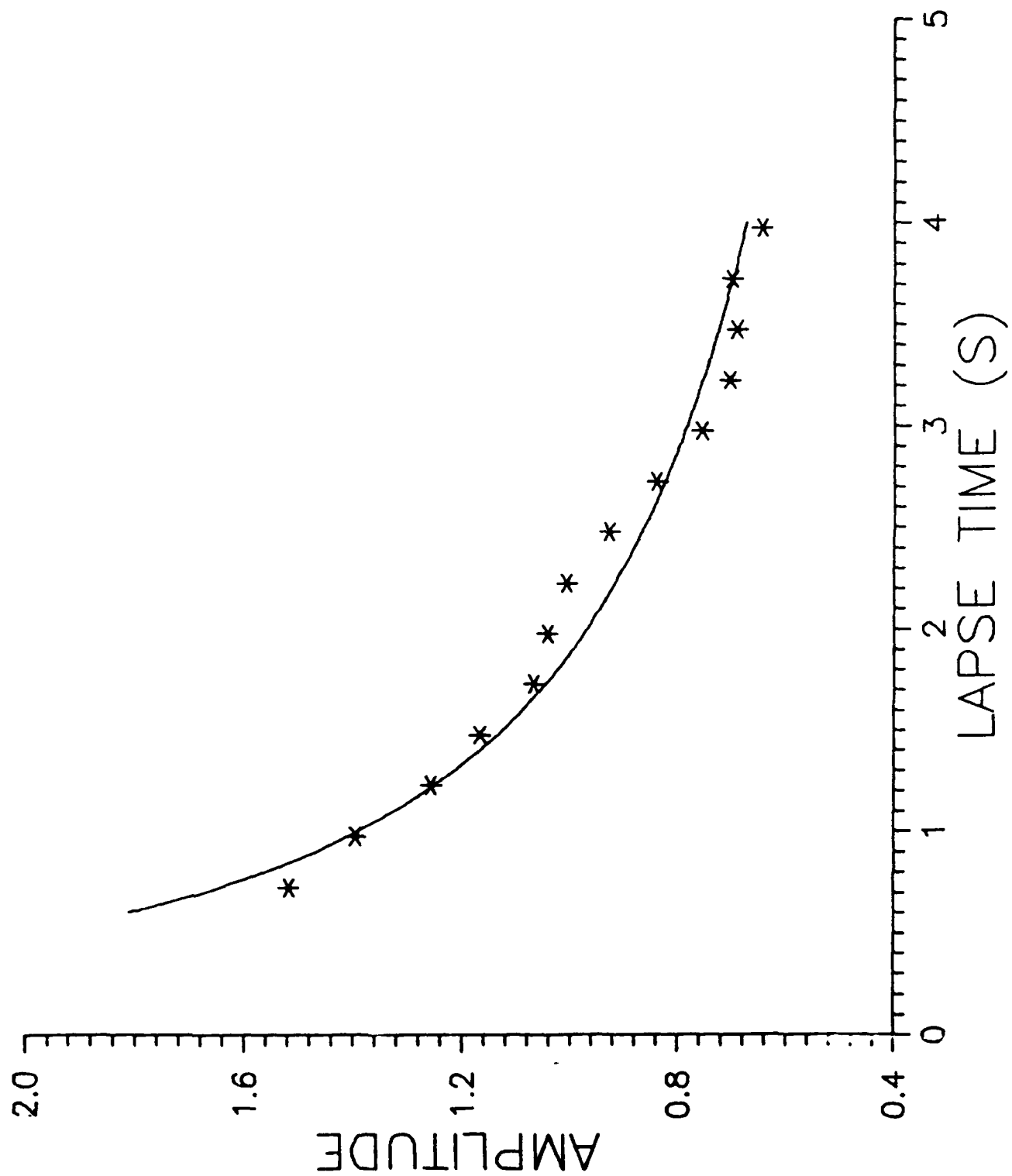


FIGURE 2

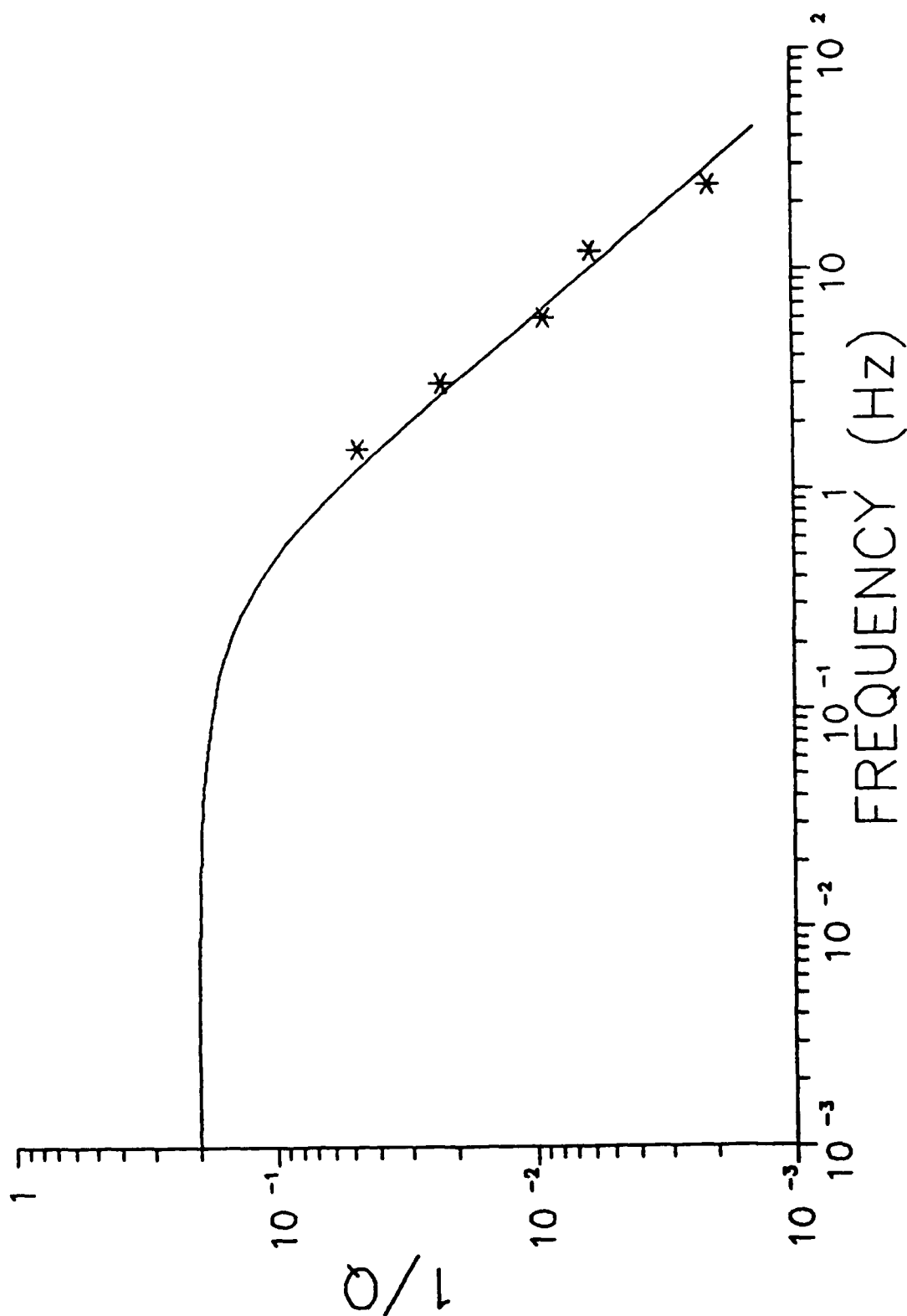


FIGURE 3

CERDANYA NETWORK CA7051

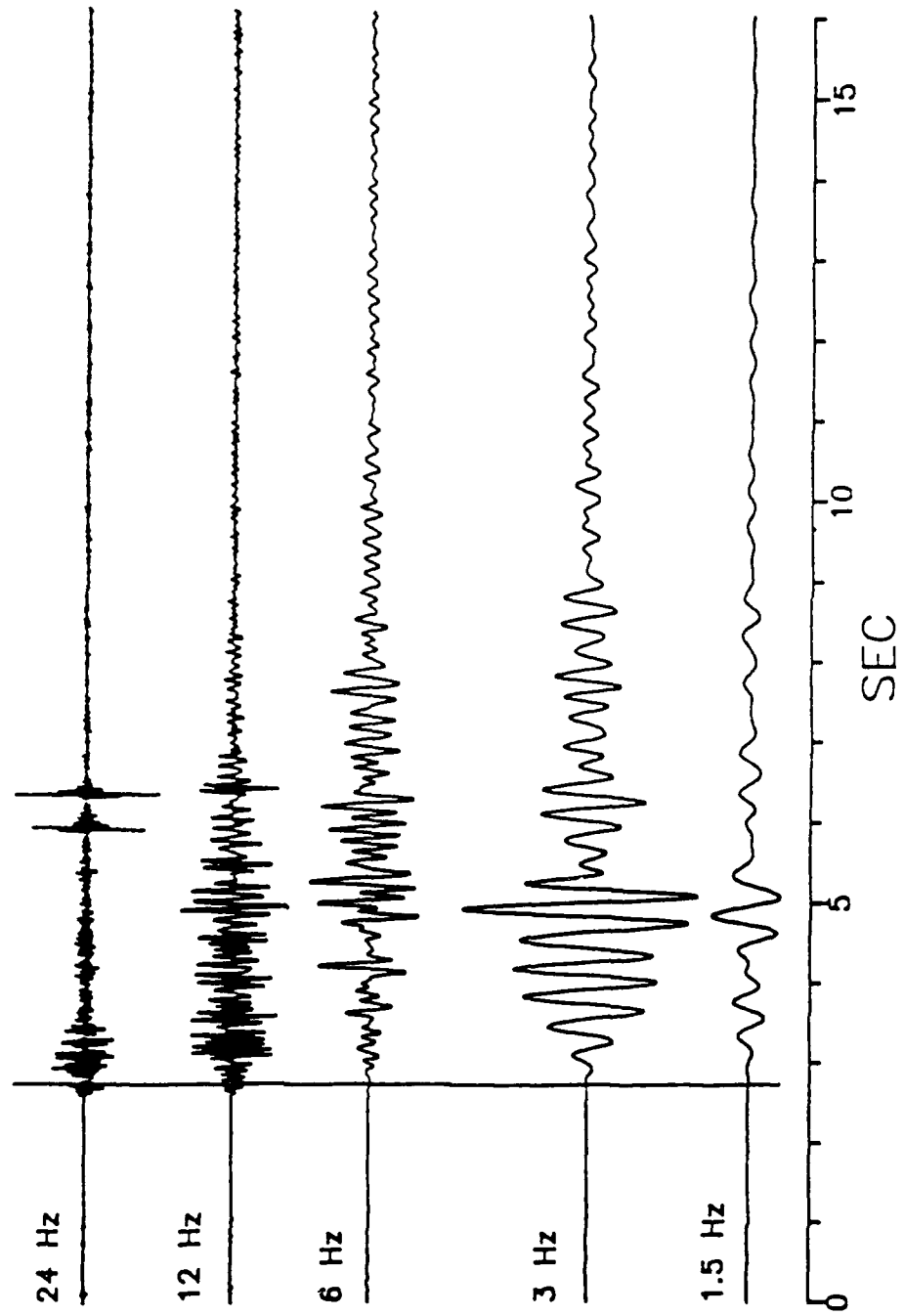


Figure 4

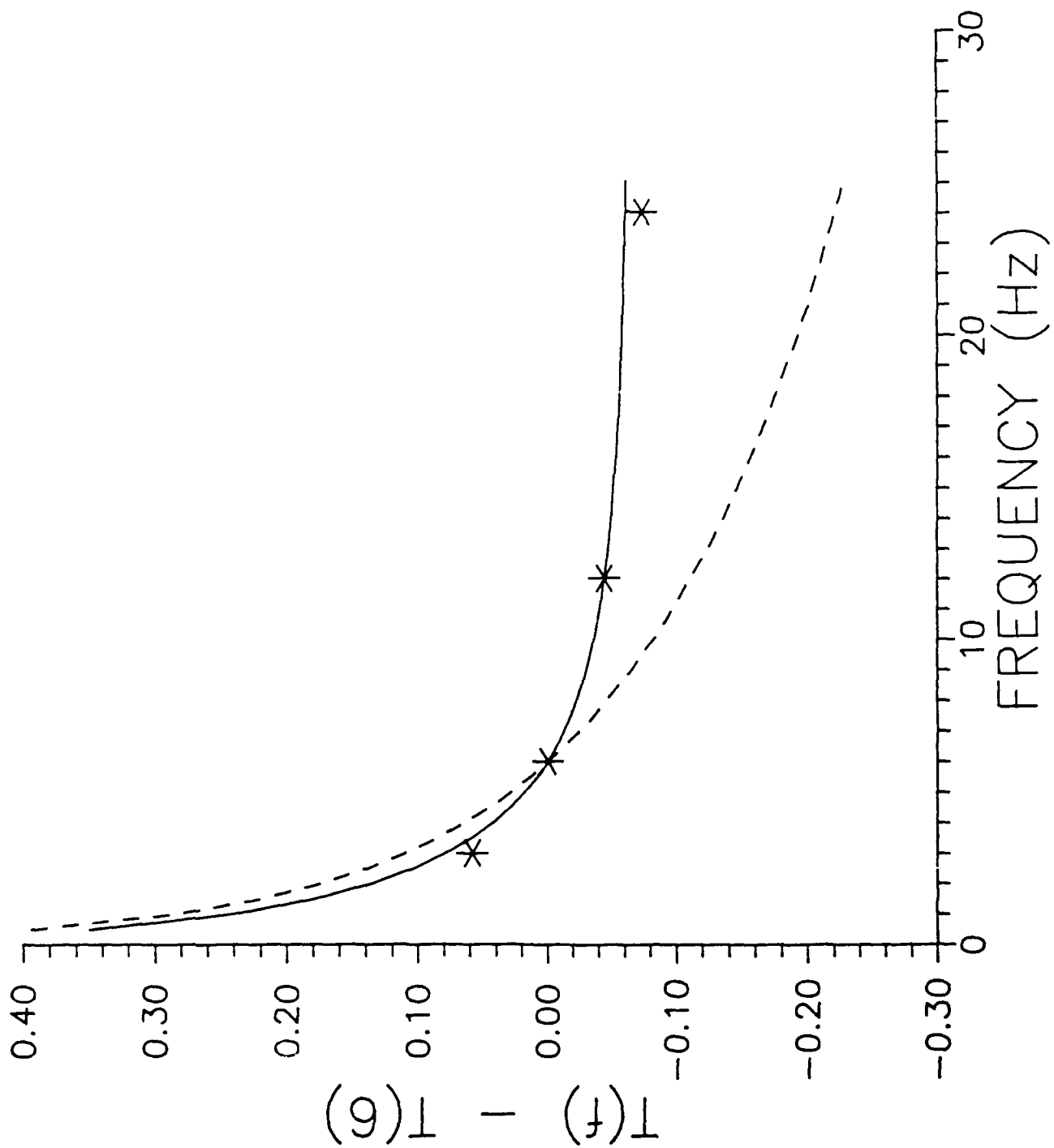


FIGURE 5

CONTRACTORS (United States)

Professor Keiiti Aki
Center for Earth Sciences
University of Southern California
University Park
Los Angeles, CA 90089-0741

Professor Thomas Ahrens
Seismological Lab, 252-21
Div. of Geological and Planetary
Sciences
California Institute of Technology
Pasadena, CA 91125

Professor Charles B. Archambeau
Cooperative Institute for Resch
in Environmental Sciences
University of Colorado
Boulder, CO 80309

Dr. Thomas C. Bache Jr.
Science Applications Int'l Corp.
10210 Campus Point Drive
San Diego, CA 92121 (2 copies)

Dr. Muawia Barazangi
Institute for the Study of
of the Continent
Cornell University
Ithaca, NY 14853

Dr. Douglas R. Baumgardt
Signal Analysis & Systems Div.
ENSCO, Inc.
5400 Port Royal Road
Springfield, VA 22151-2388

Dr. Jonathan Berger
Institute of Geophysics and
Planetary Physics
Scripps Institution of Oceanography
A-025
University of California, San Diego
La Jolla, CA 92093

Dr. S. Bratt
Science Applications Int'l Corp.
10210 Campus Point Drive
San Diego, CA 92121

Dr. Lawrence J. Burdick
Woodward-Clyde Consultants
P.O. Box 93245
Pasadena, CA 91109-3245 (2 copies)

Professor Robert W. Clayton
Seismological Laboratory/Div. of
Geological & Planetary Sciences
California Institute of Technology
Pasadena, CA 91125

Dr Karl Coyner
New England Research, Inc.
76 Olcott Drive
White River Junction, VT 05001

Dr. Vernon F. Cormier
Department of Geology & Geophysics
U-45, Room 207
The University of Connecticut
Storrs, Connecticut 06268

Dr. Steven Day
Dept. of Geological Sciences
San Diego State U.
San Diego, CA 92182

Dr. Zoltan A. Der
ENSCO, Inc.
5400 Port Royal Road
Springfield, VA 22151-2388

Professor John Ferguson
Center for Lithospheric Studies
The University of Texas at Dallas
P.O. Box 830688
Richardson, TX 75083-0688

Professor Stanley Flatte'
Applied Sciences Building
University of California,
Santa Cruz, CA 95064

Dr. Alexander Florence
SRI International
333 Ravenswood Avenue
Menlo Park, CA 94025-3493

Professor Steven Grand
University of Texas at Austin
Dept of Geological Sciences
Austin, TX 78713-7909

Dr. Henry L. Gray
Associate Dean of Dedman College
Department of Statistical Sciences
Southern Methodist University
Dallas, TX 75275

Professor Roy Greenfield
Geosciences Department
403 Deike Building
The Pennsylvania State University
University Park, PA 16802

Professor David G. Harkrider
Seismological Laboratory
Div of Geological & Planetary Sciences
California Institute of Technology
Pasadena, CA 91125

Professor Donald V. Helmberger
Seismological Laboratory
Div of Geological & Planetary Sciences
California Institute of Technology
Pasadena, CA 91125

Professor Eugene Herrin
Institute for the Study of Earth
and Man/Geophysical Laboratory
Southern Methodist University
Dallas, TX 75275

Professor Robert B. Herrmann
Department of Earth & Atmospheric
Sciences
Saint Louis University
Saint Louis, MO 63156

Professor Bryan Isacks
Cornell University
Dept of Geological Sciences
SNEE Hall
Ithaca, NY 14850

Professor Lane R. Johnson
Seismographic Station
University of California
Berkeley, CA 94720

Professor Thomas H. Jordan
Department of Earth, Atmospheric
and Planetary Sciences
Mass Institute of Technology
Cambridge, MA 02139

Dr. Alan Kafka
Department of Geology &
Geophysics
Boston College
Chestnut Hill, MA 02167

Professor Leon Knopoff
University of California
Institute of Geophysics
& Planetary Physics
Los Angeles, CA 90024

Professor Charles A. Langston
Geosciences Department
403 Deike Building
The Pennsylvania State University
University Park, PA 16802

Professor Thorne Lay
Department of Geological Sciences
1006 C.C. Little Building
University of Michigan
Ann Arbor, MI 48109-1063

Dr. Randolph Martin III
New England Research, Inc.
76 Olcott Drive
White River Junction, VT 05001

Dr. Gary McCartor
Mission Research Corp.
735 State Street
P.O. Drawer 719
Santa Barbara, CA 93102 (2 copies)

Professor Thomas V. McEvilly
Seismographic Station
University of California
Berkeley, CA 94720

Dr. Keith L. McLaughlin
S-CUBED,
A Division of Maxwell Laboratory
P.O. Box 1620
La Jolla, CA 92038-1620

Professor William Menke
Lamont-Doherty Geological Observatory
of Columbia University
Palisades, NY 10964

Professor Brian J. Mitchell
Department of Earth & Atmospheric
Sciences
Saint Louis University
Saint Louis, MO 63156

Mr. Jack Murphy
S-CUBED
A Division of Maxwell Laboratory
11800 Sunrise Valley Drive
Suite 1212
Reston, VA 22091 (2 copies)

Professor J. A. Orcutt
IGPP, A-205
Scripps Institute of Oceanography
Univ. of California, San Diego
La Jolla, CA 92093

Professor Keith Priestley
University of Nevada
Mackay School of Mines
Reno, NV 89557

Professor Paul G. Richards
Lamont-Doherty Geological
Observatory of Columbia Univ.
Palisades, NY 10964

Wilmer Rivers
Teledyne Geotech
314 Montgomery Street
Alexandria, VA 22314

Dr. Alan S. Ryall, Jr.
Center of Seismic Studies
1300 North 17th Street
Suite 1450
Arlington, VA 22209-2308 (4 copies)

Professor Charles G. Sammis
Center for Earth Sciences
University of Southern California
University Park
Los Angeles, CA 90089-0741

Professor Christopher H. Scholz
Geological Sciences
Lamont-Doherty Geological Observatory
Palisades, NY 10964

Dr. Jeffrey L. Stevens
S-CUBED,
A Division of Maxwell Laboratory
P.O. Box 1620
La Jolla, CA 92038-1620

Professor Brian Stump
Institute for the Study of Earth & Man
Geophysical Laboratory
Southern Methodist University
Dallas, TX 75275

Professor Ta-liang Teng
Center for Earth Sciences
University of Southern California
University Park
Los Angeles, CA 90089-0741

Dr. Clifford Thurber
State University of New York at
Stony Brooks
Dept of Earth and Space Sciences
Stony Brook, NY 11794-2100

Professor M. Nafi Toksoz
Earth Resources Lab
Dept of Earth, Atmospheric and
Planetary Sciences
Massachusetts Institute of Technology
42 Carleton Street
Cambridge, MA 02142

Professor Terry C. Wallace
Department of Geosciences
Building #77
University of Arizona
Tucson, AZ 85721

Weidlinger Associates
ATTN: Dr. Gregory Wojcik
4410 El Camino Real, Suite 110
Los Altos, CA 94022

Professor Francis T. Wu
Department of Geological Sciences
State University of New York
at Binghamton
Vestal, NY 13901

OTHERS (United States)

Dr. Monem Abdel-Gawad
Rockwell Internat'l Science Center
1049 Camino Dos Rios
Thousand Oaks, CA 91360

Professor Shelton S. Alexander
Geosciences Department
403 Deike Building
The Pennsylvania State University
University Park, PA 16802

Dr. Ralph Archuleta
Department of Geological
Sciences
Univ. of California at
Santa Barbara
Santa Barbara, CA

J. Barker
Department of Geological Sciences
State University of New York
at Binghamton
Vestal, NY 13901

Mr. William J. Best
907 Westwood Drive
Vienna, VA 22180

Dr. N. Biswas
Geophysical Institute
University of Alaska
Fairbanks, AK 99701

Dr. G. A. Bollinger
Department of Geological Sciences
Virginia Polytechnical Institute
21044 Derring Hall
Blacksburg, VA 24061

Mr. Roy Burger
1221 Serry Rd.
Schenectady, NY 12309

Dr. Robert Burrige
Schlumberger-Doll Resch Ctr.
Old Quarry Road
Ridgefield, CT 06877

Science Horizons, Inc.
ATTN: Dr. Theodore Cherry
710 Encinitas Blvd., Suite 101
Encinitas, CA 92024 (2 copies)

Professor Jon F. Claerbout
Professor Amos Nur
Dept. of Geophysics
Stanford University
Stanford, CA 94305 (2 copies)

Dr. Anton W. Dainty
Earth Resources Lab
Massachusetts Institute of Technology
42 Carleton Street
Cambridge, MA 02142
Professor Adam Dziewonski
Hoffman Laboratory
Harvard University
20 Oxford St.
Cambridge, MA 02138

Professor John Ebel
Dept of Geology and Geophysics
Boston College
Chestnut Hill, MA 02167

Dr. Donald Forsyth
Dept of Geological Sciences
Brown University
Providence, RI 02912

Dr. Anthony Gangi
Texas A&M University
Department of Geophysics
College Station, TX 77843

Dr. Freeman Gilbert
Institute of Geophysics &
Planetary Physics
University of California, San Diego
P.O. Box 109
La Jolla, CA 92037

Mr. Edward Giller
Pacific Seirra Research Corp.
1401 Wilson Boulevard
Arlington, VA 22209

Dr. Jeffrey W. Given
Sierra Geophysics
11255 Kirkland Way
Kirkland, WA 98033

Rong Song Jih
Teledyne Geotech
314 Montgomery Street
Alexandria, Virginia 22314

Professor F.K. Lamb
University of Illinois at
Urbana-Champaign
Department of Physics
1110 West Green Street
Urbana, IL 61801

Dr. Arthur Lerner-Lam
Lamont-Doherty Geological Observatory
of Columbia University
Palisades, NY 10964

Dr. L. Timothy Long
School of Geophysical Sciences
Georgia Institute of Technology
Atlanta, GA 30332

Dr. Peter Malin
University of California at
Santa Barbara
Institute for Central Studies
Santa Barbara, CA 93106

Dr. George R. Mellman
Sierra Geophysics
11255 Kirkland Way
Kirkland, WA 98033

Dr. Bernard Minster
IGPP, A-205
Scripps Institute of Oceanography
Univ. of California, San Diego
La Jolla, CA 92093

Professor John Nabelek
College of Oceanography
Oregon State University
Corvallis, OR 97331

Dr. Geza Nagy
U. California, San Diego
Dept of Ames, M.S. B-010
La Jolla, CA 92093

Dr. Jack Oliver
Department of Geology
Cornell University
Ithaca, NY 14850

Dr. Robert Phinney/Dr. F. A. Dahlen
Dept of Geological
Geological Science University
Princeton University
Princeton, NJ 08540

RADIX System, Inc.
Attn: Dr. Jay Pulli
2 Taft Court, Suite 203
Rockville, Maryland 20850

Dr. Norton Rimer
S-CUBED
A Division of Maxwell Laboratory
P.O. 1620
La Jolla, CA 92038-1620

Professor Larry J. Ruff
Department of Geological Sciences
1006 C.C. Little Building
University of Michigan
Ann Arbor, MI 48109-1063

Dr. Richard Sailor
TASC Inc.
55 Walkers Brook Drive
Reading, MA 01867

Thomas J. Sereno, Jr.
Science Application Int'l Corp.
10210 Campus Point Drive
San Diego, CA 92121

Dr. David G. Simpson
Lamont-Doherty Geological Observ.
of Columbia University
Palisades, NY 10964

Dr. Bob Smith
Department of Geophysics
University of Utah
1400 East 2nd South
Salt Lake City, UT 84112

Dr. S. W. Smith
Geophysics Program
University of Washington
Seattle, WA 98195

Dr. Stewart Smith
IRIS Inc.
1616 N. Fort Myer Drive
Suite 1440
Arlington, VA 22209

Rondout Associates
ATTN: Dr. George Sutton,
Dr. Jerry Carter, Dr. Paul Pomeroy
P.O. Box 224
Stone Ridge, NY 12484 (4 copies)

Dr. L. Sykes
Lamont Doherty Geological Observ.
Columbia University
Palisades, NY 10964

Dr. Pradeep Talwani
Department of Geological Sciences
University of South Carolina
Columbia, SC 29208

Dr. R. B. Tittmann
Rockwell International Science Center
1049 Camino Dos Rios
P.O. Box 1085
Thousand Oaks, CA 91360

Professor John H. Woodhouse
Hoffman Laboratory
Harvard University
20 Oxford St.
Cambridge, MA 02138

Dr. Gregory B. Young
ENSCO, Inc.
5400 Port Royal Road
Springfield, VA 22151-2388

FOREIGN (OTHERS)

Dr. Peter Basham
Earth Physics Branch
Geological Survey of Canada
1 Observatory Crescent
Ottawa, Ontario
CANADA K1A 0Y3

Professor Ari Ben-Menahem
Dept of Applied Mathematics
Weizman Institute of Science
Rehovot
ISRAEL 951729

Dr. Eduard Berg
Institute of Geophysics
University of Hawaii
Honolulu, HI 96822

Dr. Michel Bouchon - Universite
Scientifique et Medicale de Grenob
Lab de Geophysique - Interne et
Tectonophysique - I.R.I.G.M.-B.P.
38402 St. Martin D'Heres
Cedex FRANCE

Dr. Hilmar Bungum/NTNF/NORSAR
P.O. Box 51
Norwegian Council of Science,
Industry and Research, NORSAR
N-2007 Kjeller, NORWAY

Dr. Michel Campillo
I.R.I.G.M.-B.P. 68
38402 St. Martin D'Heres
Cedex, FRANCE

Dr. Kin-Yip Chun
Geophysics Division
Physics Department
University of Toronto
Ontario, CANADA M5S 1A7

Dr. Alan Douglas
Ministry of Defense
Blacknest, Brimpton,
Reading RG7-4RS
UNITED KINGDOM

Dr. Manfred Henger
Fed. Inst. For Geosciences & Nat'l Res.
Postfach 510153
D-3000 Hannover 51
FEDERAL REPUBLIC OF GERMANY

Ms. Eva Johannisson
Senior Research Officer
National Defense Research Inst.
P.O. Box 27322
S-102 54 Stockholm
SWEDEN

Tormod Kvaerna
NTNF/NORSAR
P.O. Box 51
N-2007 Kjeller, NORWAY

Mr. Peter Marshall, Procurement
Executive, Ministry of Defense
Blacknest, Brimpton,
Reading FG7-4RS
UNITED KINGDOM (3 copies)

Dr. Robert North
Geophysics Division
Geological Survey of Canada
1 Observatory crescent
Ottawa, Ontario
CANADA, K1A 0Y3

Dr. Frode Ringdal
NTNF/NORSAR
P.O. Box 51
N-2007 Kjeller, NORWAY

Dr. Jorg Schlittenhardt
Federal Inst. for Geosciences & Nat'l Res.
Postfach 510153
D-3000 Hannover 51
FEDERAL REPUBLIC OF GERMANY

University of Hawaii
Institute of Geophysics
ATTN: Dr. Daniel Walker
Honolulu, HI 96822

FOREIGN CONTRACTORS

Dr. Ramon Cabre, S.J.
Observatorio San Calixto
Casilla 5939
La Paz Bolivia

Professor Peter Harjes
Institute for Geophysik
Rhur University/Bochum
P.O. Box 102148, 4630 Bochum 1
FEDERAL REPUBLIC OF GERMANY

Dr. E. Husebye
NTNF/NORSAR
P.O. Box 51
N-2007 Kjeller, NORWAY

Professor Brian L.N. Kennett
Research School of Earth Sciences
Institute of Advanced Studies
G.P.O. Box 4
Canberra 2601
AUSTRALIA

Dr. B. Massinon
Societe Radiomana
27, Rue Claude Bernard
7,005, Paris, FRANCE (2 copies)

Dr. Pierre Mechler
Societe Radiomana
27, Rue Claude Bernard
75005, Paris, FRANCE

Dr. Svein Mykkeltveit
NTNF/NORSAR
P.O. Box 51
N-2007 Kjeller, NORWAY (3 copies)

GOVERNMENT

Dr. Ralph Alewine III
DARPA/NMRO
1400 Wilson Boulevard
Arlington, VA 22209-2308

Dr. Robert Blandford
DARPA/NMRO
1400 Wilson Boulevard
Arlington, VA 22209-2308

Sandia National Laboratory
ATTN: Dr. H. B. Durham
Albuquerque, NM 87185

Dr. Jack Evernden
USGS-Earthquake Studies
345 Middlefield Road
Menlo Park, CA 94025

U.S. Geological Survey
ATTN: Dr. T. Hanks
Nat'l Earthquake Resch Center
345 Middlefield Road
Menlo Park, CA 94025

Dr. James Hannon
Lawrence Livermore Nat'l Lab.
P.O. Box 808
Livermore, CA 94550

Paul Johnson
ESS-4, Mail Stop J979
Los Alamos National Laboratory
Los Alamos, NM 87545

Ms. Ann Kerr
DARPA/NMRO
1400 Wilson Boulevard
Arlington, VA 22209-2308

Dr. Max Koontz
US Dept of Energy/DP 5
Forrestal Building
1000 Independence Ave.
Washington, D.C. 20585

Dr. W. H. K. Lee
USGS
Office of Earthquakes, Volcanoes,
& Engineering
Branch of Seismology
345 Middlefield Rd
Menlo Park, CA 94025

Dr. William Leith
U.S. Geological Survey
Mail Stop 928
Reston, VA 22092

Dr. Richard Lewis
Dir. Earthquake Engineering and
Geophysics
U.S. Army Corps of Engineers
Box 631
Vicksburg, MS 39180

Dr. Robert Masse'
Box 25046, Mail Stop 967
Denver Federal Center
Denver, Colorado 80225

Richard Morrow
ACDA/VI
Room 5741
320 21st Street N.W.
Washington, D.C. 20451

Dr. Keith K. Nakanishi
Lawrence Livermore National Laboratory
P.O. Box 808, L-205
Livermore, CA 94550 (2 copies)

Dr. Carl Newton
Los Alamos National Lab.
P.O. Box 1663
Mail Stop C335, Group ESS-3
Los Alamos, NM 87545

Dr. Kenneth H. Olsen
Los Alamos Scientific Lab.
P.O. Box 1663
Mail Stop C335, Group ESS-3
Los Alamos, NM 87545

Howard J. Patton
Lawrence Livermore National
Laboratory
P.O. Box 808, L-205
Livermore, CA 94550

Mr. Chris Paine
Office of Senator Kennedy
SR 315
United States Senate
Washington, D.C. 20510

AFOSR/NP
ATTN: Colonel Jerry J. Perrizo
Bldg 410
Bolling AFB, Wash D.C. 20332-6448

HQ AFTAC/TT
Attn: Dr. Frank F. Pilotte
Patrick AFB, Florida 32925-6001

Mr. Jack Rachlin
USGS - Geology, Rm 3 C136
Mail Stop 928 National Center
Reston, VA 22092

Robert Reinke
AFWL/NTESG
Kirtland AFB, NM 87117-6008

Dr. Byron Ristvet
HQ DNA, Nevada Operations Office
Attn: NVCG
P.O. Box 98539
Las Vegas, NV 89193

HQ AFTAC/TGR
Attn: Dr. George H. Rothe
Patrick AFB, Florida 32925-6001

Donald L. Springer
Lawrence Livermore National Laboratory
P.O. Box 808, L-205
Livermore, CA 94550

Dr. Lawrence Turnbull
OSWR/NED
Central Intelligence Agency
CIA, Room 5G48
Washington, D.C. 20505

Dr. Thomas Weaver
Los Alamos National Laboratory
P.O. Box 1663
MS C 335
Los Alamos, NM 87545

GL/SULL
Research Library
Hanscom AFB, MA 01731-5000 (2 copies)

Secretary of the Air Force (SAFRD)
Washington, DC 20330
Office of the Secretary Defense
DDR & E
Washington, DC 20330

HQ DNA
ATTN: Technical Library
Washington, DC 20305

DARPA/RMO/RETRIEVAL
1400 Wilson Blvd.
Arlington, VA 22209

DARPA/RMO/Security Office
1400 Wilson Blvd.
Arlington, VA 22209

GL/XO
Hanscom AFB, MA 01731-5000

GL/LW
Hanscom AFB, MA 01731-5000

DARPA/PM
1400 Wilson Boulevard
Arlington, VA 22209

Defense Technical
Information Center
Cameron Station
Alexandria, VA 22314
(5 copies)

Defense Intelligence Agency
Directorate for Scientific &
Technical Intelligence
Washington, D.C. 20301

Defense Nuclear Agency/SPSS
ATTN: Dr. Michael Shore
6801 Telegraph Road
Alexandria, VA 22310

AFTAC/CA (STINFO)
Patrick AFB, FL 32925-6001

Dr. Gregory van der Vink
Congress of the United States
Office of Technology Assessment
Washington, D.C. 20510

Mr. Alfred Lieberman
ACDA/VI-OA'State Department Building
Room 5726
320 - 21st Street, NW
Washington, D.C. 20451

TACTEC
Battelle Memorial Institute
505 King Avenue
Columbus, OH 43201 (Final report only)

TACTEC
Battelle Memorial Institute
505 King Avenue
Columbus, OH 43201 (Final report only)